Stony Brook University

Optimal Mass Transport and Its Applications

A Dissertation presented

by

Zhengyu Su

to

The Graduate School

in Partial Fulfillment of the

Requirements

for the Degree of

Doctor of Philosophy

in

Computer Science

Stony Brook University

December 2015

Stony Brook University

The Graduate School

Zhengyu Su

We, the dissertation committe for the above candidate for the

Doctor of Philosophy degree, hereby recommend

acceptance of this dissertation

Xianfeng Gu - Dissertation Advisor
Associate Professor, Computer Science Department

Jie Gao - Chairperson of Defense
Associate Professor, Computer Science Department

Yalin Wang - Outside Member
Assistant Professor, School of Computing, Informatics, and Decision Systems Engineering
Arizona State University

Feng Luo - Outside Member
Professor, Department of Mathematics, Rutgers University

This dissertation is accepted by the Graduate School

Charles Taber
Dean of the Graduate School

Abstract of the Dissertation

Optimal Mass Transport and Its Applications

by

Zhengyu Su

Doctor of Philosophy

in

Computer Science

Stony Brook University

2015

Abstract

Optimal Mass Transport theory has deep roots in pure mathematics, combining complex analysis, Riemannian geometry and measure theory. Monge first raised the classical Optimal Mass Transport Problem that concerns determining the optimal way, with minimal transportation cost, to move a pile of soil from one place to another. Kantorovich has proven the existence and uniqueness of the optimal transport plan based on linear program. Monge-Kantorovich optimization has been used in numerous fields from physics, econometrics to computer science including computer vision, medical imaging and statistics. However, it has one fundamental disadvantage that the complexity is $O(k^2)$, which is unacceptable to computer vision and visualization applications since a high resolution 3D surface normally includes up to hundreds of thousands of vertices. In this dissertation, we introduce a practical optimal mass transport map based on Brenier's approach, which reduces the complexity from $O(k^2)$ to $O(k)$ and improves the efficiency and applicability. And we use our approach to address three practical applications of computer vision, medical imaging, and visualization.

Firstly, in computer vision, surface based 3D shape analysis is popular and critical. We proposed to use optimal mass transport map for shape analysis, focusing on two important shape analysis applications including surface registration and 3D shape classification. For surface registration problem, one commonly used approach is to use conformal map to convert the shapes into some canonical space. Although conformal mappings have small angle distortions, they may introduce large area distortions which are likely to cause numerical instability thus resulting failures of shape analysis. This

work proposed to compose the conformal map with the optimal mass transport map to get the unique area-preserving map, which is intrinsic to the Riemannian metric, unique, and diffeomorphic. For 3D shape classification study, we presented a novel Riemannian framework, *Conformal Wasserstein Shape Space*, by combing conformal geometry and Riemannian optimal mass transportation theory. In our work, all metric surfaces with the spherical topology are mapped to the unit sphere by a conformal mapping, which pushes the area element on the surface to a probability measure on the sphere. The Riemannian optimal mass transportation provides a map from the shape space of all topological spheres with metrics to the Wasserstein space of the disk and the pullback Wasserstein metric equips the shape space with a Riemannian metric. We validate our work by a real 3D classification problem of categorizing human brains with different intelligence quotient.

Secondly, in medical imaging, brain mapping transforms the brain cortical surface to canonical planar domains, which plays a fundamental role in morphological study. Most existing brain mapping methods are based on angle preserving maps, which may introduce large area distortions. Thus we proposed an area preserving brain mapping method based on Monge-Brenier theory. The brain mapping is intrinsic to the Riemannian metric, unique, and diffeomorphic. The computation is equivalent to convex energy minimization and power Voronoi diagram construction. Comparing to the existing approaches based on Monge-Kantorovich theory, the proposed one greatly reduces the complexity (from k^2 unknowns to k), and improves the simplicity and efficiency. Experimental results on caudate nucleus surface mapping and cortical surface mapping demonstrate the efficacy and efficiency of the proposed method. Conventional methods for caudate nucleus surface mapping may suffer from numerical instability; in contrast, current method produces diffeomorphic mappings stably. In the study of cortical surface classification for recognition of Alzheimer's Disease, the proposed method outperforms some other morphometry features.

Finally, in the visualization field, with the fast generation of large and complicated data nowadays, it is highly desirable to develop new frameworks aiming at generating a visualization of the entire data needed for navigation, detection, exploration and a global understanding of selected objects or regions of interest (ROIs). Angle-preservation (conformal) mapping/surface flattening preserves local shapes, and thus has been broadly used in many feature oriented applications in visualization and medical imaging. However, conformal method usually substantially distorts area, which fails to display accurate size of area, including height, width, thickness or diameter of ROIs. Unfortunately, these distorted area parameters are extremely important in many medical image recognition and auto diagnosis applications, such as brain fold detection or colon polyps detection and diagnosis. Therefore, we proposed to use our optimal mass transport map to address visualization applications that are beyond the scope of conformal mapping.

To my parents, my wife, my advisor Dr. Gu, as well as all that helped and cared about me.

Contents

List of Figures

Publications

- **Zhengyu Su**, Yalin Wang, Rui Shi, Wei Zeng, Jian Sun, Feng Luo, Xianfeng Gu: **Optimal Mass Transport for Shape Matching and Comparison**. *IEEE Transactions on Pattern Analysis and Machine Intelligence (T-PAMI)*, 37(11):2246-2259, November, 2015.

- **Zhengyu Su**, Wei Zeng, Yalin Wang, Zhonglin Lu, Xianfeng Gu: **Shape Classification using Wasserstein Distance for Brain Morphometry Analysis**. *Information Processing in Medical Imaging (IPMI)*, 24:411-423, 2015.

- **Zhengyu Su**, Wei Zeng, Rui Shi, Yalin Wang, Jian Sun, Xianfeng Gu: **Area Preserving Brain Mapping**. *IEEE Conference on Computer Vision and Pattern Recognition (CVPR)*, 2235 - 2242, Portland, Oregan, June, 2013.

- **Zhengyu Su**, Jian Sun, Xianfeng Gu, Feng Luo, Shing-Tung Yau: **Optimal mass transport for geometric modeling based on variational principles in convex geometry**. *Journal of Engineering With Computers*, 30(4):475-486, October, 2014.

- Rui Shi, Wei Zeng, **Zhengyu Su**, Hanna Damasio, Zhonglin Lu, Yalin Wang, Shing-Tung Yau, Xianfeng Gu: **Hyperbolic Harmonic Mapping for Constrained Brain Surface Registration**. *IEEE Conference on Computer Vision and Pattern Recognition (CVPR oral)*, 2531 - 2538, Portland, Oregan, June, 2013.

- Xin Zhao, **Zhengyu Su**, Xianfeng Gu, Arie Kaufman: **Area-Preservation Mapping using Optimal Mass Transport**. *IEEE Transactions on Visualization and Computer graphics (TVCG)*, 19(12):2838-47, December, 2013.

- Wei Luo, **Zhengyu Su**, Min Zhang, Wei Zeng, Junfei Dai, Xianfeng D. Gu: **Shape signature based on Ricci flow and optimal mass transportation**. *Journal of Optical Engineering*, April, 2014.

- Rui Shi, Wei Zeng, **Zhengyu Su**, Hanna Damasio, Zhonglin Lu, Yalin Wang, Shing-Tung Yau, Xianfeng Gu: **Hyperbolic harmonic brain surface registration with curvature-based landmark matching**. *Information Processing in Medical Imaging (IPMI)*, 23:159-70, 2013.

- Wei Zeng, Rui Shi, **Zhengyu Su**, David Xianfeng Gu: **Colon Surface Registration Using Ricci Flow**. *Abdomen and Thoracic Imaging*, 389-419, 2013.

1 Introduction

Nowadays surface parameterization has been used for a wide variety of applications like computer vision, medical imaging, computer graphics and visualization. Computational conformal geometry [56] has been employed to shape analysis [111, 25, 141] and surface registration [140], medical imaging[1], wireless sensor networks [107], visualization [85] and geometric modeling [47][66]. However, an accurate isometric parameterization is impossible for general surfaces. The conformal mapping may bring huge area distortions in certain surfaces, e.g. a slim surface of brain caudate nucleus. In turn, such distortions usually introduce much difficulty for following shape analysis.

In medical imaging field, as the clinical questions of interest move towards identifying very early signs of diseases, the corresponding statistical differences at the group level invariably become weaker and increasingly harder to identify. A stable method to compute some other mapping with alternative invariants may be highly advantageous for visualization and shape analysis in this research area.

In computer vision field, Studying the original surfaces could be extremely difficult when shapes are irregular and very complex, such as human body or human brain cortical surfaces. One effective and common approach is to first parameterize the original 3D domain to some classical parameter domains, such as planar or spherical domain, then register or analyze 3D surfaces through these canonical space [110, 41, 142]. This approach has the advantage of converting complex shapes to simple ones, reducing the computational complexity and improving the efficiency. Conformal geometry based methods have been frequently applied for shape parameterizations [25, 93, 51, 111, 132, 139, 69, 11]. Conformal mapping can keep angle unchanged and preserve local shapes (conformal), but may also produce huge area distortions. In Figure 13, the Armadillo model is mapped onto the planar unit disk. Frame (d) shows the image of a conformal mapping, where the head area shrunk exponentially to the height of the model and hard to be recognized. Other extruding parts, such as hands with fingers shown in the zoom-in image, the exponential area distortions may easily exceed machine precisions, leading to problems and failures of surface matching and registration. The conformal mapping in (d) pushes forward the area element on the Armadillo model to the planar disk. Then the unique optimal mass transport map is carried out from the disk with the push-forward measure in (d) to the disk with Euclidean measure. The composition of the conformal mapping and the optimal mass transport map is an area-preserving map from the surface to the Euclidean disk. The mapping result is shown in (c), where the head and figures occupy the same areas as those on the original surface. Area-preserving mapping avoids the huge area distortion, thus is more robust and intuitive for processing. Furthermore, this area-preserving mapping is intrinsic to the Riemannian metric, unique, and diffeomorphic. Therefore, the OMT map may help provide practical solutions for general 3D shape analysis tasks, such as surface parameterization, surface matching and comparison.

In the computer graphics and visualization areas, it is desirable to develop new frame-

works aiming at generating a visualization of the entire data needed for navigation, detection, exploration and a global understanding of selected objects or regions of interest (ROIs). Complex geometric structures are often better visualized and analyzed by mapping the surface properties, such as normal map, angle, or area, to a simple canonical domain, such as a rectangle or a sphere. Surface flattening and texture mapping offer a good way of visualizing a surface section by enabling the visualization of all surface parts within a single planar image.

In general, surface flattening and texture mapping unavoidably introduces distortions. There are two types of distortions, angle distortion and area distortion. A mapping, which is both angle preservation and area preservation, must be isometric. Therefore, the surface must have zero Gaussian curvature everywhere, namely a developable surface or a ruled surface. For general surfaces, one can only choose either angle-preservation mapping or area-preservation mapping, but never both of them simultaneously.

Angle-preservation (conformal) mapping/surface flattening preserves local shapes, and thus has been broadly used in many feature oriented applications in visualization and medical imaging. However, conformal method usually substantially distorts area, which fails to display accurate size of area, including height, width, thickness or diameter of ROIs. Unfortunately, these distorted area parameters are extremely important in many medical image recognition and auto diagnosis applications, such as brain fold detection [38] or colon polyps detection and diagnosis [62, 138]. Moreover, it is well known that conformal mapping induces severe area distortions for surfaces with long tube shapes, such as the elongated lion head model, as shown in Fig. 33. This disadvantage derives from the fundamental obstacle of conformal mapping theory and we can not easily overcome it. Imagine a cylinder $\mathbf{r}(\theta, z) = (\cos\theta, \sin\theta, z)$, a conformal mapping $\phi(\theta, z) = e^{-z}(\cos\theta, \sin\theta)$ maps it to the unit disk, the area distortion factor e^{-2z} is exponential with respect to the height z, and in practice easily exceeds the machine precision.

By comparison, area-preservation mapping can generate accurate and information lossless mapping results, which is a key objective for many medical imaging applications, with the ability to carry out measurements for detecting anatomic abnormalities. For example, in virtual colonoscopy, the physician may want to measure and compare different sizes of polyps, to determine disease conditions and cancer risks [58]. A special case of this problem also occurs in any application where volume or area measurement is critical (e.g. brain data in [38, 50, 150]). From human cognition perspective, area-preservation mapping and flattening can also enhance the viewer's ability to easily recognize the component-aware patches or long branch parts distribution of models, and consequently understand the local feature with the knowledge of a global structure (Fig. 33). Therefore, area-preservation mapping has vast potentials to be applied to many related visualization and graphics applications.

In this dissertation, we first review the mathematical background of computational conformal geometry and optimal mass transport theory in Section 2. Then in Section 3, we explain in details the computational algorithms. In section 4, we introduce the application

in medical imaging: Area preserving brain mapping. In section 5, applications in computer vision: Optimal mass transport for shape matching and comparison. In section 6, applications in visualization are introduced. Finally we conclude the dissertation with a sketch of the future plan.

2 Theoretical Background

By Poincare uniformization theorem, all shapes can be conformally deformed to one of the three canonical spaces: the unit sphere, the Euclidean plane or the hyperbolic plane. Generally speaking, such mapping will have distortions, since the geometric structures of a 3D surface and the plane usually have some differences. There are many metrics to measure the distortion of a mapping between two surfaces. These two are essential and important: angle distortion and area distortion. A mapping which preserves both angle and area between two surfaces preserves the Gaussian curvature [84], and is called a isometric mapping. Conformal mapping, or angle preserving mapping, is the one that minimizes angle distortion. It has many good properties and has been widely applied in many research and engineering areas [111, 25, 141, 140, 1]. However, conformal mapping may introduce large area distortions and may even cause numerical problems. In these scenarios, area-preserving mapping may be powerful.

In this section, we will briefly review the mathematical background of conformal geometry and optimal mass transport theory. For more details, we refer readers to a classical textbook [55] for conformal geometry, the seminal papers [78] on optimal transport map with Kantorovich's method, and [48] for more detailed proofs of the proposed method.

2.1 Homotopy

2.1.1 Homotopy Group

Definition 2.1. ***(Homotopy)****. Two continuous maps $f_0, f_1 : M \to N$ are said to be homotopic if there is a continuous map $f : M \times I \to N$ such that $F(\cdot, 0) = f_0$ and $F(\cdot, 1) = f_1$. The map F is called a homotopy[96][99][100] between f_0 and f_1, denoted as $f_0 \cong f_1$.*

As shown in Figure 1. It is easy to verify that the relation $\cong$ on the set of continuous maps from M to N is an equivalence relation. We can use the concept of homotopic maps to classify topological spaces.

A map $f : [0, 1] \to M$ from the unit interval to a topological space is called a path in M, if f and g are two paths in M with $f(1) = g(0)$. Then the product of f and g is a path $f \cdot g$, which is defined as

$$f \cdot g(t) = \begin{cases} f(2t), & 0 \le t \le \frac{1}{2}, \\ g(2t-1), & \frac{1}{2} \le t \le 1. \end{cases} \tag{2.1}$$

Definition 2.2. ***(Homotopic Paths)****[14]. Two paths f, g in M are said to be equivalent if f and g are homotopic relative to $\{0, 1\}$, denoted as $f \cong g$*

We denote the equivalence class of a path γ by $[\gamma]$. The product of equivalence classes of paths can be defined as

$$[f][g] = [f \cdot g] \tag{2.2}$$

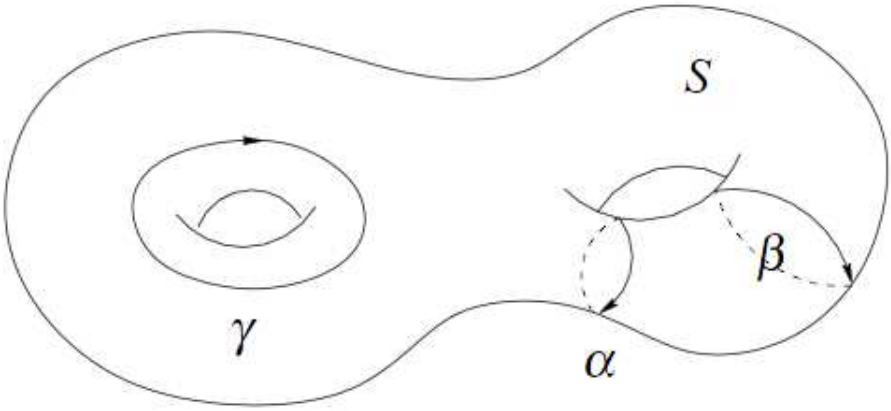

Figure 1: Homotopy:α is homotopy to β, but not to γ

We can verify that the multiplication of equivalence classes of paths is associative

$$([f][g])[h] = [f]([g][h]). \tag{2.3}$$

We say f is a closed path (loop) based at p if $f(0) = f(1) = p \in M$. We define $\varepsilon_p : I \to M$ as the constant path, i.e., $\varepsilon_p(t) = p$. Then we have

$$[f][\varepsilon_p] = [f] = [\varepsilon_p][f]. \tag{2.4}$$

Furthermore, the inverse of a path can be defined as $f^{-1}(t) = f(1-t)$. Then

$$[f][f^{-1}] = [\varepsilon_p] = [f^{-1}][f]. \tag{2.5}$$

Therefore, we have defined a group on the equivalence classes of closed paths based at $p \in M$, which we denote it by $\pi(M, p)$. This group is called the *fundamental group* or the *homotopy group*[65][100] of M.

Let $p, q \in M$. If there is a path γ from p to q, then groups $\pi(M, p)$ and $\pi(M, q)$ are isomorphic, $u_\gamma : \pi(M, p) \to \pi(M, q)$,

$$u_\gamma[g] = [\gamma \cdot g \cdot \gamma^{-1}]. \tag{2.6}$$

Therefore, we usually omit the base point for path connected spaces.

2.1.2 Covering Spaces

Definition 2.3. ***(Covering Space)****[65][83]. Let $p : \tilde{M} \to M$ be a continuous map, p is onto and for all $q \in M$, there is an open neighborhood U of q such that*

$$p^{-1}(U) = \cup_{j \in J} U_j \tag{2.7}$$

for some collection $\{U_j, j \in J\}$ of subsets of $\tilde{M}$, satisfying $U_j \cup U_k = \emptyset$ if $j \neq k$, and with $p|_{U_j} : U_j \to U$ a homeomorphism for each $j \in J$. : $\tilde{M} \to M$ is a covering.

Definition 2.4. ***(Lift)****. Suppose $p : \tilde{N} \to N$ is a covering, and $f : M \to N$ is a continuous map. Then a lift of f is a continuous map $\tilde{f} : M \to \tilde{N}$ such that $p \circ \tilde{f} = f$.*

Globally, $\tilde{M}$ and M have different topologies. If $\tilde{M}$ has simpler topology, then $\tilde{f}$ is easier to study than f. In general, the map f may have different lifts.

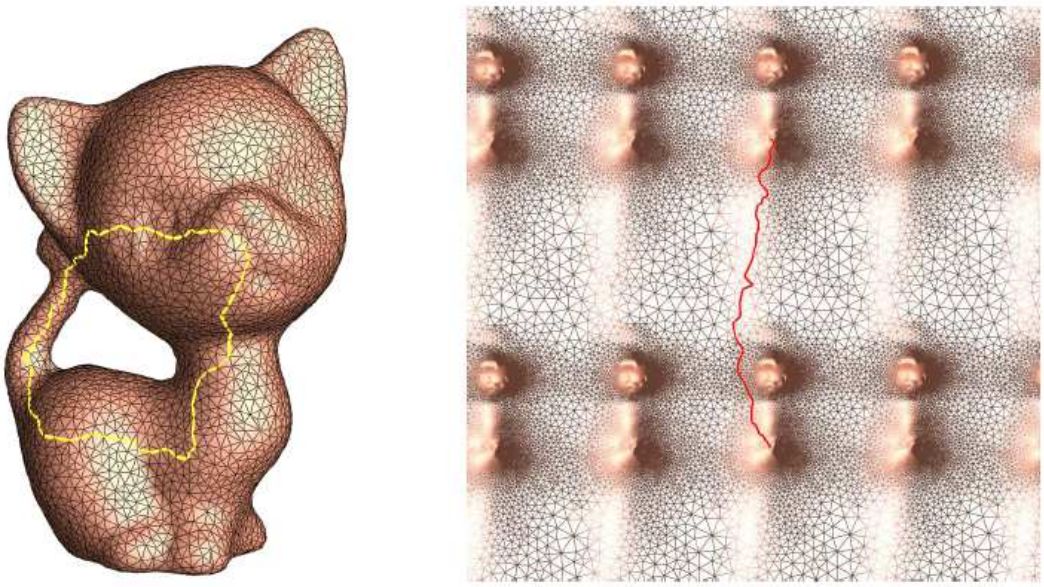

Figure 2: A loop on the surface is lifted to a path on the universal covering

Definition 2.5. ***(Deck Transformation)****. Suppose $p : \tilde{M} \to M$ is a covering. Then an automorphism $\tau : \tilde{M} \to \tilde{M}$ is called a deck transformation if*

$$p \circ \tau = p. \tag{2.8}$$

All of the deck transformation form a group $Deck(\tilde{M})$, the deck transformation group. M is homeomorphic to the quotient space

$$\frac{\tilde{M}}{Deck\tilde{M}} \cong M \tag{2.9}$$

Definition 2.6. *(**Fundamental Domain**). A closed subset $D \in \tilde{M}$ is called a fundamental domain of the Deck($\tilde{M}$), if $\tilde{M}$ is the union of conjugates of D,*

$$\tilde{M} = \bigcup_{\tau \in Deck} \tau D \tag{2.10}$$

and the intersection of any two conjugate has no interior.

Definition 2.7. *(**Universal Covering**). Suppose $p : \tilde{M} \to M$ is a covering. If $\tilde{M}$ is simply connected ($\pi(\tilde{M}, \tilde{q}) = e$), then the covering is a universal covering.(see figure 3)*

Figure 2 and 3 show examples of universal covering space.

2.2 Homology and Cohomology

Homology is anther tool to study the topological properties of a space by counting the number of holes. Generally speaking, (co)homology is the study of the relationship between closed and exact (co)chains.

2.2.1 Simplicial Homology

A fundamental problem in topology is that of determining, for two spaces, whether they are topologically equivalent. That is, we wish to know if one space can be morphed into the other without having to puncture it. The key idea of homology is to define invariants (i.e., quantities that cannot change by continuous deformation) that characterize topological spaces.

Definition 2.8. *(**Simplicial Complex**). A* simplicial complex *is a collection $\mathcal{K}$ of simplices, which satisfies the following two simple conditions:*

- *every face of each simplex in $\mathcal{K}$ is in $\mathcal{K}$;*
- *the intersection of any two simplices in $\mathcal{K}$ is either empty, or an entire common face.*

A *cycle*[65] is simply a closed k-chain, *i.e.*, a linear combination of k-simplices[65] so that the boundary of this chain is the empty set. Any set of vertices is a closed chain; any set of 1D loops are too. Equivalently, a k-cycle is any k-chain that belongs to Ker ∂k, by definition.

With the concept of k-cycle, we can define equivalence classes in homology. We will say that a k-cycle is homologous to another k-cycle (i.e., in the same equivalence class than the other) when these two chains differ by a boundary of a $(k+1)$-chain (i.e., by an exact chain). By definition, this exact chain is the image of ∂_{k+1}, i.e., Im ∂_{k+1}.

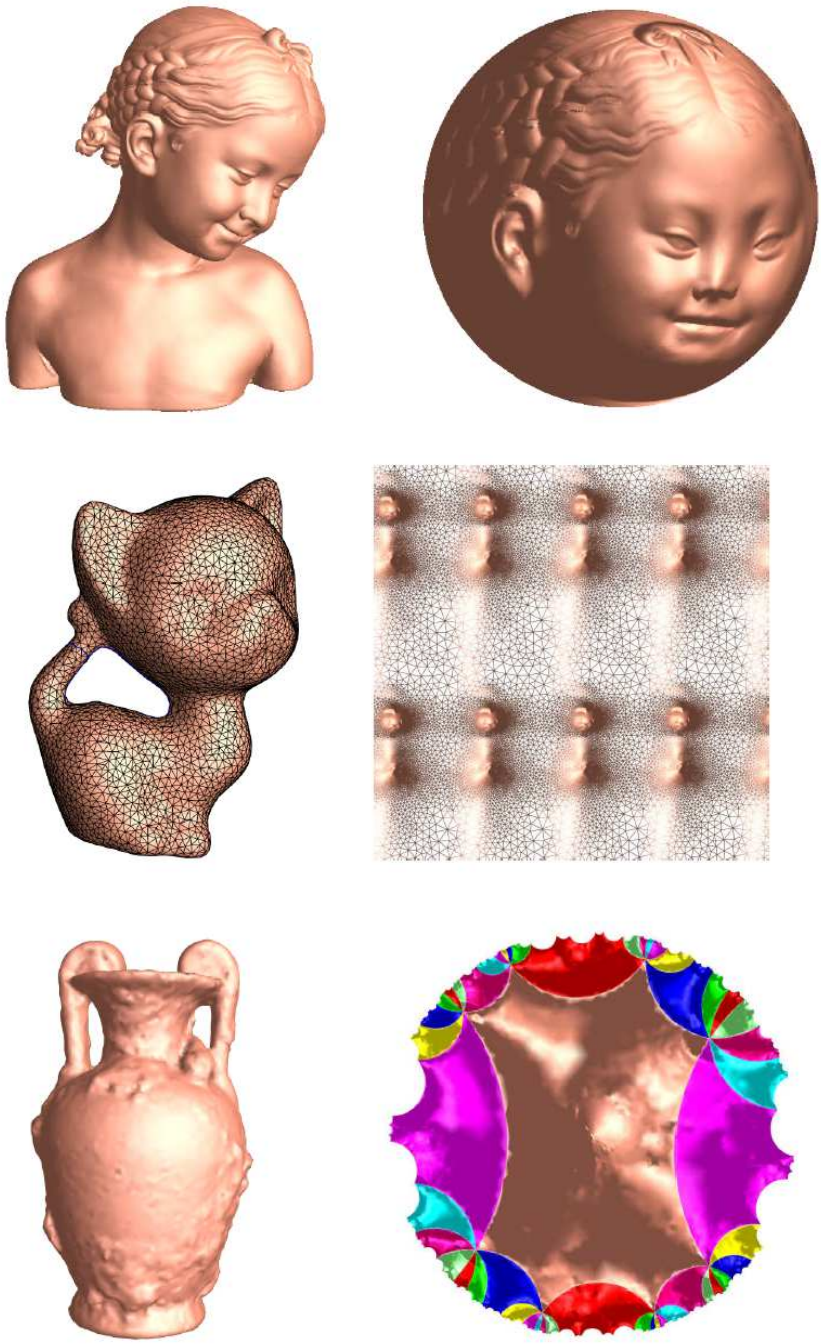

Figure 3: Universal covering of 3 canonical shapes: genus zero, genus one and high genus surface

2.2.2 Homology Groups

The homology groups[65] $\{\mathcal{H}_k\}_{k=0..n}$ of a chain complex based on ∂ are defined as the following quotient spaces:

$$\mathcal{H}_k = \frac{\text{Ker } \partial_k}{\text{Im } \partial_{k+1}}. \tag{2.11}$$

Here Ker ∂_k is the k-dimensional closed chain group and Im ∂_{k+1} is the k-dimensional boundary group. Two k-chains c_k^1, c_k^2 are homologous if they bound a $(k+1)$-chain c_{k+1},

$$c_k^1 - c_k^2 = \partial_{k+1} c_{k+1}, as shown in Figure 4 \tag{2.12}$$

$$\cdots \xrightarrow{\partial_{n+1}} C_n \xrightarrow{\partial_n} C_{n-1} \xrightarrow{\partial_{n-1}} \cdots \xrightarrow{\partial_2} C_1 \xrightarrow{\partial_1} C_0 \xrightarrow{\partial_0} 0$$

Figure 4: Homology

2.2.3 Cohomology Groups

The definition of cohomology groups[65] is much more general than homology groups. The cohomology groups is defined by taking the formal definition in the homology, replacing all occurrences of chain by cochain, of ∂ by d, and reverse the direction of the operator between spaces – this will also define equivalence classes. The cohomology groups of the deRham complex for the coboundary operator are simply the quotient spaces

$$\mathcal{H}_k^* = \frac{\text{Ker } d}{\text{Im } d} \tag{2.13}$$

Note that the homology and cohomology groups are not only dual notions, but they are also isomorphic; therefore, the cardinalities of their bases are equal.

2.3 Differential Forms

Euclidean space, R^n is endowed with a global coordinate system $(x^1, x^2, \cdots, x^n)$ and is the most general example of manifold.

A subset $M = M^n \in R^{n+r}$ is said to be an *n-dimensional submanifold* of R^{n+r} if locally M can be described by giving r of the coordinate differentiably in terms of the n

remaining ones. This means that given $p \in M$, a neighborhood of p on M can be described in some coordinate system $(x, y) = (x^1, \cdots, x^n, y^1, \cdots, y^r)$ of R^{n+r} by r differentiable functions

$$y^\alpha = f^\alpha(x^1, \cdots, x^n), \qquad \alpha = 1, \cdots r$$

We say that $x^1, \cdots, x^n$ are local coordinates for M near p.

In the n dimensional case, for each point $x_i \in R^n$ we need a linear transformation $\omega_{x_i} : R^n \to R$ which takes an (infinitesimal) displacement $\Delta x_i \in R^n$ as input and returns an (infinitesimal) scalar $\omega_{x_i}(\Delta x_i) \in R$ as output, representing the infinitesimal work required to move from x_i to x_{i+1} (In other words, ω_{x_i} is a linear functional on the space of tangent vectors at x_i, and is thus a cotangent vector at x_i). The net work $\int_\gamma \omega$ required to move from a to b along the path γ is approximated by

$$\int_\gamma \omega \approx \int_{i=0}^{n-1} \omega_{x_i}(\Delta x_i) \tag{2.14}$$

The object ω, which continuously assigns a *cotangent vector* to each point in R^n, is called a 1-*form*. There is in fact a duality between curves and forms. A 1-form is also called a *covarient vector* or *covector*, which means it is the dual concept of vector.

$$\int_\gamma (\omega_1 + \omega_2) = \int_\gamma \omega_1 + \int_\gamma \omega_2. \tag{2.15}$$

and

$$\int_{\gamma_1+\gamma_2} \omega = \int_{\gamma_1} \omega + \int_{\gamma_2} \omega. \tag{2.16}$$

Next consider the integration on 2-dimensional sets. Physically, such integrals arise when computing a *flux* of some field (e.g. a magnetic field) across a surface; a more intuitive example would arise when computing the net amount of force exerted by a wind blowing on a sail. If we have a parametrization of the surface $\phi : [0, 1]^2 \to R^n$, the surface can be cut up into infinitesimal oriented squares with corners $x := \phi(t_1, t_2), x + \Delta_1 x := \phi(t_1 + \Delta t, t_2), x + \Delta_2 x := \phi(t_1, t_2 + \Delta t), x + \Delta_1 x + \Delta_2 x := \phi(t_1 + \Delta t, t_2 + \Delta t)$, where $\Delta_1 x, \Delta_2 x \in R^n$ are the infinitesimal vectors

$$\Delta_1 x := \frac{\partial \phi}{\partial t_1}(t_1, t_2)\Delta t; \quad \Delta_2 x := \frac{\partial \phi}{\partial t_2}(t_1, t_2)\Delta t. \tag{2.17}$$

We refer to this object as the infinitesimal parallelogram with dimensions $\Delta_1 x \wedge \Delta_2 x$ with the base point x. Now we can define some sort of functional ω_x at this base point which should take the above infinitesimal parallelogram and return an infinitesimal number $\omega_x(\Delta_1 x \wedge \Delta_2 x)$, which physically should represent the amount of flux passing through

this parallelogram. With this intuition, we may require that the map $(\Delta_1 x \wedge \Delta_2 x) \mapsto \omega_x(\Delta_1 x \wedge \Delta_2 x)$ be *bilinear*, thus we have the axioms

$$\omega_x(c\Delta_1 x \wedge \Delta_2 x) = c\omega_x(\Delta_1 x \wedge \Delta_2 x) \tag{2.18}$$

$$\omega_x((\Delta_1 x + \widetilde{\Delta_1 x}) \wedge \Delta_2 x) = \omega_x(\Delta_1 x \wedge \Delta_2 x) + \omega_x(\widetilde{\Delta_1 x} \wedge \Delta_2 x) \tag{2.19}$$

$$\omega_x(\Delta_1 x \wedge c\Delta_2 x) = c\omega_x(\Delta_1 x \wedge \Delta_2 x) \tag{2.20}$$

$$\omega_x((\Delta_1 x + \widetilde{\Delta_1 x}) \wedge \Delta_2 x) = \omega_x(\Delta_1 x \wedge \Delta_2 x) + \omega_x(\widetilde{\Delta_1 x} \wedge \Delta_2 x) \tag{2.21}$$

$$\omega_x(\Delta x \wedge \Delta x) = 0 \tag{2.22}$$

Therefore, any continuous assignment $\omega : x \mapsto \omega_x$ that obeys the above axioms is called a *2-form*. It is not difficult to derive the *anti-symmetric* property

$$\omega_x(\Delta_1 x \wedge \Delta_2 x) = -\omega_x(\Delta_2 x \wedge \Delta_1 x) \tag{2.23}$$

More generally, one can define the concept of k-forms on an n-dimensional manifold for any $0 \leq k \leq n$ and integrate it against an oriented k-dimensional surface in that manifold.

The concept of derivation can be defined for differential forms[134] that map a k-form to a $k+1$-form, which is called *exterior differentiation* [44]. Using the exterior differentiation the fundamental theorem of calculus can be generalized to the *Stokes' theorem*

$$\int_S d\omega = \int_{\partial S} \omega. \tag{2.24}$$

In the special case of Euclidean space R^3, the differential operation $\omega \mapsto d\omega$ becomes the *gradient* operation $f \mapsto \nabla f$ when ω is 0-form, the *curl* operation $x \mapsto \nabla \times X$ when ω is a 1-form, the *divergence* operation $X \mapsto \nabla \cdot X$ when ω is a 2-form.

Finally, we can introduce the differential form in the complex domain as

$$dz = dx + idy \tag{2.25}$$

$$d\overline{z} = dx - idy \tag{2.26}$$

$$\frac{\partial}{\partial z} = \frac{1}{2}(\frac{\partial}{\partial x} - i\frac{\partial}{\partial y}) \tag{2.27}$$

$$\frac{\partial}{\partial \overline{z}} = \frac{1}{2}(\frac{\partial}{\partial x} + i\frac{\partial}{\partial y}) \tag{2.28}$$

The discrete counterpart of the differential forms mentioned above is represented by simplicial complexes[56][36]. Formally, a k-*simplex* σ_k is the non-degenerate convex hull of $k+1$ geometrically distinct points $v_0, \ldots v_k \in R^n$ with $n \geq k$, which is represented as

$$\sigma_k = \{x \in R^n | x = \sum_{i=0}^{k} \alpha^i v_i \text{ with } \alpha^i \geq 0 \text{ and } \sum_{i=0}^{k} \alpha^i = 1\}. \tag{2.29}$$

It can also be denoted by $\sigma_k = \{v_0 v_1 \ldots v_k\}$. The orientation of a simplex is determined by if there is an even or odd permutation from one to another.

The *boundary operator* on a k-simplex can be defined as

$$\partial\{v_0 v_1 \dots v_k\} = \sum_{j=0}^{k} (-1)^j \{v_0, \dots, \widehat{v_j}, \dots v_k\} \tag{2.30}$$

where $\widehat{v_j}$ indicates that v_j is missing from the sequence.

The boundary operator is a linear mapping from the space of k-simplices to the space of $(k-1)$-simplices, so it can simply be represented by a matrix of dimension $|\mathcal{K}^{k-1}| \times |\mathcal{K}^k|$.

A k-cochain ω is the dual of a k-chain, that is to say, ω is a linear mapping that takes k-chains to R.

$$\begin{aligned} \omega : \mathcal{C} &\to R \\ c &\to \omega(c), \end{aligned} \tag{2.31}$$

that is, a k-cochain ω operates on a k-chain c to give a scalar in R. Since a chain is a linear combination of simplices, a cochain returns a linear combination of the values of that cochain on each simplex involved. In other words, a k-cochain can be thought of as a field that can be evaluated on each k-simplex of an oriented simplicial complex $\mathcal{K}$. Recall that a k-chain can be represented as a vector c_k of length equal to the number of k-simplices in $\mathcal{M}$. Similarly, one may represent ω by a vector ω_k of the same size as c_k. The linear operation $\omega(c)$ translates into an inner product $\omega^k \cdot c_k$. A linear mapping from a chain to a real number is what we called a cochain.

In sum, k-cochains are discrete analogs to differential forms. For instance a 0-form can be evaluated at each point, a 1-form can be evaluated on each curve, a 2-form can be evaluated on each surface, etc. Now if we restrict integration to take place only on the k-submanifold which is the sum of the k-simplices in the triangulation, we get a k-cochain; thus k-cochains are a discretization of k-forms. One can further map a continuous k-form to a k-cochain. To do this, first integrate the k-form on each k-simplex and assign the resulting value to that simplex to obtain a k-cochain on the k-simplicial complex. This k-cochain is a discrete representation of the original k-form.

The operator d is called the *adjoint* of the boundary operator ∂: if we denote the integral sign as a pairing, *i.e.*, with the convention that $\int_\sigma \omega = [\sigma, \omega]$, then applying d on the left hand side of this operator is equivalent to applying ∂ on the right hand: $[d\sigma, \omega] = [\sigma, \partial\omega]$. For this very reason, d is sometimes called the *coboundary operator*. Finally, by linearity of integration, we can write a more general expression of Stokes' theorem, now extended to arbitrary chains as follows:

$$\int_{\sum_i c_i \sigma_i} d\omega = \int_{\partial(\sum_i c_i \sigma_i)} \omega = \int_{\sum_i c_i \partial\omega_i} \omega = \sum_i c_i \int_{\partial\sigma_i} \omega \tag{2.32}$$

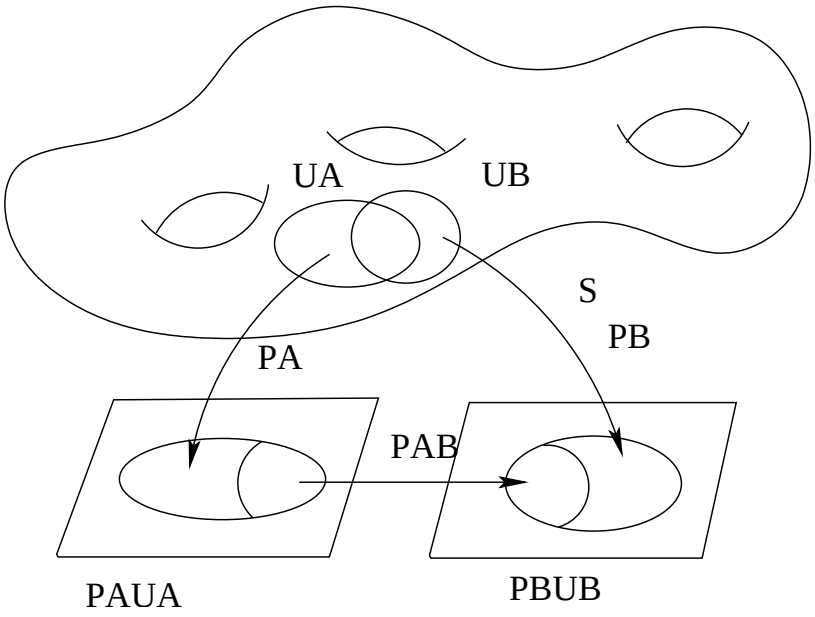

Figure 5: Riemannian manifold

2.4 Riemannian Geometry

2.4.1 Riemannian metric

A *Riemannian metric*[127] on a manifold M^n assigns, in a differentiable fashion, a positive definite inner product $<,>$ in each tangent space M_p^n. If $\langle,\rangle$ is only nondegenerate (i.e., $\langle u, v\rangle = 0$ for all v only if $u = 0$) rather than positive definite, then we shall call the resulting structure on M^n a *pseudo-Riemannian* metric. A manifold with a Riemannian metric is called a Riemannian manifold, which is shown in Figure 5

In terms of coordinate basis $e_i = \partial_i := \partial/\partial x^i$, we then have the differentiable matrices (the "metric tensor")

$$g_{ij}(x) = \langle \frac{\partial}{\partial x^i}, \frac{\partial}{\partial x^j} \rangle \tag{2.33}$$

Using the Riemannian metric we can define measures on the manifold. For example, the *First Fundamental Form* of a regular surface S in R^3 that is parameterized as $r(u, v)$ can be defined as

$$ds^2 = \langle dr, dr\rangle = \begin{pmatrix} du & dv \end{pmatrix} \begin{pmatrix} E(u,v) & F(u,v) \\ F(u,v) & G(u,v) \end{pmatrix} \begin{pmatrix} du \\ dv \end{pmatrix} \tag{2.34}$$

where

$$E = \langle r_u, r_u\rangle, F = \langle r_u, r_v\rangle, G = \langle r_v, r_v\rangle \tag{2.35}$$

We often use symbol g to denote the inner product matrix of the first fundamental form. Therefore, we can also write

$$ds^2 \equiv \langle dr, dr \rangle_g = \sum g_{\alpha\beta} dx^\alpha dx^\beta \tag{2.36}$$

2.4.2 Surface Uniformization Mapping

Conformal mapping between two surfaces preserves angles. Suppose $(S_1, \mathbf{g}_1)$ and $(S_2, \mathbf{g}_2)$ are two surfaces embedded in $\mathbb{R}^3$, $\mathbf{g}_1$ and $\mathbf{g}_3$ are the Euclidean induced Riemannian metrics. A mapping $\phi : S_1 \to S_2$ is called *conformal*, if the pull back metric of $\mathbf{g}_2$ induced by ϕ on S_1 differs from $\mathbf{g}_1$ by a positive scalar function: $\phi^* \mathbf{g}_2 = e^{2\lambda} \mathbf{g}_1$, where $\lambda : S_1 \to \mathbb{R}$ is a scalar function, called the *conformal factor*.

A circle domain on the complex plane is the unit disk with circular holes. All genus zero surfaces with boundaries can be conformally mapped to circle domains:

Theorem 2.9. *[Uniformization] Suppose S is a genus zero Riemannian surface with boundaries, then S can be conformally mapped onto a circle domain. All such conformal mappings differ by a Möbius transformation on the unit disk.*

2.5 Conformal Structure and Conformal Mapping

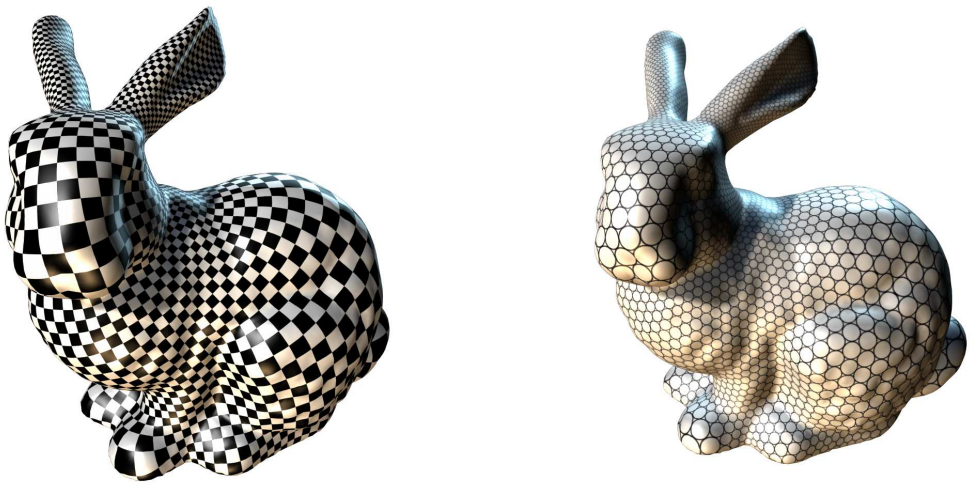

Figure 6: Conformal structure.

2.5.1 Hodge Duality

Recall that an (exterior) p-form is a covariant p-tensor that is antisymmetric ([44]). Therefore, a p-form in n dimensional space has dimension $\binom{n}{p}$. Since

$$\binom{n}{k} = \binom{n}{n-k},$$

there is a one-to-one correspondence between a p-vector (p-form) and $(n-p)$-vector ($(n-p)$-form) which forms a primal-dual pair.

In the vector case, the *Hodge star operator* of n vectors $e_{j_1}, e_{j_2}, \ldots e_{j_{n-p}}$ is defined as

$$(e_{j_1} \wedge e_{j_2} \wedge \ldots \wedge e_{j_{n-p}})^\star = e_{k_1} \wedge e_{k_2} \ldots \wedge e_{k_p}. \tag{2.37}$$

we can write out this in another form as

$$e^\star_{j_1 \ldots j_{n-p}} = e_{k_1 \ldots k_p} \tag{2.38}$$

In the covector (form) case, if α^1 is a 1-form, we look at its contravariant version A, and to this vector we may associate the pseudo $(n-1)$-form $i_A vol^n$. In this way we associate to each 1-form a pseudo $(n-1)$-form. In general, we can associate a p-form $\alpha^p = \alpha$ a pseudo $(n-p)$-form $\star\alpha$, called the *(Hodge-dual)* of α,

$$\alpha^\star_{j_1 \ldots j_{n-p}} = \sqrt{|g|} \sum_{k_1 < \ldots < k_p} \alpha^{k_1 \ldots k_p} \epsilon_{k_1 \ldots k_p j_1 \ldots j_{n-p}} \tag{2.39}$$

Here ϵ is the permutation symbol.

In the discrete setting, using the Hodge Dual concept we can define a *dual mesh* for each k-cell. For example, in the R^3 case, the dual 0-cell associated with the triangular face is the circumcenter of the triangle. The dual 1-cell associated with one of the primal edges is the line segment that joins the circumcenter of the triangle to the circumcenter of that edge, while the dual 2-cell associated with a primal vertex is corner wedge made of the convex hull of the circumcenter of the triangle, the two centers of the adjacent edges, and the vertex itself. An application of this primal-dual mesh is the computation of Voronoi/Delaunay in computational geometry [33]. Formally, k-chains and dual $(n-k)$-chains are represented by vectors of the same dimension. Similarly to the discrete exterior derivative (coboundary) operator, we may use a matrix (this time of size $|\mathcal{K}^k| \times |\mathcal{K}^k|$) to represent the Hodge star. In other words, we can define the discrete Hodge star through the following simple rule:

$$\frac{1}{|\sigma_k|} \int_{\sigma_k} \omega = \frac{1}{|\star\, \sigma_k|} \int_{\star\sigma_k} \star\omega \tag{2.40}$$

2.5.2 Harmonic Forms and Holomorphic Forms

After defining the Hodge star operator, we can now define the *Lapace Operator* Δ on forms:

$$\Delta : \bigwedge^p \to \bigwedge^p \text{ by } \Delta := dd^* + d^*d \tag{2.41}$$

Since $d^*d^* = 0$, we have $\Delta = (d + d^*)^2$.

We say that a form α^p is *harmonic* if $\Delta\alpha = 0$, which is called harmonic forms. And since

$$(\Delta\alpha^p, \alpha^p) = (dd^*\alpha + d^*d\alpha, \alpha) = (d^*\alpha, d^*\alpha) + (d\alpha, d\alpha) = \| d\alpha \|^2 + \| d^*\alpha \|^2, \quad (2.42)$$

we have

$$\Delta\alpha = 0 \Leftrightarrow d\alpha = 0 \text{ and } d^*\alpha = 0. \quad (2.43)$$

So harmonic forms on a closed manifold are both closed and coclosed.

Therefore, a harmonic 1-form $d\alpha$ on a Riemann surface can be treated as a vector field with zero circulation and divergence.

Definition 2.10. *A function $f : (x, y) \to (u, v)$ is holomorphic or complex analytic, if it satisfies the following Cauchy-Riemann equation:*

$$\begin{cases} \frac{\partial u}{\partial x} = \frac{\partial v}{\partial y} \\ \frac{\partial u}{\partial y} = -\frac{\partial v}{\partial x} \end{cases} \quad (2.44)$$

If $f = u + iv$ is holomorphic[54][74], then

$$\frac{\partial f}{\partial \overline{z}} = 0 \quad (2.45)$$

Furthermore, it is easy to verify that both u and v are harmonic. We say that u and v are conjugate if $u + iv$ satisfies the Cauchy-Riemann equation. If a holomorphic function f is bijective and f^{-1} is holomorphic, then f is a conformal mapping.

2.5.3 Conformal Mapping

Suppose $(S_1, \mathbf{g}_1)$ and $(S_2, \mathbf{g}_2)$ are two surfaces with Riemannian metrics $\mathbf{g}_1$ and $\mathbf{g}_2$ respectively. The local parameters of S_k are (x_1^k, x_2^k), the metric tensor has local representation

$$\mathbf{g}_k(x_1^k, x_2^k) = \begin{pmatrix} g_{11}^k & g_{12}^k \\ g_{21}^k & g_{22}^k \end{pmatrix} (x_1^k, x_2^k).$$

A mapping $\phi : (S_1, \mathbf{g}_1) \to (S_2, \mathbf{g}_2)$ has local representation $\phi : (x_1^1, x_2^1) \to (x_1^2, x_2^2)$. The Jacobian matrix of the mapping has the form

$$J_\phi(x_1^1, x_2^1) := \begin{pmatrix} \frac{\partial x_1^2}{\partial x_1^1} & \frac{\partial x_1^2}{\partial x_2^1} \\ \frac{\partial x_2^2}{\partial x_1^1} & \frac{\partial x_2^2}{\partial x_2^1} \end{pmatrix} (x_1^1, x_2^1).$$

Definition 2.11 (Pull Back Metric)**.** *Suppose $\phi : (S_1, \mathbf{g}_1) \to (S_2, \mathbf{g}_2)$ is a diffeomorphism between two Riemannian surfaces, the mapping ϕ induces a Riemannian metric on S_1, with local representation*

$$\phi^*\mathbf{g}_2 = J_\phi^T \mathbf{g}_2 J_\phi,$$

which is called the pull back metric induced by ϕ.

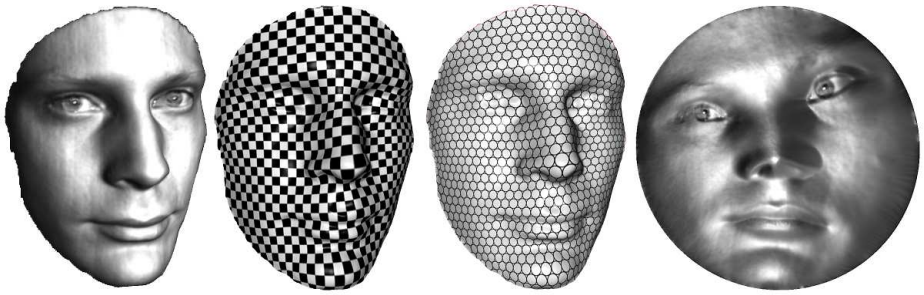

Figure 7: A conformal mapping from a male facial surface onto the planar unit disk.

Definition 2.12 (Conformal Mapping)**.** *Suppose $\phi : (S_1, \mathbf{g}_1) \to (S_2, \mathbf{g}_2)$ is a diffeomorphism between two Riemannian surfaces, if the pull back metric induced by ϕ differs from the original metric $\mathbf{g}_1$ by a scalar function,*

$$\phi^* \mathbf{g}_2 = e^{2\lambda} \mathbf{g}_1, \tag{2.46}$$

where $\lambda : S_1 \to \mathbb{R}$ is a function defined on S_1, then ϕ is called a conformal mapping.

As shown in Fig. 7, a conformal mapping from a male facial surface onto the planar unit disk is illustrated. We put checker board texture on the disk, and pull back the texture onto the facial surface. As shown in the second frame, all the right angles of checkers are well preserved. If we put circle packing texture on the disk, and pull it back on the face surface, all the circles are preserved, as demonstrated in the third frame. This demonstrates that a conformal mapping transforms infinitesimal circles to infinitesimal circles.

Theorem 2.13 (Riemann Mapping)**.** *Suppose a Riemannian surface $(S, \mathbf{g})$ is simply connected with a single boundary, then there exists a conformal mapping $\phi : S \to \mathbb{D}$ from the surface onto the planar unit disk $\mathbb{D}$, Furthermore, such mapping is unique upto a Möbius transformation.*

A Möbius transformation $\eta : \mathbb{D} \to \mathbb{D}$ for the unit disk to itself has the form

$$\eta(z) = e^{i\theta} \frac{z - z_0}{1 - \bar{z}_0 z}.$$

Riemann mapping theorem implies the existence of isothermal coordinates.

Definition 2.14 (Isothermal Coordinates)**.** *Suppose $(S, \mathbf{g})$ is a Riemannian surface, a local coordinate system (x_1, x_2) is called isothermal coordinates, if it is conformal, namely*

$$\mathbf{g} = e^{2\lambda(x_1, x_2)}(dx_1^2 + dx_2^2).$$

Under isothermal coordinates, the *Gaussian curvature* of the surface is given by

$$K(p) = -\frac{1}{e^{2\lambda(p)}}\Delta\lambda(p) = -\Delta_{\mathbf{g}}\lambda(p),$$

where Δ is the Laplace-Beltrami operator

$$\Delta = \partial_1^2 + \partial_2^2, \Delta_{\mathbf{g}} = \frac{1}{e^{2\lambda}}\Delta.$$

The geodesic curvature can be defined similarly. Under isothermal coordinates, the angle between the x-axis and the tangent direction of the boundary curve is $\theta(s)$, where s is the arc length parameter, $\mathbf{n}$ is the exterior normal to the boundary, then geodesic curvature reads

$$k_g = -\frac{1}{e^{\lambda}}\frac{\partial\theta}{\partial\mathbf{n}}$$

Theorem 2.15 (Gauss-Bonnet)**.** *The total curvature of $(S, \mathbf{g})$ is a topological invariant,*

$$\int_S KdA + \int_{\partial S} k_g ds = 2\pi\chi(S),$$

where $\chi(S)$ is the Euler characteristic number of the surface.

2.5.4 Ricci Flow

Riemann mapping can be computed using surface Ricci flow. Ricci flow deforms the Riemannian metric proportional to the curvature, such that the curvature evolves according to a heat diffusion process, and eventually becomes constant everywhere. Ricci flow is a powerful tool to design Riemannian metrics by prescribed curvatures.

Definition 2.16 (Surface Ricci Flow)**.** *Given the target curvature $\bar{K} : S \to \mathbb{R}$, the surface Ricci flow is defined as*

$$\frac{dg_{ij}(p,t)}{dt} = 2(\bar{K}(p) - K(p,t))g_{ij}(p,t),$$

One can set the target curvature to be constant $\rho = \frac{2\pi\chi(S)}{A(0)}$, where $A(0)$ is the total area at the time 0. During the flow, the curvature evolution equation is

$$\partial_t K = \Delta_{g(t)}K + 2K(K - \rho),$$

The convergence of surface Ricci flow has been proven,

Theorem 2.17 (Hamilton and Chow)**.** *The normalized Ricci flow on a closed surface converges to the metric with constant curvature ρ.*

Furthermore, surface Ricci flow is conformal, the conformal factor evolves

$$\partial_t\lambda(p,t) = 2(\rho - K(p,t))\lambda(p,t),$$

where the initial condition is $\lambda(p,0) \equiv 0$.

2.6 Optimal Mass Transportation

2.6.1 Monge's Problem

In the 18th century, Monge first raised a problem that minimizes the inter-domain transportation cost while preserves measure quantities[24]. Suppose X and Y are two metric spaces with probability measures μ and ν respectively. And suppose X and Y have equal total measures.

$$\int_X \mu = \int_Y \nu.$$

A map $T : X \to Y$ is *measure preserving* if for any measurable set $B \subset Y$, it satisfies

$$\mu(T^{-1}(B)) = \nu(B). \tag{2.47}$$

Denote transportation cost for sending $x \in X$ to $y \in Y$ by $c(x, y)$, then the total *transportation cost* is defined by

$$\mathcal{C}(T) := \int_X c(x, T(x)) d\mu(x). \tag{2.48}$$

Problem 2.18 (Optimal Mass Transport)**.** *Given two metric spaces with probabilities measures (X, μ), (Y, ν) with the transportation cost function $c : X \times Y \to \mathbb{R}$, the problem is to find the measure preserving map $T : X \to Y$, satisfying condition Eqn. 2.47, which minimizes the transportation cost Eqn. 2.48.*

In the 1940s, Kantorovich introduced the relaxation of Monge's problem and solved it using linear programming method [78].

At the end of 1980's, Brenier [26] discovered the intrinsic connection between optimal mass transport map and convex geometry.

2.6.2 Optimal Mass Transportation

Optimal mass transportation map is a special area-preserving mapping.

Definition 2.19 (Area-preserving Mapping)**.** *Suppose $\phi : (S_1, \mathbf{g}_1) \to (S_2, \mathbf{g}_2)$ is a diffeomorphism, the pull back metric induced by ϕ on S_1 is $\phi^* \mathbf{g}_2$, if*

$$det(\mathbf{g}_1) = det(\phi^* \mathbf{g}_2), \tag{2.49}$$

then ϕ is an area-preserving mapping.

Convex Geometry Convex geometry studies convex polyhedra in Euclidean space $\mathbb{R}^n$. The Minkowski theorem states that a convex polyhedron can be fully determined by its face normals and face areas.

Theorem 2.20 (Minkowski [108]). *Given k unit vectors $\mathbf{n}_1, \cdots, \mathbf{n}_k$ not contained in a half-space in $\mathbb{R}^n$ and $A_1, \cdots, A_k \geq 0$, such that*

$$\sum_{i=1}^{k} A_i \mathbf{n}_i = 0,$$

then there exists a convex polytope P with faces $F_1, \cdots, F_k$, such that the normal to F_i is $\mathbf{n}_i$ and the area of F_i is A_i. P is unique up to translations.

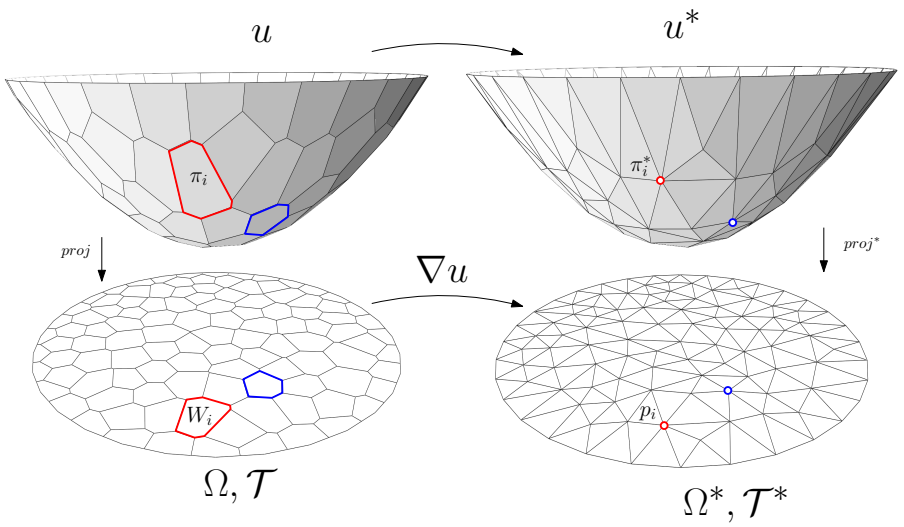

Figure 8: A PL convex function induces a cell decomposition of Ω. Each cell is mapped to a point.

Alexandrov generalized Minkowski's result to non-compact convex polyhedra. As shown in Fig.8, given k planes $\pi_i : \langle x, p_i \rangle + h_i$, one can construct a piecewise linear convex function

$$u(x) = \max_i \{\langle x, p_i \rangle + h_i | i = 1, \cdots, k\}, \tag{2.50}$$

whose graph is an infinite convex polyhedron. The PL convex function produces a convex cell decomposition $\{W_i\}$ of $\mathbb{R}^n$:

$$W_i = \{x | \langle x, p_i \rangle + h_i \geq \langle x, p_j \rangle + h_j, \forall j\} = \{x | \nabla u(x) = p_i\}. \tag{2.51}$$

Alexandrov shows that the convex polyhedron is determined by the face normal, or equivalently the gradient $\{p_i\}$ and the projected area $\{A_i\}$.

Theorem 2.21 (Alexandrov [9])**.** *Given a compact convex domain Ω in $\mathbb{R}^n$, if $p_1, \cdots, p_k$ are distinct in $\mathbb{R}^n$, $A_1, \cdots, A_k > 0$ such that*

$$\sum_{i=1}^{k} A_i = vol(\Omega),$$

then there exists a piecewise linear function $u(x) = \max_i\{\langle x, p_i\rangle + h_i\}$ unique up to translations, such that

$$Vol(W_i \cap \Omega) = A_i,$$

where W_i is defined in Eqn. 3.20.

Definition 2.22 (Alexandrov map)**.** *We call the gradient map $\nabla u : x \to \nabla u(x)$ the Alexandrov map, or briefly A-Map.*

According to Monge-Brenier theory [27], the Alexandrov map is the unique Optimal Mass Transport map that minimizes the following mass transport energy

$$\int_\Omega \|x - f(x)\|^2 dx,$$

among all mass preserving maps $f : \Omega \to \{p_1, \cdots, p_k\}$, such that

$$Vol(f^{-1}(p_i)) = A_i.$$

The computation of the Alexandrov map is equivalent to computing the so-called *power diagram* in computational geometry.

Power Diagram The power diagram is a generalization of Voronoi diagrams. Suppose each point p_i has a weight h_i, which may be positive or negative, the *power distance* from a point $\mathbf{x} \in \mathbb{R}^2$ to $\mathbf{p}$ is defined as

$$\text{Pow}(x, p_i) = \frac{1}{2}\|x - p_i\|^2 - \frac{1}{2}h_i.$$

When h_i is positive, the intuitive meaning of the power distance is one half of the squared distance from x to the tangent point of x to the circle centered at p_i with radius $\sqrt{h_i}$. The *power diagram* is the Voronoi diagram when we use power distance instead of the standard L_2 distance metric. It is again a partition of the Euclidean plane into polygonal cells, although some sites may have empty power cells $\{W_i\}$.

$$\begin{aligned} W_i &= \{x | Pow(x, p_i) \le Pow(x, p_j), \forall j\} \\ &= \{x | \langle x, p_i\rangle + 1/2(h_i - |p_i|^2) \ge \langle x, p_j\rangle + 1/2(h_j - |p_j|^2), \forall j\} \end{aligned}$$

Comparing this equation to Eqn.3.20, it is obvious that computing a power diagram is equivalent to compute the Alexandrov map.

Traditionally, constructing a power diagram is converted to computing the convex function in Eqn.3.18, which can be solved using convex hull algorithms in time $O(n \log n)$, such as the divide-and-conquer algorithm [103] or the randomized incremental algorithm [31].

The *power Delaunay triangulation* on the point set $\{p_1, \cdots, p_k\}$ is the dual to the power diagram. Two power cells W_i and W_j are adjacent in the diagram, if and only if there is an edge connecting p_i and p_j in the dual triangulation.

Optimal Mass Transportation Map by Variational Principle The computation of Alexandrov map is based on the following theorem.

Theorem 2.23 (Generalized Alexandrov)**.** *Given a convex domain $\Omega \subset \mathbb{R}^n$, with measure density $\rho : \Omega \to \mathbb{R}$, and a discrete point set $P = \{p_1, \cdots, p_k\}$ with discrete measures $\mu = \{\mu_1, \cdots, \mu_k\}$, such that*

$$\int_\Omega \rho(x)dx = \sum_{i=1}^{k} \mu_i,$$

then there exists a $\mathbf{h} = \{h_1, \cdots, h_k\}$ unique upto translations, such that the convex function $u(x) = \max_i\{\langle x, p_i\rangle + h_i\}$, induces a cell decomposition of $\mathbb{R}^n$, $\mathbb{R}^n = \bigcup_{i=1}^k W_i(\mathbf{h})$, and the area of each cell

$$w_i(\mathbf{h}) = \int_{W_i(\mathbf{h})\cap\Omega} \rho(x)dx$$

equals to μ_i. $\mathbf{h}$ is the unique global minimizer of the convex function

$$E_\mu(\mathbf{h}) = \sum_{i=1}^{k} \mu_i h_i - \int_{\mathbf{0}}^{\mathbf{h}} \omega, \tag{2.52}$$

where the differential form $\omega = \sum_{i=1}^k w_i(\mathbf{h})dh_i$.

The computation on 2D is based on power diagram and power triangulation. Suppose, two voroni cells $W_i(\mathbf{h}), W_j(\mathbf{h})$ are adjacent and they share a common edge e_{ij}. The edge e_{ij} has a dual Delaunay edge $\bar{e}_{ij}$. The norm with respect to ρ is defined as

$$|e|_\rho = \int_e \rho(x)dx, \tag{2.53}$$

and $|e|$ is just the traditional Euclidean length. By direct computation, we can show

$$\frac{\partial w_i}{\partial h_j} = \frac{\partial w_j}{\partial h_i} = \frac{|e_{ij}|_\rho}{|\bar{e}_{ij}|}.$$

Therefore the differential 1-form $\omega = \sum_{i=1}^k w_i dh_i$ is a closed 1-form, $d\omega = 0$. By Brunn-Minkowski inequality [9], the admissible space

$$\mathcal{H} := \{\mathbf{h} | \forall i, w_i(\mathbf{h}) > 0, \sum_i h_i = 0\}$$

is non-empty and convex. Therefore, $E(\mathbf{h}) = \int^{\mathbf{h}} \omega$ is well defined. The gradient of E is $(w_1, \cdots, w_k)$, the Hessian matrix of E is as follows. The off diagonal element is given by

$$\frac{\partial^2 E}{\partial h_i \partial h_j} = \frac{\partial w_i}{\partial h_j} = \frac{|e_{ij}|_\rho}{|\bar{e}_{ij}|}. \tag{2.54}$$

Because $\sum_i w_i(\mathbf{h}) = const$, therefore the diagonal element is given by

$$\frac{\partial w_i}{\partial h_i} = -\sum_{j \neq i} \frac{\partial w_i}{\partial h_j}, \tag{2.55}$$

the negative Hessian matrix is diagonal dominant, so E is concave on $\mathcal{H}$. Therefore E_μ in Eqn. 5.6 is positive definite, the desired solution is the unique global minimum.

An Alexandrov map can be obtained by optimizing the convex energy $E_\mu(\mathbf{h})$using Newton's method, where each iteration is to construct a power diagram dynamically. Algorithmically, each iteration in the optimization process is to construct a power diagram, which is classical in computational geometry and can be solved using mature, robust and efficient software packages, such as [6].

2.6.3 Shape Distance

Given a Riemannian surface $(S, \mathbf{g})$, we compute a Riemann mapping $\phi : (S, \mathbf{g}) \to (\mathbb{D}, dzd\bar{z})$. Assume the conformal factor function is $\lambda : S \to \mathbb{R}$, such that

$$\mathbf{g} \circ \phi^{-1}(z) = e^{2\lambda(z)} dzd\bar{z}.$$

Suppose the total area is π,

$$\int_{\mathbb{D}} e^{2\lambda(z)} dxdy = \pi,$$

we can find the unique optimal transportation map (Alexandov map) $\tau : (\mathbb{D}, e^{2\lambda} dzd\bar{z}) \to (\mathbb{D}, dwd\bar{w})$, τ can be represented as a complex-valued function defined on the unit disk.

Definition 2.24 (Shape Definition)**.** *Given two Riemannian surfaces, which are topological disks, $(S_1, \mathbf{g}_1)$ and $(S_2, \mathbf{g}_2)$, the Riemann mappings are ϕ_k, $k = 1, 2$ respectively. Let $\eta_k \in Mob(\mathbb{D})$ be a Möbius transformation, where $Mob(\mathbb{D})$ is the Mobius transformation group of the unit planar disk, then $\eta_k \circ \phi_k$ are still Riemann mappings. Each Riemann mapping $\eta_k \circ \phi_k$ determines a unique optimal transportation map $\tau_k(\phi_k, \eta_k)$. Then the distance between two surfaces is given by*

$$d(S_1, S_2) := \min_{\eta_1, \eta_2 \in Mob(\mathbb{D})} \int_{\mathbb{D}} |\tau_1(\phi_1, \eta_1) - \tau_2(\phi_2, \eta_2)|^2 dxdy.$$

The following lemma shows that the Riemann mapping ϕ and the optimal transportation map η encodes all the Riemannian metric information of the original surface.

Lemma 2.1. *Suppose a Riemannian surface $(S, \mathbf{g})$ with total area π, which is a topological disk, the Riemann mapping is $\phi : (S, \mathbf{g}) \to (\mathbb{D}, dzd\bar{z})$, the conformal factor induced by ϕ is $\lambda : S \to \mathbb{R}$, the optimal transportation map is $\eta : (\mathbb{D}, e^{2\lambda\circ\phi^{-1}(z)}dzd\bar{z}) \to (\mathbb{D}, dzd\bar{z})$, then the Riemannian metric of the original surface is given by*

$$\mathbf{g} \circ \phi^{-1}(z) = det(J_\eta)dzd\bar{z}.$$

Proof. Because $\phi : (S, \mathbf{g}) \to (\mathbb{D}, dzd\bar{z})$ is conformal, according to Eqn. 2.46

$$\mathbf{g} \circ \phi^{-1}(z) = e^{2\lambda\circ\phi^{-1}(z)}dzd\bar{z},$$

Because $\eta : (\mathbb{D}, e^{2\lambda}dzd\bar{z}) \to (\mathbb{D}, dzd\bar{z})$ is an optimal transportation map, therefore it is area-preserving. According to Eqn. 2.49,

$$e^{2\lambda} = det(J_\eta).$$

Combine the above two equations, we get the formula in the lemma. □

The following theorem is classical in surface differential geometry.

Theorem 2.25. *Suppose $(S, \mathbf{g})$ is a closed Riemannian surface embedded in in $\mathbb{R}^3$ with isothermal coordinates, then S is determined unique upto a rigid motion by the conformal factor λ and mean curvature function H defined on isothermal coordinates. If S has boundaries, then S is determined by (λ, H) and Dirichlet boundary condition.*

We now give the proof for the main theorem.

Proof. Suppose two marked topological disks $(S_1, \mathbf{g}_1, p_0, p_1)$ and $(S_2, \mathbf{g}_2, q_0, q_1)$ are given.

We prove the first claim:
'$\Longrightarrow$' if there exists an isometry $f : S_1 \to S_2$, such that $f(p_k) = q_k$, $k = 0, 1$, consider the normalized Riemann mappings $\phi_1 : S_1 \to \mathbb{D}$, $\phi_1(p_0) = 0$ and $\phi_1(p_1) = 1$, $\phi_2 : S_2 \to \mathbb{D}$, $\phi_2(q_0) = 0$ and $\phi_2(q_1) = 1$, the composition

$$\phi_2 \circ f \circ \phi_1^{-1} : \mathbb{D} \to \mathbb{D}$$

is conformal, therefore a Möbius transformation, which fixes 0 and 1, hence it is the identity, namely

$$f = \phi_2^{-1} \circ \phi_1,$$

Suppose $\mathbf{g}_1 = e^{2\lambda_1}\phi_1^* dzd\bar{z}$, and $\mathbf{g}_2 = e^{2\lambda_2}\phi_1^* dzd\bar{z}$, therefore

$$f^*\mathbf{g}_2 = e^{2(\lambda_2-\lambda_1)}\mathbf{g}_1,$$

because f is an isometry, therefore $\lambda_1 \equiv \lambda_2$. Therefore the measures on the disk induced by ϕ_1 and ϕ_2 are equal. According to the uniqueness of the optimal transportation map, we obtain $\eta_1 \equiv \eta_2$.
'$\Longleftarrow$' Reversely, if $\eta_1 \equiv \eta_2$, according to lemma 2.1, $\lambda_1 \equiv \lambda_2$. Define the composition $f : S_1 \to S_2$, $f := \phi_2^{-1} \circ \phi_1$, because ϕ_1 and ϕ_2 are conformal, so f is conformal, $f^*\mathbf{g}_2 = e^{2(\lambda_1 - \lambda_2)}\mathbf{g}_1$, so f is an isometry.
We prove the second claim:
From the first claim, $\eta_1 \equiv \eta_2$ is equivalent to $\lambda_1 \equiv \lambda_2$, then according to theorem 2.25, the claim holds. □

2.6.4 Wasserstein Metric Space

Suppose $(M, \mathbf{g})$ is a Riemannian manifold with a Riemannian metric $\mathbf{g}$.

Definition 2.26 (Wasserstein Space)**.** *Let $\mathcal{P}_p(M)$ denote the space of all probability measures μ on M with finite p^{th} moment, where $p \geq 1$. Suppose there exists some point $x_0 \in M$ that $\int_M d(x, x_0)^p d\mu(x) < +\infty$, where d is the geodesic distance induced by* $\mathbf{g}$.

Given two probability μ and ν in $\mathcal{P}_p$, the Wasserstein distance between them is defined as the transportation cost induced by the optimal mass transport map $T : M \to M$,

$$W_p(\mu, \nu) := \inf_{T_{\#}\mu = \nu} \left(\int_M d(x, T(x))^p d\mu(x) \right)^{\frac{1}{p}}.$$

The following theorem plays a fundamental role for the current work

Theorem 2.27. *The Wasserstein distance W_p is a Riemannian metric of the Wasserstein space $\mathcal{P}_p(M)$.*

Detailed proof can be found in [129].

2.6.5 Conformal Wasserstein Shape Space

Combing optimal transportation and conformal mapping theories, we can construct a shape space framework.

We consider all oriented metric surfaces $(M, \mathbf{g})$ with the disk topology, namely M is of genus 0 and with a single boundary ∂M. There are two markers $(p, q) \subset M$, p is an interior point, q is a boundary point. We call $(M, \mathbf{g}, p, q)$ as a *marked metric surface*. The set of all marked metric surfaces is denoted as $\mathcal{M}$, $\mathcal{M} := \{marked\ metric\ surfaces\}$.

Two marked metric surfaces are equivalent, if there is a *normalized isometric diffeomorphism* $\phi : (M_1, \mathbf{g}_1, p_1, q_1) \to (M_2, \mathbf{g}_2, p_2, q_2)$, such that ϕ preserves metrics $\phi^*\mathbf{g}_2 = \mathbf{g}_1$ and preserves markers $\phi(p_1) = p_2, \phi(q_1) = q_2$. The product of the normalized isometry diffeomorphism group and the scaling group is denoted as G, $G := \{normalized\ isometries\} \oplus \{scaling\}$.

We define the shape space as

$$\mathcal{S} := \mathcal{M}/G. \tag{2.56}$$

Let $(M, \mathbf{g}, p, q) \in \mathcal{S}$ is a normalized marked metric surface, such that its total area is π. In the following discussion, we always omit the markers (p, q), and assume the total area is π. Then according to Riemann mapping theorem, there is a unique conformal mapping $\phi : M \to \mathbb{D}$, where $\mathbb{D}$ is the unit planar disk with Euclidean metric $dx^2 + dy^2$, such that $\phi(p) = (0, 0)$ and $\phi(q) = (1, 0)$. Then $\mathbf{g} = e^{2\lambda(x,y)}(dx^2 + dy^2)$. ϕ push forward the area element on $(M, \mathbf{g})$ to the disk as

$$\mu_{(M,\mathbf{g})} := e^{2\lambda(x,y)} dx \wedge dy. \tag{2.57}$$

This gives an injective mapping $\Gamma : \mathcal{S} \to \mathcal{P}_2(\mathbb{D})$, $\Gamma : (M, \mathbf{g}) \mapsto \mu_{(M,\mathbf{g})}$. The Wasserstein metric on the Wasserstein space $\mathcal{P}_2(\mathbb{D})$ is pulled back to $\mathcal{S}$,

$$d_{\mathcal{S}}((M_1, \mathbf{g}_1), (M_2, \mathbf{g}_2)) := W_2(\mu_{(M_1,\mathbf{g}_1)}, \mu_{(M_2,\mathbf{g}_2)}). \tag{2.58}$$

We call the metric space $(\mathcal{S}, d_{\mathcal{S}})$ the *conformal Wasserstein shape space*.The constructed shape space enjoys numerous advantages such as that it is intrinsic geometric structure and does not have reparameterization ambiguity, etc.

3 Computational Algorithms

3.1 Conformal Mapping

In discrete setting, the captured surfaces are represented as discrete polyhedral surfaces. Suppose S is a topological surface, V is a set of points on S, (S, V) is called a *marked surface*. T is a triangulation of S, whose vertices are in V, then (S, T) is called a *triangular mesh*. In the following discussion, we use E and F to represent the edge and face sets. A piecewise linear Riemannian metric (PL metric) on (S, V) is a flat cone metric, whose cone points are in V, represented by edge lengths.

Definition 3.1 (Discrete Riemannian Metric)**.** *A discrete metric on a triangular mesh (S, T) is a function defined on the edges $d : E \to \mathbb{R}^+$, which satisfies the triangle inequality, on a face $[v_i, v_j, v_k]$,*

$$d_{ij} + d_{jk} > d_{ki}, d_{ki} + d_{ij} > d_{jk}, d_{ik} + d_{kj} > d_{ij}.$$

The discrete curvature is defined as angle deficit,

Definition 3.2 (Discrete Gauss Curvature)**.** *The discrete Gauss curvature function on a mesh is defined on vertices, $K : V \to \mathbb{R}$,*

$$K(v) = \begin{cases} 2\pi - \sum_i \theta_i & v \notin \partial(S, T, V) \\ \pi - \sum_i \theta_i & v \in \partial(S, T, V) \end{cases}$$

where θ_i's are corner angles adjacent to the vertex v, and $\partial(S, T)$ represents the boundary of the mesh.

Gauss-Bonnet theorem still holds on discrete surface, the total Gauss curvature of a mesh M

$$\sum_i K(v_i) = 2\pi\chi(S),$$

where $\chi(S)$ is the Euler characteristic number of S.

In practice, a choose a special triangulation according to the given discrete metric,

Definition 3.3 (Delaunay Triangulation)**.** *A closed discrete surface (S, T) with a discrete metric d, we say a triangulation T is Delaunay, if for any edge $[v_i, v_j]$ adjacent to two faces $[v_i, v_j, v_k]$ and $[v_j, v_i, v_l]$,*

$$\theta_k^{ij} + \theta_l^{ji} \leq \pi,$$

where θ_k^{ij} is the corner angle at v_k in $[v_i, v_j, v_k]$, θ_l^{ji} is the angle at v_l in $[v_j, v_i, v_l]$.

Discrete Surface Yamabe flow We define the discrete conformal factor function as $u : V \to \mathbb{R}$, and conformal structure coefficient on edges $\eta : E \to \mathbb{R}^+$.

Definition 3.4 (Discrete Conformal Equivalence)**.** *Two discrete metrics d and d' on (S, V) are discrete conformal if there exists a sequence of discrete metrics $d = d_1, d_2, d_3, \cdots, d_n = d'$ on (S, V) and triangulations $T_1, T_2, \cdots, T_n$ of (S, V),satisfying:*
(a) each T_i is Delaunay in d_i,
(b) if $T_i = T_{i+1}$, there exists a conformal factor, so that if $e \in T_i$ is with end vertices v and v', then

$$d_{i+1}(e) = e^{u(v)} d_i(e) e^{u(v')},$$

(c) if $T_i \neq T_{i+1}$, then (S, d_i) is isometric to (S, d_{i+1}) by an isometry homotopic to the identity in (S, V).

Each discrete conformal class of discrete metrics is called a *discrete Riemann surface*.

Definition 3.5 (Discrete Yamabe Flow with Surgery)**.** *Given a surface (S, V) with a discrete metric d, given a target curvature function $\bar{K} : V \to \mathbb{R}$, $\bar{K}(v_i) \in (-\infty, 2\pi)$, and the total target curvature satsifies Gauss-Bonnet formula, the discrete Yamabe flow is defined as*

$$\frac{du(v_i)}{dt} = \bar{K}(v_i) - K(v_i), \tag{3.1}$$

under the constraint $\sum_{v_i \in V} u(v_i) = 0$. During the flow, the triangulation on (S, V) is updated to be Delaunay with respect to $d(t)$, for all time t.

The existence of the solution to the Yamabe flow is guaranteed by the following theorem.

Theorem 3.6. *Suppose (S, V) is a closed connected surface and d is any discrete metric on (S, V). Then for any $\bar{K} : V \to (-\infty, 2\pi)$ satisfying Gauss-Bonnet formula, there exists a discrete metric $\bar{d}$, unique up to scaling on (S, V), so that $\bar{d}$ is discrete conformal to d and the discrete curvature of $\bar{d}$ is $\bar{K}$. Furthermore, the $\bar{d}$ can be obtained by discrete Yamabe flow with surgery.*

Furthermore, it has been show that Yamabe flow is the negative gradient flow of the following Yamabe energy,

$$f(u_1, u_2, \cdots, u_n) = \int^{(u_1, u_2, \cdots, u_n)} \sum_{v_i \in V} (\bar{K}(v_i) - K(v_i)) du_i. \tag{3.2}$$

The gradient of Yambe energy is $\nabla f(u_1, \cdots, u_n) = (\bar{K}_1 - K_1, \bar{K}_2 - K_2, \cdots, \bar{K}_n - K_n)^T$. The Yamabe energy is strictly concave in the subspace $\sum_{v_i \in V} u_i = 0$. The Hessian matrix can be formulated explicitly. The cotangent edge weight is defined as

$$w_{ij} := \begin{cases} \cot \theta_k^{ij} + \cot \theta_l^{ji} & [v_i, v_j] \notin \partial(S, T) \quad [v_i, v_j] = [v_i, v_j, v_k] \cap [v_j, v_i, v_l] \\ \cot \theta_k^{ij} & [v_i, v_j] \in \partial(S, T) \qquad\qquad\quad [v_i, v_j] \in \partial[v_i, v_j, v_k] \end{cases} \tag{3.3}$$

Algorithm 1 Discrete Surface Yamabe Flow

Require: The inputs include:

1. A triangular mesh Σ, embedded in $\mathbb{E}^3$;
2. A target curvature $\bar{K}$, $\sum \bar{K}_i = 2\pi\chi(\Sigma)$ and $\bar{K}_i \in (-\infty, 2\pi)$.

Ensure: A discrete metric conformal to the original one, which realizes the target curvature $\bar{K}$.

Initialize the discrete conformal factor u as 0 and conformal structure coefficient η, such that $\eta(e)$ equals to the initial edge length of e.
while $\max_i |\bar{K}_i - K_i| > threshold$ **do**
    Compute the edge length from γ and η
    Update the triangulation to be Delaunay using diagonal edge swap for each pair of adjacent faces
    Compute the corner angle θ_i^{jk} from the edge length using cosine law
    Compute the vertex curvature K
    Compute the Hessian matrix H
    Solve linear system $H\delta u = \bar{K} - K$
    Update conformal factor $u \leftarrow u - \delta u$
end while
Output the result circle packing metric.

The Hessain matrix $H = (h_{ij})$, where

$$h_{ij} = \begin{cases} -w_{ij} & v_i \sim v_j \quad i \neq j \\ 0 & v_i \not\sim v_j \quad i \neq j \\ \sum_k w_{ik} & \quad i = j \end{cases} \tag{3.4}$$

In order to compute the conformal metric with prescribed curvature, we can optimize the Yamabe energy using Newton's method.

3.2 Discrete Optimal Mass Transport

3.2.1 Kantorovich's Approach.

The space X and Y are discretized to sample points, $X = \{x_1, x_2, \cdots, x_n\}$, $Y = \{y_1, y_2, \cdots, y_n\}$, the measures are dirac measures

$$\mu = \sum_{i=1}^{n} \mu_i \delta(x - x_i), \nu = \sum_{j=1}^{n} \nu_j \delta(y - y_j),$$

the transport plan τ is represented as a matrix (τ_{ij}), such that

$$\sum_{j=1}^{n} \tau_{ij} = 1, \sum_{i=1}^{n} \tau_{ij} = 1, \tau_{ij} \geq 0.$$

All such matrices form a convex polytope. The total transportation cost is a linear function

$$\mathcal{C}(\tau) = \sum_{i,j} c(x_i, y_j)\tau_{ij}.$$

The optimal mass transport problem becomes a linear programming problem with n^2 unknowns τ_{ij}.

3.2.2 Brenier's Approach.

Suppose μ has compact support on X, define

$$\Omega = supp\, \mu = \{x \in X | \mu(x) > 0\},$$

assume Ω is a convex domain in X. The space Y is discretized to $Y = \{y_1, y_2, \cdots, y_k\}$ with Dirac measure $\nu = \sum_{j=1}^{k} \nu_j \delta(y - y_j)$.

We define a *height vector* $\mathbf{h} = (h_1, h_2, \cdots, h_n) \in \mathbb{R}^k$, consisting of k real numbers. For each $y_i \in Y$, we construct a hyperplane defined on X,

$$\pi_i(\mathbf{h}) : \langle x, y_i \rangle + h_i = 0. \tag{3.5}$$

Define a function

$$u_{\mathbf{h}}(x) = \max_{i=1}^{k} \{\langle x, y_i \rangle + h_i\}, \tag{3.6}$$

then $u_{\mathbf{h}}(x)$ is a convex function. We denote its graph by $G(\mathbf{h})$, which is an infinite convex polyhedron with supporting planes $\pi_i(\mathbf{h})$. The projection of $G(\mathbf{h})$ induces a polygonal partition of Ω,

$$\Omega = \bigcup_{i=1}^{k} W_i(\mathbf{h}), \tag{3.7}$$

where each cell $W_i(\mathbf{h})$ is the projection of a facet of the convex polyhedron $G(\mathbf{h})$ onto Ω,

$$W_i(\mathbf{h}) = \{x \in X | u_{\mathbf{h}}(x) = \langle x, y_i \rangle + h_i\} \cap \Omega. \tag{3.8}$$

The area of $W_i(\mathbf{h})$ is given by

$$w_i(\mathbf{h}) = \int_{W_i(\mathbf{h})} \mu(x) dx. \tag{3.9}$$

The convex function $u_{\mathbf{h}}$ on each cell $W_i(\mathbf{h})$ is a linear function $\pi_i(\mathbf{h})$, therefore, the gradient map

$$grad\, u_{\mathbf{h}} : W_i(\mathbf{h}) \to y_i, i = 1, 2, \cdots, k. \tag{3.10}$$

maps each $W_i(\mathbf{h})$ to a single point y_i.

The following theorem plays a fundamental role for discrete optimal mass transport theory,

Theorem 3.7. *For any given measure ν, such that*

$$\sum_{j=1}^{n} \nu_j = \int_\Omega \mu, \nu_j > 0,$$

there must exist a height vector $\mathbf{h}$ *unique up to adding a constant vector* $(c, c, \cdots, c)$*, the convex function Eqn. 3.18 induces the cell decomposition of* Ω*, Eqn. 3.19, such that the following* area-preserving constraints *are satisfied for all cells,*

$$\int_{W_i(\mathbf{h})} = \nu_i, i = 1, 2, \cdots, n. \tag{3.11}$$

Furthermore, the gradient map $grad\ u_{\mathbf{h}}$ *optimizes the following transportation cost*

$$\mathcal{C}(T) := \int_\Omega |x - T(x)|^2 \mu(x) dx. \tag{3.12}$$

The existence and uniqueness was first proven by Alexandrov [10] using a topological method; the existence was also proven by Argmstrong [16], the uniqueness and optimality was proven by Brenier [28].

Recently, Gu et al. [48] gives a novel proof for the existence and uniqueness based on the variational principle. The deep insight of variational framework provides us excellent opportunities for numerical implementation. We will take their approach and explore its engineering applications in this work.

Define the admissible space of height vectors

$$H_0 := \{\mathbf{h} | \sum_{j=1}^{k} h_j = 0\ and\ \int_{W_i(\mathbf{h})} \mu > 0, \forall i = 1, \cdots, k, \}.$$

Then define the energy $E(\mathbf{h})$,

$$E(\mathbf{h}) = \int_\Omega u_{\mathbf{h}}(x)\mu(x)dx - \sum_{i=1}^{k} \nu_i h_i. \tag{3.13}$$

or equivalently

$$E(\mathbf{h}) = \int_{\mathbf{0}}^{\mathbf{h}} \sum_{i=1}^{k} w_i(\eta) d\eta_i - \sum_{i=1}^{k} \nu_i h_i + C, \tag{3.14}$$

where C is a constant. Consider the shape bounded by the graph $G(\mathbf{h})$, the horizontal plane $\{x_{n+1} = 0\}$ and the cylinder consisting of vertical lines through $\partial\Omega$, the volume of the shape is given by the first term.

The gradient of the energy is given by

$$\nabla E(\mathbf{h}) = (w_1(\mathbf{h}) - \nu_1, \cdots, w_k(\mathbf{h}) - \nu_k)^T, \tag{3.15}$$

Suppose the cells $W_i(\mathbf{h})$ and $W_j(\mathbf{h})$ intersects at an edge $e_{ij} = W_i(\mathbf{h}) \cap W_j(\mathbf{h}) \cap \Omega$, then the Hessian of $E(\mathbf{h})$ is given by

$$\frac{\partial^2 E(\mathbf{h})}{\partial h_i \partial h_j} = \begin{cases} \frac{\int_{e_{ij}} \mu(x) dx}{|y_j - y_i|} & W_i(\mathbf{h}) \cap W_j(\mathbf{h}) \cap \Omega \neq \emptyset \\ 0 & otherwise \end{cases} \tag{3.16}$$

We focus on the Brenier's approach. Suppose μ has compact support on X, define $\Omega = supp\ \mu = \{x \in X | \mu(x) > 0\}$, assume Ω is a convex domain in X. The space Y is discretized to $Y = \{y_1, y_2, \cdots, y_k\}$ with Dirac measure $\nu = \sum_{j=1}^{k} \nu_j \delta(y - y_j)$.

We define a *height vector* $\mathbf{h} = (h_1, h_2, \cdots, h_n) \in \mathbb{R}^k$, consisting of k real numbers. For each $y_i \in Y$, we construct a hyperplane defined on X,

$$\pi_i(\mathbf{h}) : \langle x, y_i \rangle + h_i = 0. \tag{3.17}$$

Define a function

$$u_{\mathbf{h}}(x) = \max_{i=1}^{k} \{\langle x, y_i \rangle + h_i\}, \tag{3.18}$$

then $u_{\mathbf{h}}(x)$ is a convex function. We denote its graph by $G(\mathbf{h})$, which is an infinite convex polyhedron with supporting planes $\pi_i(\mathbf{h})$. The projection of $G(\mathbf{h})$ induces a polygonal partition of Ω,

$$\Omega = \bigcup_{i=1}^{k} W_i(\mathbf{h}), \tag{3.19}$$

where each cell $W_i(\mathbf{h})$ is the projection of a facet of the convex polyhedron $G(\mathbf{h})$ onto Ω,

$$W_i(\mathbf{h}) = \{x \in X | u_{\mathbf{h}}(x) = \langle x, y_i \rangle + h_i\} \cap \Omega. \tag{3.20}$$

Note that, this partition is equivalent to a power diagram, denoted as $D(\mathbf{h})$, as explained in [48]. The area of $W_i(\mathbf{h})$ is given by

$$w_i(\mathbf{h}) = \int_{W_i(\mathbf{h})} \mu(x) dx. \tag{3.21}$$

The convex function $u_{\mathbf{h}}$ on each cell $W_i(\mathbf{h})$ is a linear function $\pi_i(\mathbf{h})$, therefore, the gradient map

$$grad\ u_{\mathbf{h}} : W_i(\mathbf{h}) \to y_i, i = 1, 2, \cdots, k. \tag{3.22}$$

maps each $W_i(\mathbf{h})$ to a single point y_i.

The following theorem plays a fundamental role for discrete optimal mass transport theory,

Theorem 3.8. *Given a convex domain $\Omega \subset \mathbb{R}^n$, with measure density $\mu : \Omega \to \mathbb{R}$, and a discrete point set $Y = \{y_1, \cdots, y_k\}$ with discrete measures $\nu = \{\nu_1, \cdots, \nu_k\}$. Suppose $\sum_{j=1}^{n} \nu_j = \int_\Omega \mu, \nu_j > 0$.*

Then there must exist a height vector $\mathbf{h} = \{h_1, \cdots, h_k\}$ unique up to translations, such that the convex function Eqn. 3.18 induces the cell decomposition of Eqn. 3.19. And the following area-preserving constraints *are satisfied for all cells,*

$$\int_{W_i(\mathbf{h})} \mu(x) dx = \nu_i, i = 1, 2, \cdots, n. \tag{3.23}$$

Furthermore, the gradient map $grad\ u_{\mathbf{h}}$ optimizes the following transportation cost

$$\mathcal{C}(T) := \int_{\Omega} |x - T(x)|^2 \mu(x) dx. \tag{3.24}$$

The existence and uniqueness was first proven by Alexandrov [10] using a topological method; the existence was also proven by Argmstrong [16], the uniqueness and optimality was proven by Brenier [26]. Recently, Gu et al. [48] gives a novel proof for the existence and uniqueness based on the variational principle, which leads to the computational algorithm directly.

Define the admissible space of height vectors $H_0 := \{\mathbf{h} | \sum_{j=1}^{k} h_j = 0\ and\ \int_{W_i(\mathbf{h})} \mu > 0, \forall i = 1, \cdots, k, \}$. Then define the energy $E(\mathbf{h})$,

$$E(\mathbf{h}) = \int_{\Omega} u_{\mathbf{h}}(x)\mu(x)dx - \sum_{i=1}^{k} \nu_i h_i. \tag{3.25}$$

or equivalently

$$E(\mathbf{h}) = \int_{\mathbf{0}}^{\mathbf{h}} \sum_{i=1}^{k} w_i(\eta) d\eta_i - \sum_{i=1}^{k} \nu_i h_i + C, \tag{3.26}$$

where C is a constant. Consider the shape bounded by the graph $G(\mathbf{h})$, the horizontal plane $\{x_{n+1} = 0\}$ and the cylinder consisting of vertical lines through $\partial\Omega$, the volume of the shape is given by the first term.

The gradient of the energy is given by

$$\nabla E(\mathbf{h}) = \left(w_1(\mathbf{h}) - \nu_1, \cdots, w_k(\mathbf{h}) - \nu_k\right)^T, \tag{3.27}$$

Suppose the cells $W_i(\mathbf{h})$ and $W_j(\mathbf{h})$ intersects at an edge $e_{ij} = W_i(\mathbf{h}) \cap W_j(\mathbf{h}) \cap \Omega$, then the Hessian of $E(\mathbf{h})$ is given by

$$\frac{\partial^2 E(\mathbf{h})}{\partial h_i \partial h_j} = \begin{cases} \frac{\int_{e_{ij}} \mu(x) dx}{|y_j - y_i|} & W_i(\mathbf{h}) \cap W_j(\mathbf{h}) \cap \Omega \neq \emptyset \\ 0 & otherwise \end{cases}. \tag{3.28}$$

The following theorem lays down the theoretic foundation of our OMT map algorithm.

Theorem 3.9 (Discrete Optimal Mass Transport [48])**.** *If Ω is convex, then the admissible space H_0 is convex, so is the energy (Eqn. 3.25). Moreover, the unique global minimum $\mathbf{h}_0$ is an interior point of H_0. And the gradient map (Eqn. 3.22) induced by the minimum $\mathbf{h}_0$ is the unique optimal mass transport map, which minimizes the total transportation cost (Eqn. 3.24).*

The proof of Theorem 3.9 is reported in [48]. Due to the convexity of the volume energy Eqn. 3.25, With this theory, the global minimum can be obtained efficiently using Newton's method. Comparing to Kantorovich's approach, where there are $O(n^2)$ unknowns, this approach has only $O(n)$ unknowns.

3.2.3 Optimal Mass Transport Map (OMT-Map) Algorithm

Assume Ω is a convex planar domain with measure density μ, $P = \{p_1, \cdots, p_k\}$ is a point set with measure $\nu = \{\nu_1, \cdots, \nu_k\}$, such that $\int_\Omega \mu(x)dx = \sum_{i=1}^k \nu_i$.

According to the discussion in previous section, the OMT-Map can be obtained by minimizing the convex energy in Eqn. 3.25. In practice, the energy can be optimized using Newton's method, which requires the computation of the energy gradient using Eqn. 3.27, and the Hessian matrix using Eqn. 3.28. The method is straightforward, but the initialization and the step length selection need to be specially addressed.

Initialization. By translating and scaling, P could be inside Ω, $P \subset \Omega$. At the beginning, we set each power weight h_i to be 0, namely $\mathbf{h} = \mathbf{0}$, and compute the power diagram $D(P, \mathbf{h})$ and the Delaunay triangulation $T(P, \mathbf{h})$. In this scenario, $D(P, \mathbf{h})$ is a conventional voronoi diagram.

Step Length Selection. Suppose at the k-th step in the optimization, the power weight vector is $\mathbf{h}^k$, and all Voronoi cells $W_i(\mathbf{h}^k)$ are non-empty. Then the Hessian matrix H_k in Eqn. 3.28 is positive definite on the hyper-plane $\{\mathbf{h} | \sum_i h_i = 0\}$. At the $k+1$-step, we set the step length parameter λ as 1, and update the power weight vector

$$\mathbf{h}^{k+1} = \mathbf{h}^k - \lambda H_k^{-1} \nabla E(\mathbf{h}^k). \tag{3.29}$$

Then we compute the power diagram $D(P, \mathbf{h}^{k+1})$. If any Voronoi cell $W_i(\mathbf{h}^{k+1})$ disappears, then the Hessian matrix H_{k+1} will be degenerated. In this case, we shrink the step length parameter λ to be half, $\lambda \leftarrow \frac{1}{2}\lambda$. Then we recompute $\mathbf{h}^{k+1}$ using the formula in Eqn. 3.29 and test again. We repeat this procedure, until all Voronoi cells in $D(P, \mathbf{h}^{k+1})$ are non-empty. Algorithm 2 gives the implementation details.

3.2.4 Area-preserving Parameterization for Topological Disks

The OMT-Map algorithm can be generalized to compute the area-preserving mappings between surfaces. Suppose S is simply connected surface with a single boundary, namely a topological disk. S is with a Riemannian metric $\mathbf{g}$. By scaling, the total area of $(S, \mathbf{g})$ equals to π. Then according to the Riemann mapping theorem, there is a conformal mapping $\phi : (S, \mathbf{g}) \to (\mathbb{D}, dzd\bar{z})$, such that $\mathbf{g} = e^{2\lambda(z)} dzd\bar{z}$. Then we find a OMT-Map $\tau : (\mathbb{D}, dzd\bar{z}) \to (\mathbb{D}, e^{2\lambda} dzd\bar{z})$, then the composition $\tau^{-1} \circ \phi : (S, \mathbf{g}) \to (\mathbb{D}, dzd\bar{z})$ gives the area-preserving mapping.

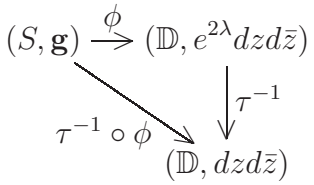

The smooth surface $(S, \mathbf{g})$ is approximated by a triangular mesh M, with vertex set $V = \{v_1, v_2, \cdots, v_k\}$. The conformal mapping ϕ can be computed using discrete surface Ricci

Algorithm 2 Optimal Mass Transport Map (OMT-Map)

Input: A convex planar domain with measure (Ω, μ); a planar point set with measure (P, ν), $\nu_i > 0$, $\int_\Omega u(x)dx = \sum_{i=1}^{k} \nu_i$; a threshold ϵ.
Output: The unique discrete OMT-Map $f : (\Omega, \mu) \to (P, \nu)$.

Scale and translate P, such that $P \subset \Omega$.
$\mathbf{h} \leftarrow (0, 0, \cdots, 0)$.
Compute the power diagram $D(\mathbf{h})$,
Compute the dual power Delaunay triangulation $T(\mathbf{h})$,
Compute the cell areas $\mathbf{w}(\mathbf{h}) = (w_1(\mathbf{h}), \cdots, w_k(\mathbf{h}))$.
repeat
  Compute $\nabla E(\mathbf{h})$ using Eqn. 3.27.
  Compute the Hessian matrix using Eqn. 3.28.
  $\lambda \leftarrow 1$
  $\mathbf{h} \leftarrow \mathbf{h} - \lambda H^{-1} \nabla E(\mathbf{h})$.
  Compute $D(\mathbf{h})$, $T(\mathbf{h})$ and $\mathbf{w}(\mathbf{h})$
  while $\exists w_i(\mathbf{h}) == 0$ **do**
    $\mathbf{h} \leftarrow \mathbf{h} + \lambda H^{-1} \nabla E(\mathbf{h})$.
    $\lambda \leftarrow 1/2\lambda$
    $\mathbf{h} \leftarrow \mathbf{h} - \lambda H^{-1} \nabla E(\mathbf{h})$.
    Compute $D(\mathbf{h})$, $T(\mathbf{h})$ and $\mathbf{w}(\mathbf{h})$.
  end while
until $\|\nabla E\| < \epsilon$.
return $f : \Omega \to P$, $W_i(\mathbf{h}) \to p_i$,$i = 1, 2, \cdots, k$.

flow method [139]. Then each vertex $v_i \in M$ is mapped to a planar point $p_i = \phi(v_i)$. The discrete measure ν_i is given by

$$\nu_i = \frac{1}{3} \sum_{[v_i, v_j, v_k] \in M} area([v_i, v_j, v_k]), \tag{3.30}$$

where $[v_i, v_j, v_k]$ is a face adjacent to v_i on the mesh. After normalization, the summation of the discrete measures, $\sum_i \nu_i$, equals to π. Then the OMT-Map $\tau : (\mathbb{D}, dxdy) \to (P, \nu)$ can be computed using Algorithm 4. The composition $\tau^{-1} \circ \phi$ is a discrete area-preserving mapping, which maps each vertex v_i on the mesh to the centroid of the corresponding cell W_i on the disk, such that the area of W_i equals to ν_i. The implementation details can be found in Algorithm 3. Figure 9 shows an examples.

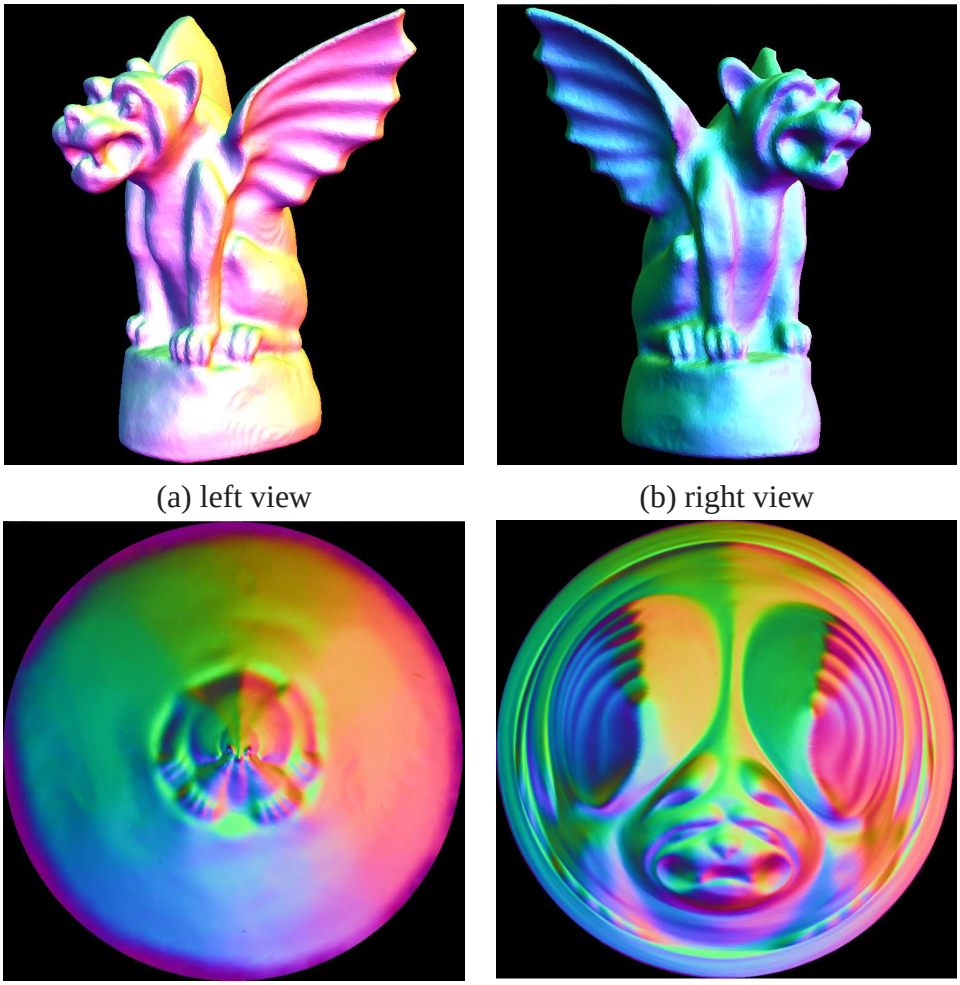

(a) left view (b) right view

(c) Angle-Preserving (CFP) (d) Area-Preserving (APP)

Figure 9: Topological disk area-preserving parameterization for the gargoyle model.

Algorithm 3 Topological Disk Area-preserving Parameterization

Input: A triangular mesh M which is a topological disk; three vertices $\{v_0, v_1, v_2\} \subset \partial M$ on the boundary.

Output: The area-preserving parameterization $f : M \to \mathbb{D}$, which maps $\{v_0, v_1, v_2\}$ to $\{1, i, -1\}$ respectively.

1. Scale M such that its total area equals to π.
2. Compute the conformal parameterization $\varphi : M \to \mathbb{D}$, such that the images of $\{v_0, v_1, v_2\}$ are $\{1, i, -1\}$ respectively.
3. For each vertex $v_i \in M$, define $p_i = \varphi(v_i)$, ν_i to be $1/3$ of the total area of the faces adjacent to v_i. Set $P = \{p_i\}$, $\nu = (\nu_i)$.
4. Compute the DOTM $\tau : \mathbb{D} \to (P, \mu)$ using Algorithm 4.
5. Construct the mapping $\tau^{-1} \circ \phi : M \to \mathbb{D}$, which maps each vertex $v_i \in M$ to the centroid of $W_i(\mathbf{h}) \subset \mathbb{D}$.

3.2.5 Area-preserving Parameterization for Topological Spheres

Suppose $(S, \mathbf{g})$ is a closed genus zero metric surface, namely a topological sphere, with total area 4π. Given three points $\{p_1, p_2, p_3\} \subset S$, there is a unique conformal mapping $\phi : S \to \hat{\mathbb{C}}$, where $\hat{\mathbb{C}}$ is the augmented complex plane $\mathbb{C} \cup \{\infty\}$, such that ϕ maps the three points to $\{0, 1, \infty\}$ respectively, furthermore the original surface metric $\mathbf{g} = e^{2\lambda} dz d\bar{z}$.

Consider the unit sphere $\mathbb{S}^2$ embedded in $\mathbb{R}^3$, it has the induced Euclidean metric $\mathbf{h}$. Let $\psi : \mathbb{S}^2 \to \hat{\mathbb{C}}$ be the stereo-graphic projection, then

$$\mathbf{h} = \frac{4dzd\bar{z}}{(1 + z\bar{z})^2}, \mu = \frac{4dudv}{(1 + u^2 + v^2)^2}$$

where μ is measure induced by $\mathbf{h}$, $z = u + iv$.

Let $\tau : ((\hat{\mathbb{C}}, \frac{4dzd\bar{z}}{(1+z\bar{z})^2}) \to (\hat{\mathbb{C}}, e^{2\lambda} dz d\bar{z}))$ be the optimal mass transport map, then the composition $\psi^{-1} \circ \tau^{-1} \circ \phi : (S, \mathbf{g}) \to (\mathbb{S}^2, \mathbf{h})$ is an area-preserving mapping.

$$\begin{array}{ccc} (S, \mathbf{g}) & \xrightarrow{\psi^{-1} \circ \tau^{-1} \circ \phi} & (\mathbb{S}^2, \mathbf{h}) \\ \downarrow \phi & & \downarrow \psi \\ (\hat{\mathbb{C}}, e^{2\lambda} dz d\bar{z}) & \xrightarrow{\tau^{-1}} & (\hat{\mathbb{C}}, \frac{4dzd\bar{z}}{(1 + z\bar{z})^2}) \end{array}$$

The surface is approximated by a triangle mesh M, the conformal mapping $\phi : S \to \hat{\mathbb{C}}$ is obtained by two steps. First, the mesh is conformally mapped to the unit sphere

using spherical harmonic mapping method in [51]; secondly, the unit sphere is conformally mapped onto the augmented complex plane $\hat{\mathbb{C}}$ using the stereo-graphic projection. Then the discrete point set P consists $p_i = \phi(v_i)$. The discrete measure ν_i for each vertex is computed using the same formula as Eqn. 3.30.

The OMT-Map $\tau : (\hat{\mathbb{C}}, \frac{4dzd\bar{z}}{(1+z\bar{z})^2}) \to (P, \nu)$ can be carried out using the same Algorithm 4. The sharp distinction is that the domain Ω here is infinite, the entire complex plane. Some cells are unbounded, but still with finite areas under the spherical measure μ.

In order to use Newton's method for the optimization, for each cell, we need to compute the spherical area and the spherical edge lengths. Consider a finite polygon G first, suppose its edges are $\{s_1, \cdots, s_m\}$ the exterior angles are $\{\theta_1, \cdots, \theta_m\}$. Because ψ is conformal, so the exterior angles are well preserved on the sphere, and each segment is mapped to curve segment, which is unnecessary to be a geodesic. According to Gauss-Bonnet theorem, $\int_G KdA + \sum_i \int_{s_i} k_g ds + \sum_j \theta_j = 2\pi$, where K is the Gaussian curvature, k_g is the geodesic curvature. Because $\sum_j \theta_j = 2\pi$, $K = +1$, we obtain $Area(G) = -\sum_i \int_{s_i} k_g ds$. where $\sum_i \int_{s_i} k_g ds$ can be easily and efficiently computed by spherical geometry. For an infinite cell G, there are two infinite edges, which intersect at the ∞ point. Suppose their intersection angle between two rays is θ, then the exterior angle at ∞ is $\pi - \theta$. The other part of the computation is similar to the finite cell case. The implementation is quite similar to Algorithm 3 except that we need to compute an additional stereo-graphic projection (ψ) and consider infinite cell G when computing the cell areas $\mathbf{w}(\mathbf{h})$.

3.2.6 Riemannian optimal mass transport map

This section gives the algorithmic implementation details for Riemannian optimal mass transport map (OMT-Map) generation using geodesic power Voronoi diagram.

Smooth metric surfaces can be approximated by piecewise linear triangle mesh. There are many ways to discretize a smooth surface, such that the piecewise linear metrics converge to the smooth metric, eg, the sampling is uniform and the triangulation is geodesic Delaunay. The geodesics on the triangle meshes can be efficiently computed using the algorithms in [130].

First, we repeat subdividing the triangle mesh until the size of each triangle is small enough to ensure the accuracy. Then from each point p_i in the point set P, we compute the geodesics to reach every other vertex on the subdivided mesh, this gives the geodesic distance from every vertex to p_i. Repeat this for all vertices in P.

Third, we find the optimal weight. We initialize all the weights to be zeros, then update the weight using the formula

$$\frac{dh_i}{dt} = \nu_i - \int_{W_i(\mathbf{h})} \mu(p)dp.$$

Details of the algorithm can be found in Alg. 4.

Algorithm 4 Riemannian Optimal Mass Transport Map

Input: A triangle mesh M, measure μ and Dirac measure $\{(p_1, \nu_1), (p_2, \nu_2), \cdots, (p_k, \nu_k)\}$, $\int_M u(p)dp = \sum_{i=1}^{k} \nu_i$; a threshold ϵ.
Output: The unique discrete Optimal Mass Transport Map $T : (M, \mu) \to (P, \nu)$.

Subdivide M for several levels, until each triangle size is small enough.
for all $p_i \in P$ **do**
  Compute the geodesic from p_i to every other vertex on M,
end for
$\mathbf{h} \leftarrow (0, 0, \cdots, 0)$.
repeat
  for all vertex v_j on M **do**
    Find the minimum weighted squared geodesic distance, decide which Voronoi cell v_i belongs to, $v_i \in W_t(\mathbf{h})$

$$t = argmin_k d^2_{\mathbf{g}}(v_j, p_k) + h_k$$

  end for
  for all $p_i \in P$ **do**
    Compute the current cell area $w_i = \int_{W_i(\mathbf{h})} d\mu$,
  end for
  for all $h_i \in \mathbf{h}$ **do**
    Update h_i, $h_i = h_i + \delta(\nu_i - w_i)$
  end for
until $|\nu_i - w_i| < \epsilon$, $\forall i$.
return Power geodesic Voronoi diagram.

3.2.7 Conformal Wasserstein Distance

The OMT-Map algorithm can also be generalized to compute the Wasserstein distance between surfaces. Given two topological disk surfaces $(M_1, g_1, p_1, q_1) \in \mathcal{S}$, $(M_2, g_2, p_2, q_2) \in \mathcal{S}$ with total area π, where $\mathcal{S}$ is the normalized marked metric space defined in Eqn. 2.56. p_1 and p_2 are correspondent interior markers, and q_1 and q_2 are correspondent boundary markers. We first compute the conformal maps $\phi_1 : M_1 \to \mathbb{D}_1$ and $\phi_2 : M_2 \to \mathbb{D}_2$, where $\mathbb{D}_1$ and $\mathbb{D}_2$ are the unit planar disks with Euclidean metric $dx^2 + dy^2$, such that $\phi(p_1) = \phi(p_2) = (0, 0)$ and $\phi(q_1) = \phi(q_2) = (1, 0)$. Then we construct a convex planar domain (Ω, μ) from $\mathbb{D}_1$, where μ is computed by Eqn. 2.57. And then we discretize $\mathbb{D}_2$ into a planar point set with measure (P, ν), where ν is computed by Eqn. 3.30. Using (Ω, μ) and

(P, ν) as inputs of Algorithm 4, we compute the Optimal Mass Transport map $f : \Omega \to P$, $W_i(\mathbf{h}) \to p_i$, where $p_i \in P, i = 1, 2, \cdots, k$. Therefore, the Wasserstein distance between M_1 and M_2 can be computed by

$$Wasserstein(\mu, \nu) = \sum_{i=1}^{n} \int_{W_i} (x - p_i)^2 \mu(x) dx \tag{3.31}$$

Algorithm 5 gives the implementation details.

Algorithm 5 Computing Wasserstein Distance

Input: Two topological disk surfaces (M_1, g_1, p_1, q_1), (M_2, g_2, p_2, q_2). p_1 and p_2 are correspondent interior markers, and q_1 and q_2 are correspondent boundary markers.
Output: The Wasserstein distance between M_1 and M_2.

1. Scale and normalize M_1 and M_2 such that the total area of each surface is π.
2. Compute the conformal maps $\phi_1 : M_1 \to \mathbb{D}_1$ and $\phi_2 : M_2 \to \mathbb{D}_2$, where $\mathbb{D}_1$ and $\mathbb{D}_2$ are the unit planar disks with Euclidean metric $dx^2 + dy^2$, such that $\phi(p_1) = \phi(p_2) = (0, 0)$ and $\phi(q_1) = \phi(q_2) = (1, 0)$.
3. Construct a convex planar domain (Ω, μ) from $\mathbb{D}_1$, where μ is computed by Eqn. 2.57.
4. Discretize $\mathbb{D}_2$ into a planar point set with measure (P, ν), where ν is computed by Eqn. 3.30.
5. With (Ω, μ) and (P, ν) as inputs of Algorithm 4, we compute the Optimal Mass Transport map $f : \Omega \to P$, $W_i(\mathbf{h}) \to p_i$, where $p_i \in P, i = 1, 2, \cdots, k$.
6. Wasserstein distance between M_1 and M_2 can be computed by Eqn. 3.31.

3.2.8 Polar Factorization

Conformal parameterizations have no angle distortions, but they may induce large area distortions. For cylindrical shapes, the area distortions can be exceptional large in terms of the cylinder height. The huge area distortions cause severe numerical instability and aliasing in rendering. On the other hand, area-preserving parameterizations has no area distortions, but they may cause huge angle distortions. In digital geometry processing, many geometric tasks boil down to solve geometric partial differential equations on the surface. The geometric PDEs are converted to sparse linear systems using Finite Element Method. The

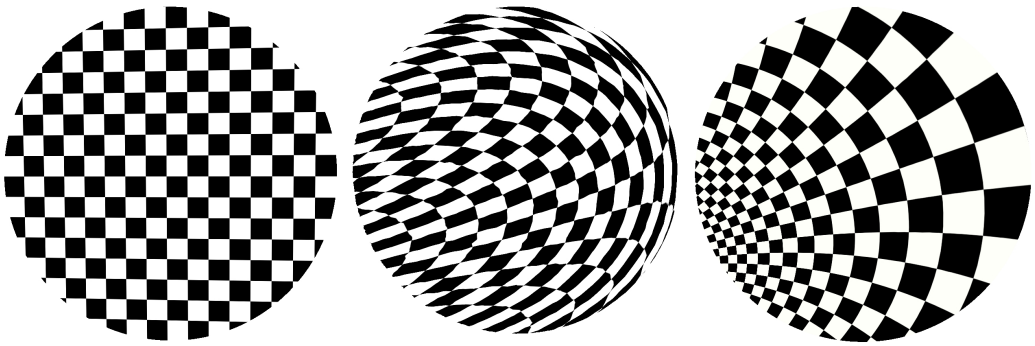

(a) Ω (b) area-preserving s (c) φ

Figure 10: Polar factorization.

numerical stability of the linear systems heavily depends on the angle structure of the discrete triangular mesh. If the triangulation has too many obtuse angles, the linear system is highly unstable, and the computational results are not reliable.

Therefore, the parameterization with a good balance between angle distortion and area distortion is highly preferred. The polar factorization of general surface mapping method has great promise to tackle this challenging problem. Given a diffeomorphism φ, it can be decomposed into the composition of two mappings

$$\varphi = \nabla u \circ s, \tag{3.32}$$

where s is area-preserving, u is a convex function and the gradient map ∇u deforms the area in the most economical way (an optimal mass transportation map). The convex function u and the optimal mass transportation map ∇u are solely determined by the source and the target mass density functions. This gives a practical way to control the area distortion.

Suppose the initial map φ is conformal, by varying the convex function u, we can deform φ to s, namely we build a path φ_t in the mapping space, connecting the angle preserving mapping $\varphi_1 = \varphi$ to the area preserving mapping $\varphi_0 = s$. By choosing the parameter t, one can find the optimal parameterization φ_t, most appropriate for the application.

The mapping polar factorization can be treated as the generalization of matrix polar decomposition and vector field Helmholtz decomposition. Suppose (Ω_0, μ_0) and (Ω_1, μ_1) are subdomains in the Euclidean space $\mathbb{R}^d$, $\varphi : \Omega_0 \to \Omega_1$ is a diffeomorphism between them. Then there is a convex function $u : \Omega_0 \to \mathbb{R}$, whose gradient map $\nabla u : x \mapsto \nabla u(x)$ maps from Ω_0 to Ω_1. Furthermore, there is a volume-preserving mapping $s : \Omega_0 \to \Omega_0$, such that φ can be decomposed to $\varphi = \nabla u \circ s$. This decomposition is unique. As shown in Fig.10, a conformal mapping φ in (c) is decomposed to an area preserving mapping from (a) to (b) and a gradient map from (b) to (c).

If the source domain coincides with the target domain, denoted as Ω, then all the volume-preserving diffeomorphisms form a Lie group $S(\Omega)$, which is non-convex. Given a diffeomorphism $\varphi : \Omega \to \Omega$ with polar decomposition $\varphi = \nabla u \circ s$, s is the unique L^2 projection onto $S(\Omega)$. Assume Ω has a volume form (measure) μ, then φ induces a push forward measure $\varphi_{\#}\mu$, ∇u is the unique optimal mass transportation map from (Ω, μ) to $(\Omega, \varphi_{\#}\mu)$.

The following polar factorization theorem plays a fundamental role in the current project.

Theorem 3.10 (Polar Factorization [26])**.** *Let Ω_0 and Ω_1 be two convex subdomains of $\mathbb{R}^n$, with smooth boundaries, each with a positive density function, μ_0 and μ_1 respectively, with the same total mass $\int_{\Omega_0} \mu_0 = \int_{\Omega_1} \mu_1$. Let $\varphi : (\Omega_0, \mu_0) \to (\Omega_1, \mu_1)$ be an diffeomorphic mapping, then φ has a unique decomposition of the form*

$$\varphi = (\nabla u) \circ s, \tag{3.33}$$

where $u : \Omega_0 \to \mathbb{R}$ is a convex function, $s : (\Omega_0, \mu_0) \to (\Omega_0, \mu_0)$ is an measure-preserving mapping. This is called the polar factorization of φ with respect to μ_0.

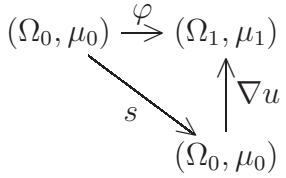

This means a general diffeomorphism $\varphi : (\Omega_0, \mu_0) \to (\Omega_1, \mu_1)$, where $\mu_1 = \varphi_{\#}\mu_0$ can be decomposed to the composition of a measure preserving map $s : (\Omega_0, \mu_0) \to (\Omega_0, \mu_0)$ and a L^2 optimal mass transportation map $\nabla u : (\Omega_0, \mu_0) \to (\Omega_1, \mu_1)$. This decomposition is unique. Furthermore, if Ω_0 coincides with Ω_1, then s is the unique L^2 projection of φ in the space of all measure preserving mappings of (Ω_0, μ_0). Namely, τ minimizes the L^2 distance among all measure preserving mappings,

$$s = argmin_{\tau} \int_{\Omega_0} \|\varphi(x) - \tau(x)\|^2 \mu_0(x) dx, \;\; \tau_{\#}\mu_0 = \mu_0.$$

Given a diffeomorphism $\varphi : (\Omega_0, \mu_0) \to (\Omega_1, \mu_1)$, such that $\varphi_{\#}\mu_0 = \mu_1$, there is a unique polar factorization $\varphi = \nabla u \circ s$, where $s : (\Omega_0, \mu_0) \to (\Omega_0, \mu_0)$ is measure preserving, $s_{\#}\mu_0 = \mu_0$; $\nabla u : (\Omega_0, \mu_0) \to (\Omega_1, \mu_1)$ is an L^2 optimal mass transportation map, u is a convex function $u : \Omega_0 \to \mathbb{R}$.

Because $\nabla u : (\Omega_0, \mu_0) \to (\Omega_1, \mu_1)$ is the unique optimal mass transportation map, then $\nabla u^* = (\nabla u)^{-1} : (\Omega_1, \mu_1) \to (\Omega_0, \mu_0)$ is the unique optimal transportation map as well. So in our algorithm, we fist compute an optimal mass transportation $(\nabla u)^{-1}$ first. The measure-preserving map s can be computed direction by

$$s = (\nabla u)^{-1} \circ \varphi. \tag{3.34}$$

Algorithm 6 Polar Factorization of Mapping

Require: Convex domains Ω_0 and Ω_1 in $\mathbb{R}^d$. A diffeomorphic mapping $\varphi : (\Omega_0, \mu_0) \to (\Omega_1, \mu_1)$, where $\varphi_{\#}\mu_0 = \mu_1$.

Ensure: The polar factorization $\varphi = \nabla u \circ s$, where s is an measure-preserving mapping, u is a convex function defined on Ω_0.

1: Compute the unique optimal mass transportation map $\nabla v : (\Omega_1, \mu_1) \to (\Omega_0, \mu_0)$ using Alg.2. The convex function u is the Legendre dual of v, $u = v^*$.

2: Compute the composition $s = \nabla v \circ \varphi$.

The algorithm is summarized in Alg.6.

One direct application of mapping polar factorization is to construct a sequence of mesh parameterizations with balanced angle vs area distortions. Suppose $(M, \mathbf{g})$ is a metric surface, for simplicity, we assume M is a topological disk. By scaling, the total area of M is π. We would like to construct one parameter family of diffeomorphic mappings $\varphi_t : (M, \mathbf{g}) \to (\mathbb{D}, dzd\bar{z})$, such that φ_0 is area preserving, and φ_1 is angle preserving. For any $0 < t < 1$, φ_t is a diffeomorphism, with different level of angle and area distortions.

The following is the computational method. First, we apply discrete surface Ricci flow algorithm to compute a Riemann mapping φ_1 from the surface to the unit disk. Then we compute the polar factorization of φ_1,

$$\varphi_1 = \nabla u_1 \circ \varphi_0,$$

where φ_0 is the area-preserving mapping, u_1 is the convex function.

Because φ_1 is conformal, the area element μ_1 has the form $\mu_1 = e^{2\lambda} dxdy$. φ_0 is area preserving, the area element μ_0 is $\mu_0 = dxdy$. We linearly interpolate μ_0 and μ_1,

$$\mu_t = (1-t)\mu_0 + t\mu_1,$$

and compute the optimal mass transportation $\nabla u_t : (\mathbb{D}, \mu_0) \to (\mathbb{D}, \mu_1)$, then we obtain the mapping

$$\varphi_t := \nabla u_t \circ \varphi_0.$$

Alternatively, when $t = 0$, ∇u_0 is the identity map, therefore $u_0 = \frac{1}{2}(x^2 + y^2)$ on the unit disk. Then we define u_t as the Minkowski sum of $(1-t)u_0$ and tu_1,

$$u_t := (1-t)u_0 \oplus tu_1.$$

In practice, the convex function is represented as upper envelope of supporting planes,

$$u_1(x) := \max_i \{\langle p_i, x\rangle + h_i\}, u_0(x) := \max_i \{\langle p_i, x\rangle - \frac{1}{2}\langle p_i, p_i\rangle\},$$

therefore

$$u_t(x) = \max_i \{\langle p_i, x\rangle + \frac{t-1}{2}\langle p_i, p_i\rangle + th_i.$$

In Figure 11 and 12 we show the comparisons among conformal map, Optimal mass transport map and polar factorization maps. For the polar factorization map ϕ_t, we show a sequence of maps when $t = 1.0$, $t = 0.75$, $t = 0.5$, $t = 0.25$ and $t = 0$. The second column shows the different parameterization results. We can see that when t increases, polar factorization map is closer to conformal map, and when t decreases, polar factorization map is closer to Optimal mass transport mapping. The third column and fourth column illustrate the histograms of angle distortion and area distortion, respectively. When t increases, the angle distortion becomes smaller and area distortion becomes larger. When t decreases, the angle distortion becomes larger and area distortion becomes smaller. These quantitative results show how the polar factorization map balances between angle distortion and area distortion, and demonstrate the flexibility, accuracy and numerical stability of polar factorization map.

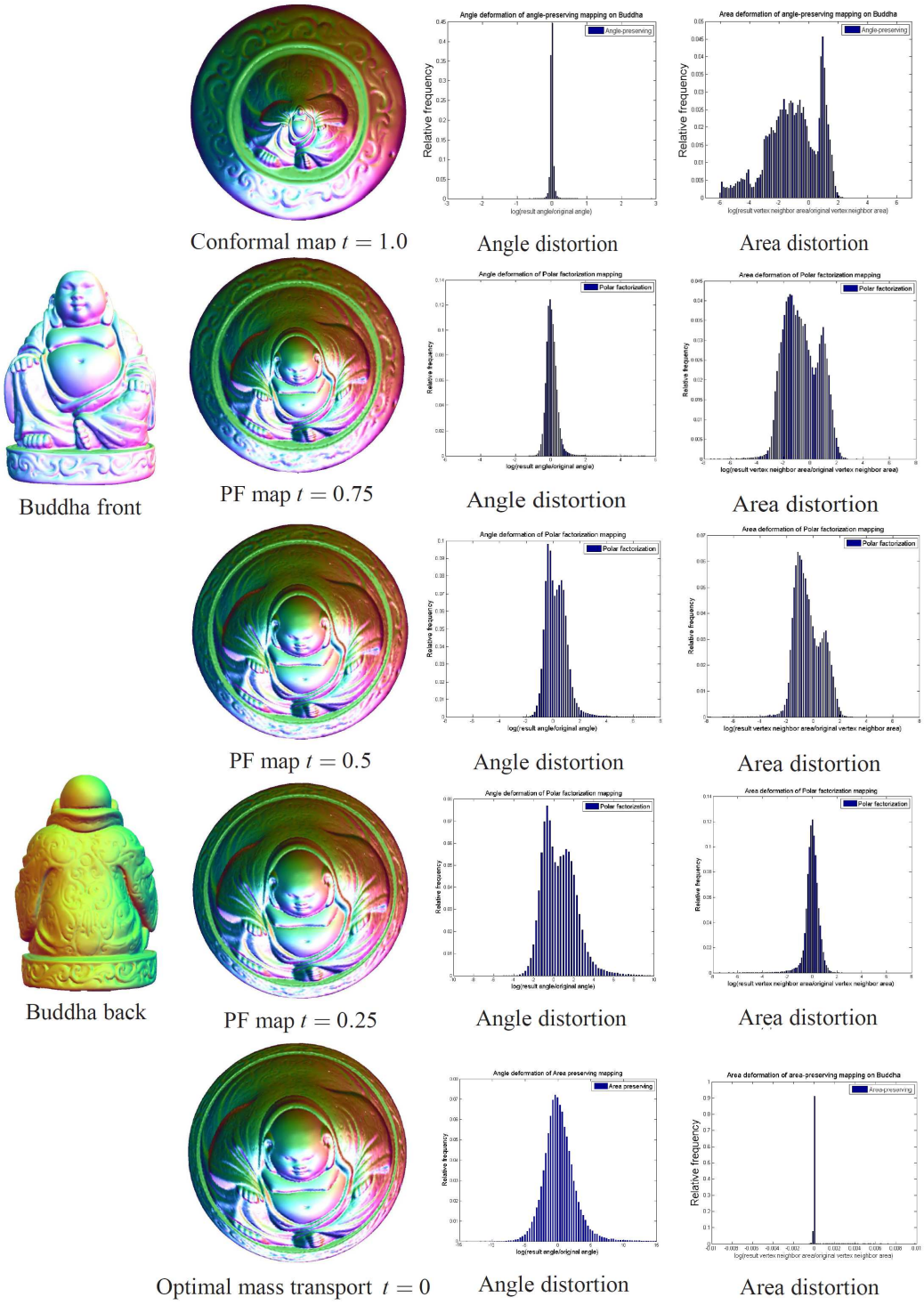

Figure 11: Comparisons among Conformal mapping, Optimal mass transport map and Polar factorization mapping (PF map) φ_t under different degree of compositions, on Buddha models.

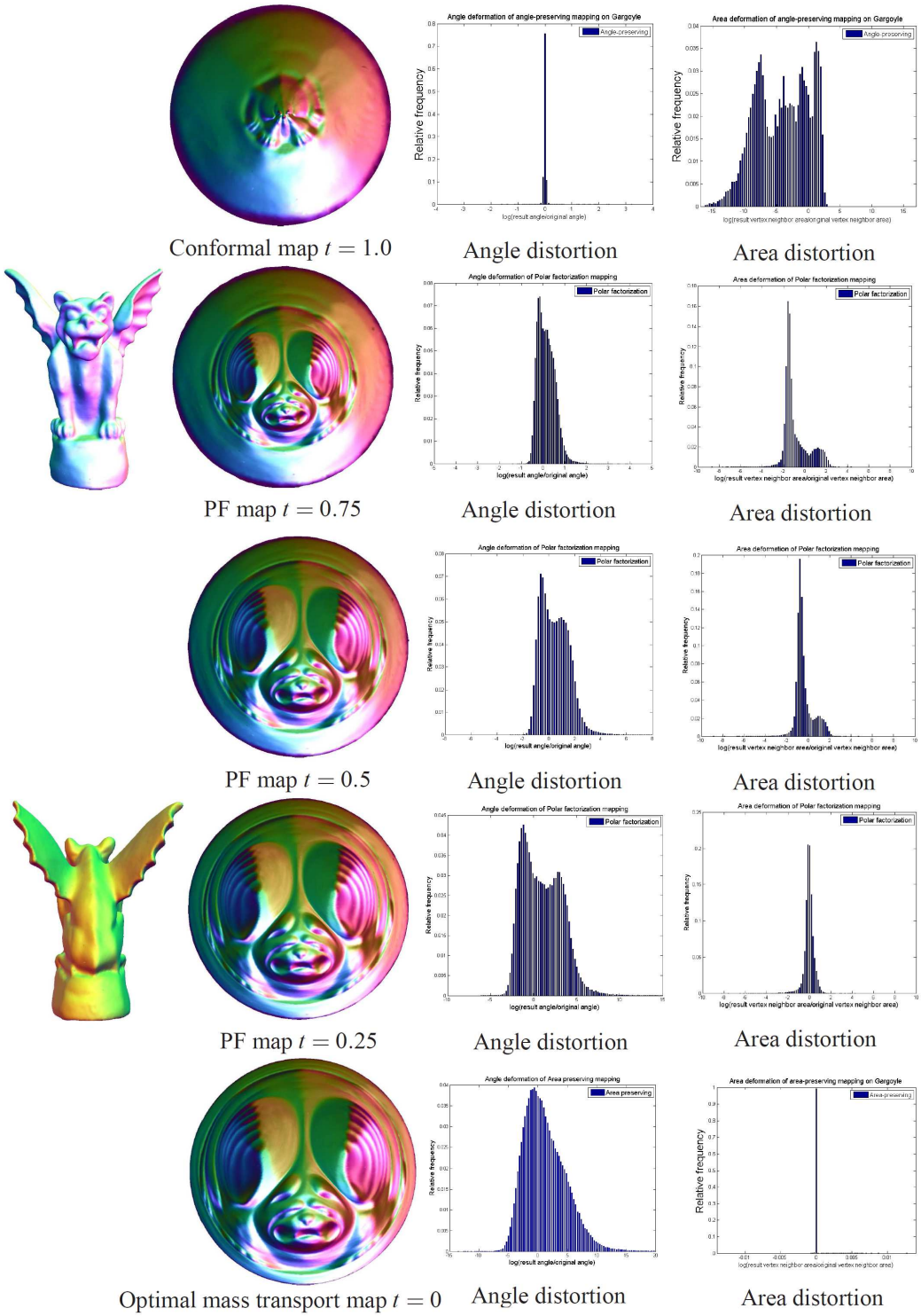

Figure 12: Comparisons among Conformal mapping, Optimal mass transport map and Polar factorization mapping (PF map) φ_t under different degree of compositions, on Gargoyle models.

4 Optimal Mass Transport for Shape Analysis

Surface based 3D shape analysis plays a fundamental role in computer vision and medical imaging. This work proposes to use optimal mass transportation maps for shape analysis, focusing on two important shape analysis applications including surface registration and shape space. The computation of the optimal mass transport map is based on Monge-Brenier theory, in comparison to the conventional method based on Monge-Kantorovich theory, this method significantly improves the efficiency by reducing computational complexity from $O(n^2)$ to $O(n)$. For surface registration problem, one commonly used approach is to use conformal map to convert the shapes into some canonical space. Although conformal mappings have small angle distortions, they may introduce large area distortions which are likely to cause numerical instability thus resulting failures of shape analysis. This work proposes to compose the conformal map with the optimal mass transportation map to get the unique area-preserving map, which is intrinsic to the Riemannian metric, unique, and diffeomorphic. For shape space study, this work introduces a novel Riemannian framework, *Conformal Wasserstein Shape Space*, by combing conformal geometry and optimal mass transportation theory. In our work, all metric surfaces with the disk topology are mapped to the unit planar disk by a conformal mapping, which pushes the area element on the surface to a probability measure on the disk. The optimal mass transportation provides a map from the shape space of all topological disks with metrics to the Wasserstein space of the disk and the pullback Wasserstein metric equips the shape space with a Riemannian metric. We validate our work by numerous experiments and comparisons with prior approaches and the experimental results demonstrate the efficiency and efficacy of our proposed approach.

4.1 Overview

In recent decades, with the fast development of 3D scanning technologies, there has been much research into surface representations for 3D shape analysis. Comparing with other approaches such as volume measurements [67], mathematical morphology [64], medial axis [22], surface based approach offers many advantages including: (1) it offers an accurate shape representation even for local subtle shape changes; (2) it can compute some physically natural measurements, e.g. elasticity and heat diffusion; (3) it has solid mathematical foundations on which one can develop numerically efficient algorithms and achieve global shape analysis, even on shapes with complicated topology structures. In computer vision research, numerous surface based approaches have been proposed to solve various shape analysis problems, such as surface matching [41, 21, 29, 86, 90, 112, 82], anatomical morphometry analysis [119], 3D object recognition and tracking [77, 132] and 3D shape

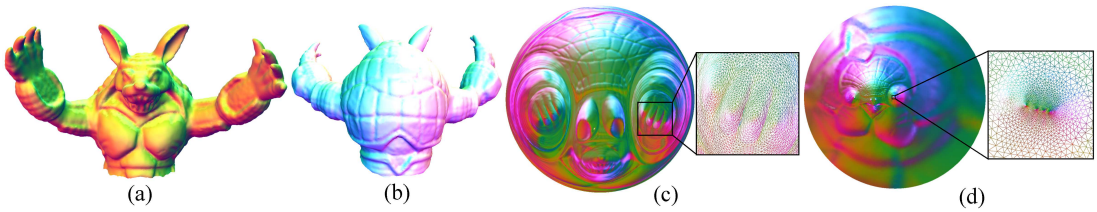

Figure 13: Comparison of geometric mappings for Armadillo surface model to a planar unit disk: (a) Front view; (b) Back view; (c) Optimal mass transport map result; (d) Conformal mapping result. The results show that conformal mapping has much more area distortions on head and hands areas. The normal information on the original surfaces is preserved and used for rendering. By the shading information on the planar domain ((c) and (d)), the correspondence is illustrated. The hand zoom-in image of (d) shows that the conformal map shrinks the fingers to very tiny areas which may cause numerical instability, while the hand zoom-in image of (c) demonstrates the optimal mass transport method gives a good one-to-one mapping result.

search engine [30]. Even so, a theoretically rigorous and numerically efficient surface based approach would be highly advantageous in this research field. Here we propose to apply the Monge-Brenier optimal mass transportation theory for shape analysis, focusing on surface registration and a generic shape space model, conformal Wasserstein shape space.

Optimal Mass Transport Monge raised the classical *Optimal Mass Transport Problem* that concerns determining the optimal way, with minimal transportation cost, to move a pile of soil from one place to another [24].

Kantorovich [78] has proved the existence and uniqueness of the optimal transport plan based on linear program. Monge-Kantorovich optimization has been used in numerous fields from physics, econometrics to computer science including data compression and image processing [104]. Recently, researchers have realized that optimal transport could provide a powerful tool in image processing, if one could reduce its high computational cost [38, 126]. However, it has one fundamental disadvantage that the number of variables is $O(k^2)$, which is unacceptable to computer vision and medical imaging applications since a high resolution 3D surface normally includes up to hundreds of thousands of vertices.

An alternative Monge-Brenier optimization scheme can significantly reduce the number of variables to be optimized. In late 1980's, Brenier [28] developed a different approach for a special class of optimal transport problems, where the cost function is quadratic distance. Brenier's theory shows that the optimal transport map is the gradient map of a special convex function. Assume the target domain is discretized to n samples, the Monge-Brenier's approach reduces the unknown variables from $O(n^2)$ to $O(n)$, which greatly reduces the

computation cost, and improves the efficiency. In our framework, we take Monge-Brenier's approach. However, our work is based on the newly discovered variational principle [48] which is the underspinning of Monge-Brenier's approach. Our framework is general and works with any valid measures, μ and ν, defined on two surfaces. Within the scope of this paper, we only consider the area induced measures. As a result, we will use the term *OMT-Map* and *area-preserving map* interchangeably. Our parameter domains could be either topological disk (including rectangles and any convex planar domain) (Figure 13 and 14) or topological sphere domains (Figure 15).

Surface Registration. Studying the original surfaces could be extremely difficult when shapes are irregular and very complex, such as human body or human brain cortical surfaces. One effective and common approach is to first parameterize the original 3D domain to some classical parameter domains, such as planar or spherical domain, then register or analyze 3D surfaces through these canonical spaces [110, 41, 142]. This approach has the advantage of converting complex shapes to simple ones, reducing the computational complexity and improving the efficiency. Conformal geometry based methods have been frequently applied for shape parameterizations [25, 93, 51, 111, 132, 139, 69, 11]. Conformal mapping can keep angle unchanged and preserve local shapes (conformal), but may also produce huge area distortions. In Figure 13, the Armadillo model is mapped onto the planar unit disk. Frame (d) shows the image of a conformal mapping, where the head area shrunk exponentially to the height of the model and hard to be recognized. Other extruding parts, such as hands with fingers shown in the zoom-in image, the exponential area distortions may easily exceed machine precisions, leading to problems and failure of surface matching and registration.

The conformal mapping in (d) pushes forward the area element on the Armadillo model to the planar disk. Then the unique optimal transportation map is carried out from the disk with the push-forward measure in (d) to the disk with Euclidean measure. The composition of the conformal mapping and the optimal transportation map is an area-preserving map from the surface to the Euclidean disk. The mapping result is shown in (c), where the head and figures occupy the same areas as those on the original surface. Area-preserving mapping avoids the huge area distortion, therefore is more robust and intuitive for processing. Furthermore, this area-preserving mapping is intrinsic to the Riemannian metric, unique, and diffeomorphic. Therefore, the OMT map may help provide practical solutions for general 3D shape analysis tasks, such as surface parameterization, surface matching and surface morphometry studies.

Conformal Wasserstein Shape Space. Shape space models provide suitable mathematical and computational descriptions for both shape representation and comparisons [79] and they were actively studied in computer vision field (as reviewed in [136]). With the proposed optimal transport theory, here we present its application for modeling shape spaces and measuring shape distances.

Let $(M, \mathbf{g})$ be a Riemannian manifold, $\mathcal{P}(M)$ is the space of all probability measures defined on M. Given two measures $\mu, \nu \in \mathcal{P}(M)$, there is an optimal mass transportation

map $T : M \to M$, the transportation cost of T is defined as the Wasserstein distance between μ and ν, denoted as $W(\mu, \nu)$. It can be shown that W is a metric of the Wasserstein space $\mathcal{P}$, the pair $(\mathcal{P}(M), W)$ is called the Wasserstein metric space, which reflects the Riemannian metric of $(M, \mathbf{g})$.

Consider a marked metric surface with the disk topology $(s, \mathbf{g})$, with two markers (p, q), $p \notin \partial M$, $q \in \partial M$, there is a unique conformal mapping $\varphi : s \to \mathbb{D}$, φ maps p and q to 0 and 1 respectively. The corresponding conformal factor induced by φ is $\lambda : \mathbb{D} \to \mathbb{R}$. The area element of s is pushed forward to the disk, represented as $\mu_{(s,\mathbf{g})} := e^{2\lambda}(x, y)dx \wedge dy$. Then we convert a marked metric surface to a probability measure $\Gamma : (s, \mathbf{g}) \mapsto \mu_{(s,\mathbf{g})}$.

All the marked metric surfaces with the disk topology quotient the isometry group and the scaling transformation group form the shape space $\mathcal{S}$. The mapping $\Gamma : \mathcal{S} \to \mathcal{P}(\mathbb{D})$ is an injective mapping, the pull back metric induced by Γ gives a Riemannian metric in $\mathcal{S}$. We call this metric space $(\mathcal{S}, \Gamma^* W_2)$ as the *Conformal Wasserstein Shape Space*.

The conformal Wasserstein shape space is a novel Riemannian framework to study shape space. This framework has solid theoretic foundation and efficient computational algorithms. It may provide a metric space for shape comparison, shape clustering and classification, shape retrieval and so on.

Advantages To our knowledge, this work is the first one to take Monge-Brenier theory to study 3D shape analysis problems. It has the following merits:

1. *Theoretic soundness:* According to convex geometry theorem developed by Brenier [28] and earlier work by Alexandrov [10], the solution exists and is unique. Furthermore, the area of each cell equals to the prescribed measure exactly. When the sampling density goes to infinity, the Alexandrov maps converge to the continuous area-preserving map.

2. *Generality and efficiency:* The method is general for arbitrary dimension, which has the potential to lead to high dimensional parameterizations. For surface case, it can handle both topological disks and topological spheres and achieve bijective surface mapping. Comparing to the conventional Monge-Kantorovich method, our approach reduces the complexity from $O(n^2)$ to $O(n)$. It is equivalent to a convex optimization problem, which can be carried out using Newton's method efficiently. Since the computation is based on classical power diagram, the algorithm can be implemented using any existing numerical software package easily.

3. *Flexibility:* Our algorithm can take different canonical space as the parameter domain.

4.2 Related Work

Optimal Mass Transport

For optimal mass transport, some approaches based on Monge-Kantorovich theory have been proposed. Zhu et al. [147] applied optimal mass transport for flattening blood vessel in an area preserving mapping for medical visualization. Haker et al. [59] proposed to use optimal mass transport for image registration and warping, the method is parameter free and has the unique global optimum. Dominitz and Tannenbaum [38] proposed to use optimal mass transport for texture mapping. The method first starts with an angle-preserving mapping and then refines the mapping using the mass transport procedure derived via a gradient flow. Rehman et al. [126] presented a method for 3D image registration based on optimal mass transport problem. Meanwhile, they stress the fact that the optimization of OMT is computationally expensive and emphasize that it is important to find efficient numerical methods to solve this issue, and it is crucial to extend the results to 3D surfaces.

There are also some works based on Monge-Brenier theory. Our prior work [120, 144] proposed an area-preserving mapping method for brain morphological study and visualization, but they can only compute the maps from the unit disk domain with Euclidean measure to another disk with general measure. Merigot [97] has proposed a multi-scale approach to solve optimal transport problem. de Goes et al. [35] have provided an optimal-transport driven approach for 2D shape reconstruction and simplification. Recently they have presented a formulation of capacity-constrained Voronoi tessellation as an optimal transport problem for image processing [34]. This method produces high-quality blue noise point sets with improved spectral and spatial properties. In summary, except our prior work [120, 144], other Monge-Brenier theory based methods were all applied to 2D image matching and registration. By contrast, our work is the first one to apply Monge-Brenier based optimal mass transport method to study 3D shape analysis.

Surface Registration

There is a vast literature on surface/image registration, a thorough survey on deformable medical image registration can be found in [115], which gives a rigorous treatment for registration problem. Let S and T be source and target images defined in an image domain Ω, a transformation $W : \Omega \to \Omega$ is a diffeomorphism of the domain. Then [115] formulate the registration as an optimization problem with the energy form $\mathcal{M}(T, S \circ W) + \mathcal{R}(W)$, where $\mathcal{M}$ measures the deformation, $\mathcal{R}$ measures the regularity of the mapping W. The survey covers methods which minimizing different energies $\mathcal{M}$. The elastic body models optimize the elastic deformation energy; the viscous fluid models minimizes the fluid dynamics energy; the diffusion model deforms the harmonic energy (membrane energy); the curvature registration method optimizes the bending energy; the flows of diffeomorphisms finds the geodesic in the shape space. Some other energy terms incorporate the landmark constraints, or the constraints for the mapping, such as the mapping should belong to homeomorphism, volume preserving or rigid motion group.

The survey does not cover methods based on optimal mass transportation or conformal mapping. In contrast, our method is based on optimal transportation and conformal mapping. Given two metric surfaces $(S_1, \mathbf{g}_1)$ and $(S_2, \mathbf{g}_2)$, which are topological disks, first we map them to the planar disk $\mathbb{D}$ by conformal mappings, $\varphi_k : S_k \to \mathbb{D}$, the induced confor-

mal factors are λ_k, $k = 1, 2$. Then on the disk, there are two measures $\mu_k = e^{2\lambda_k(x,y)}dx \wedge dy$. We find an optimal transportation map $\tau : (\mathbb{D}, \mu_1) \to (\mathbb{D}, \mu_2)$, the composition $\varphi_2^{-1} \circ \tau \circ \varphi_1$ gives the registration.

From differential geometry, any mapping between two surfaces will induce area distortion and angle distortion. Unless the two surfaces are isometric, one of the two types of distortions is unavoidable. Our registration goal is to minimize both angle and area distortions. Conformal mapping φ_k has 0 angle distortion; optimal mass transportation map τ has 0 measure distortion. The work of [38] shows that this type of mapping minimizes both angle and area distortion.

In computer vision and medical imaging research, feature landmarks, such as sulci lines on brain surfaces or extreme points on general surfaces, are usually required to guide surface registration [122, 89, 146, 133, 87, 57]. Kurtek et al. [87] proposes a constrained optimization approach that simultaneously computes dense correspondences and geodesics between surfaces. In this work, if there are landmark constraints, after the optimal mass transportation map τ, we add an harmonic map η to enforce the alignment of the landmarks. Although it shares some similar motivation with other landmark constrained surface registration work, our method has a few fundamental distinctions from that of [87]. First, our method is intrinsic while their method considers the embedding; second, our method computes the registration directly while their method finds the deformation path; third, our method can handle non-isotopic surfaces but their method can not.

Shape Space

A popular Riemannian framework for modeling shape space is to measure the similarity between two shapes by the deformation between them. A deformation process is a path in the shape space, the length of path gives the amount of deformation. Among all paths, the one with the minimal length is the geodesic. The length of the geodesic gives the *distance* between the shapes.

Shape space is the space of orbits of the *reparameterization group* acting on the space of immersions [117, 137, 116]. Namely, fix a smooth $n-1$ dimensional manifold M, let Γ be Lie group of all diffeomorophisms of M, which is the reparameterization group [118]. The shape space is the space of all smooth immersions quotient by Γ, denoted as $\mathcal{F}$. Riemannian metrics measure infinitesimal deformations. Given an immersion $f : M \to \mathbb{R}^n$, and two deformation vector fields on f, $h, k : M \to \mathbb{R}^n$, $h, k \in T_f(\mathcal{F})$, one design a reparameterization invariant metric $\langle , \rangle_f$, such that $\langle h, k\rangle_f = \langle h \circ \gamma, k \circ \gamma\rangle_{f\circ\gamma}, \forall\gamma \in \Gamma$, the construction may involve the metric of the ambient space $\mathbb{R}^n$, the metric of the immersion f, the covariant derivatives or differential operators on f and so on.

The reparameterization invariant metric constructed in [20, 19] uses the volume form and the mean curvature of the immersion f, the metric in [86] uses the area multiplication factor of f. [87] extends the work in [86] by adding landmark constraints. Instead of considering the whole reparameterization group Γ, only a subgroup fixing the landmarks is applied. The infinitesimal generators of such subgroup are constructed using an elegant technique based on spherical harmonics. [73] represents the embedding f by its area el-

ement and normal vector (r, n), the so-called square root normal fields (SRNF), and the reparameterization invariant metric is built on SRNF.

Our conformal Wasserstein shape space shares some theoretic properties with other Riemannian shape space frameworks while it also has certain fundamental differences.

- Definition of shape: these methods consider the extrinsic embeddings/immersions; our method only focuses on the intrinsic Riemannian metric.
- Reparameterization: these methods focus on designing reparameterization invariant metrics; our method uses normalized conformal mapping, which is unique, therefore there is no reparameterization ambiguity.
- Definition of distance: these methods use the geodesic length; our method uses the cost of the optimal mass transportation map.
- Deformation: these methods give the deformation sequence of shapes; our method only gives the distance without deformation.
- Isotopy constraint: these methods assume there is a deformation from one shape to the other, which requires two shapes are isotopic; our method is intrinsic, applicable for non-isotopic shapes.

In practice, our method is numerically efficient and can also be generalized to high dimensional data processing.

3D Shape Classification

Various shape classification and comparison methods were proposed in computer vision field. Ankerst et al. [12] introduced shape histogram decomposing shells and sectors around a models centroid. Osada et al. [101] proposed 3D shape representations by probability distributions of geometric properties computed for points randomly sampled on an objects surface. Laga et al. [88] represented 3D shapes by spherical wavelet transforms. Unnikrishnan et al. [128] presented a multi-scale operators on point clouds that captures variation in shapes. Mahmoudi et al. [95] represented shapes by computing the histogram of pairwise diffusion distances between all points. Kurtek et al. [86] provided a Riemannian framework for computing geodesic paths which are important for comparing and matching 3D shapes. Jermyn et al. [73] defined a general elastic metric on the space of parameter domains for shape comparisons and analysis.

Our shape classification method solely depends on Riemannian metrics and is invariant under rigid motions and scalings, yet most conventional geodesic methods depend on embeddings and thus not intrinsic; The statistical methods based on histograms and pairwise diffusion distances only measure the distance between shapes, but our method explicitly gives the diffeomorphic map between shapes as a by-product; The geodesic path methods assume there is a deformation from one shape to the other, which requires two shapes are isotopic, however our method is intrinsic, applicable for non-isotopic shapes.

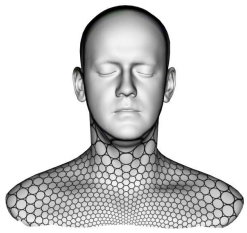

(a) texture mapping by CFP

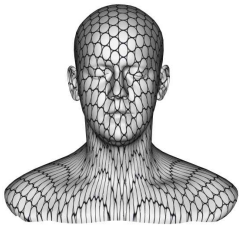

(b) texture mapping by APP

(c) angle-preserving

(d) area-preserving

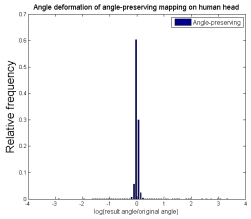

(e) angle distortion by CFP

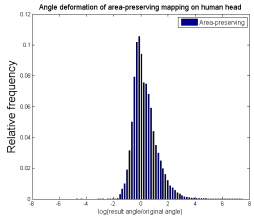

(f) angle distortion by APP

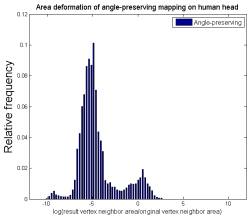

(g) area distortion by CFP

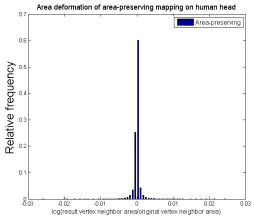

(h) area distortion by APP

Figure 14: Circle-packing texture mappings for conformal parameterization (CFP) (a) and area-preserving parameterization (APP) for the model of a human head, with the planar unit square parameter domain (b). The mappings to the parameter domain results are also shown in (c) and (d), respectively. (e) to (h) are the histograms of angle distortions and area distortions, which demonstrate the accuracy of the Optimal Mass Transport map.

(a) front view

(b) back view

(c) CFP front view

(d) APP front view

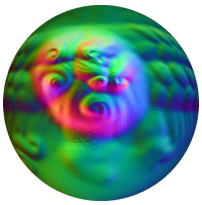

(e) CFP back view

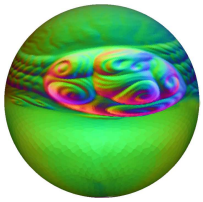

(f) APP back view

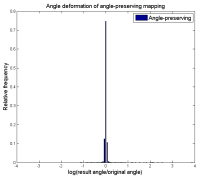

(g) angle distortion by CFP

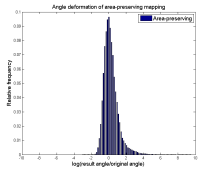

(h) angle distortion by APP

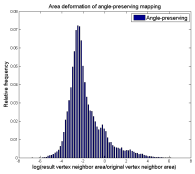

(i) area distortion by CFP

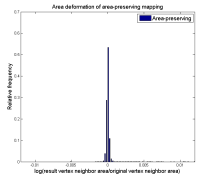

(j) area distortion by APP

Figure 15: Comparison of conformal parameterization (CFP) and area-preserving parameterization (APP) of a Bimba sculpture model, shown in (a) and (b), with the spherical parameter domain. The normal information on the original surfaces is preserved and used for rendering.(g) to (j) are the histograms of angle distortions and area distortions.

4.3 Deformable Surface Matching Application

In this section, we apply Optimal Mass Transport Map for deformable surface matching. The approach is illustrated by the following commutative diagram:

$$\begin{array}{ccc} S_1 & \xrightarrow{f} & S_2 \\ \downarrow{\scriptstyle \phi_1} & & \downarrow{\scriptstyle \phi_2} \\ D_1 & \xrightarrow{g} & D_2 \end{array}$$

where S_1 and S_2 are two given surfaces with deformation and $f : S_1 \to S_2$ is the desired matching. We use Optimal Mass Transport Map to compute $\phi_i : S_i \to D_i$ which maps S_i onto the canonical domain D_i. D_i can be domains on plane R^2 or sphere R^3. We call them optimal mass transport parameter domains of the surfaces. Then a planar or spherical mapping $g : D_1 \to D_2$ is constructed for matching. The desired map is induced by $f = \phi_2^{-1} \circ g \circ \phi_1 : S_1 \to S_2$. The OMP-map is intrinsic to the Riemannian metric, unique, and diffeomorphic and useful to compute ϕ_1, ϕ_2. This framework converts a 3D deformable surface matching problem to a 2D planar domain matching problem, or a 3D spherical matching problem, which are much easier than matching on the original surfaces.

Since our Optimal Mass Transport map converts the 3D surfaces to convex planar domain, if the map g is a diffeomorphism, the matching f is also a diffeomorphism. In our framework, that g is diffeomorphism is guaranteed by the following theorem:

Theorem 4.1 (Rado [109].)**.** *Let (S, g) be a simply connected surface, D be a convex planar domain. f is a harmonic map such that the restriction of f on the boundary $f : \partial S \to \partial D$ is a homeomorphism, then f is a diffeomorphism.*

4.3.1 Surface Matching by Euclidean Optimal Mass Transport Map

Here we use a simply connected surface with one boundary as an example to show how the OMT-Map algorithm can help compute surface matching. However, the algorithm is able to be generalized to topological sphere surfaces.

For such surfaces, the conformal parameter domain D can be chosen as the unit disk. Given two 3D surfaces S_1 and S_2 with deformations between them, $f : S_1 \to S_2$ is the desired matching. Algorithm 7 show the algorithm details.

4.3.2 Experimental Results

Data source To validate the robustness and efficiency of our method, we tested surfaces with large isometric deformations. We chose 7 models that are isometric deformations to each other to study the accuracy and efficiency of our proposed method. The original Armadillo models, the same subject with different motions, are obtained from Aim@SHAPE

Algorithm 7 Deformable surface registration.

Input: Triangular meshes of surfaces with a simple topology, such as a simply connected domain with one boundary. A template surface as the target surface.

Output: Registered surfaces with a one-to-one correspondence from each surface to the target surface.

1. Manually or automatically locate some corresponding feature points on S_1 and S_2 for constraints.

2. Compute a constrained harmonic map $g : D_1 \to D_2$, such that g align the corresponding feature points specified in the first step.

3. The matching is given by $f = \phi_2^{-1} \circ g \circ \phi_1 : S_1 \to S_2$.

repository [2] (shown in Figure 16). They form 21 different pairs of surfaces being matched to each other.

Figure 17 shows an example surface matching result for Armadillo models with different motions. (a) and (b) are the two models with isometric deformations. We cut a hole at the waist of the models so that they are topologically equivalent to a disk. (c) and (f) are the optimal mass transport map results. Their mapping results are matched using harmonic maps with hard constraints (yellow stars). The colored lines connecting color-encoded circular dots on (a) and (b) show the registered correspondences by OMT map.

Performance Evaluation and Comparison. We compared our matching and registration method with conventional conformal mapping method based on Ricci flow theory [133], where the source surface is conformally flattened to a planar disk, then the registration is obtained by a constrained harmonic map between the disk and the target surface. We also compared our work with the Lipman and Funkhouser's Möbius voting method [89]. The method first randomly samples a triplet on each of two surfaces, and uses Möbius transformations defined by the triplets to map the original surfaces into a complex domain, and finally produces voting points to predict correspondences between the surfaces. We used some performance metrics which were used in prior surface registration studies [102].

Diffeomorphism. One of the most important advantages of our registration method is that, in practice it always generates the mapping between surfaces to be diffeomorphic, even for long tube surfaces that may have numerical problems by conformal mapping, such as the fingers of the Armadillo model show in Figure 13. For each registration, we compute the Jacobian determinant and measure the area of flipped regions. For conformal mapping method, the average ratio from flipped area to the total area of 21 Armadillo pairs is 25.8%. The average flipped area ratio for the Möbius voting method is 4.5%. In contrast, the flipped area ratios for all registrations obtained by our method are exactly zero.

Curvature Difference Maps. Our method to evaluate registration accuracy is to compare

Figure 16: 7 Armadillo models with isometric deformations, which form 21 matching pairs in our experiments.

the alignment of curvature maps between the registered models [102]. We calculated curvature maps using an approximation of mean curvature, which is the convexity measure. We quantified the effects of registration on curvature by computing the difference of curvature maps from the registered surfaces. For each vertex on the target surface with curvature c_1, we find its correspondent point on the source surface with curvature c_2. Then compute the curvature difference as $max(\frac{|c_1|}{|c_2|}, \frac{|c_2|}{|c_1|})$. In Figures 17 (e) shows the average histogram of the curvature difference map of conformal mapping, Möbius voting method and our method computed from all 21 pairs of surface matchings, respectively. The quantitative results indicate that conformal mapping and the Möbius voting method produce less consistent and less accurate correspondences than our method.

Local Area Distortion. Similarly, we evaluated the local area distortion induced by the registrations [102]. For each vertex v on the target surface with its correspondent point p on the source surface, we compute its Jacobian determinant $J(v)$ [133], and represent the local area distortion at v as $max(J(v), J^{-1}(v))$. J can be approximated by the ratio between the measure $\mu(v)/\mu(p)$, where $\mu(v_i) := \frac{1}{3}\sum_{jk} Area([v_i, v_j, v_k])$ and $[v_i, v_j, v_k]$ is a triangle face adjacent to v_i. Note that if the registration is not diffeomorphic, the local area distortion may go to ∞. Therefore, we add a threshold to truncate large distortions. Figures 17 (h) shows the average area distortion histogram of conformal method, Möbius voting method and our method. It is obvious that our registration method produces much less area distortions than the other two methods.From these quantitative empirical evaluations, we observe that our method may outperform previous methods [89, 133] by registration accuracy. Moreover, our method has the advantages that it can handle large area distortion, and guarantees diffeomorphic mappings.

Figure 18 shows another example of registration.

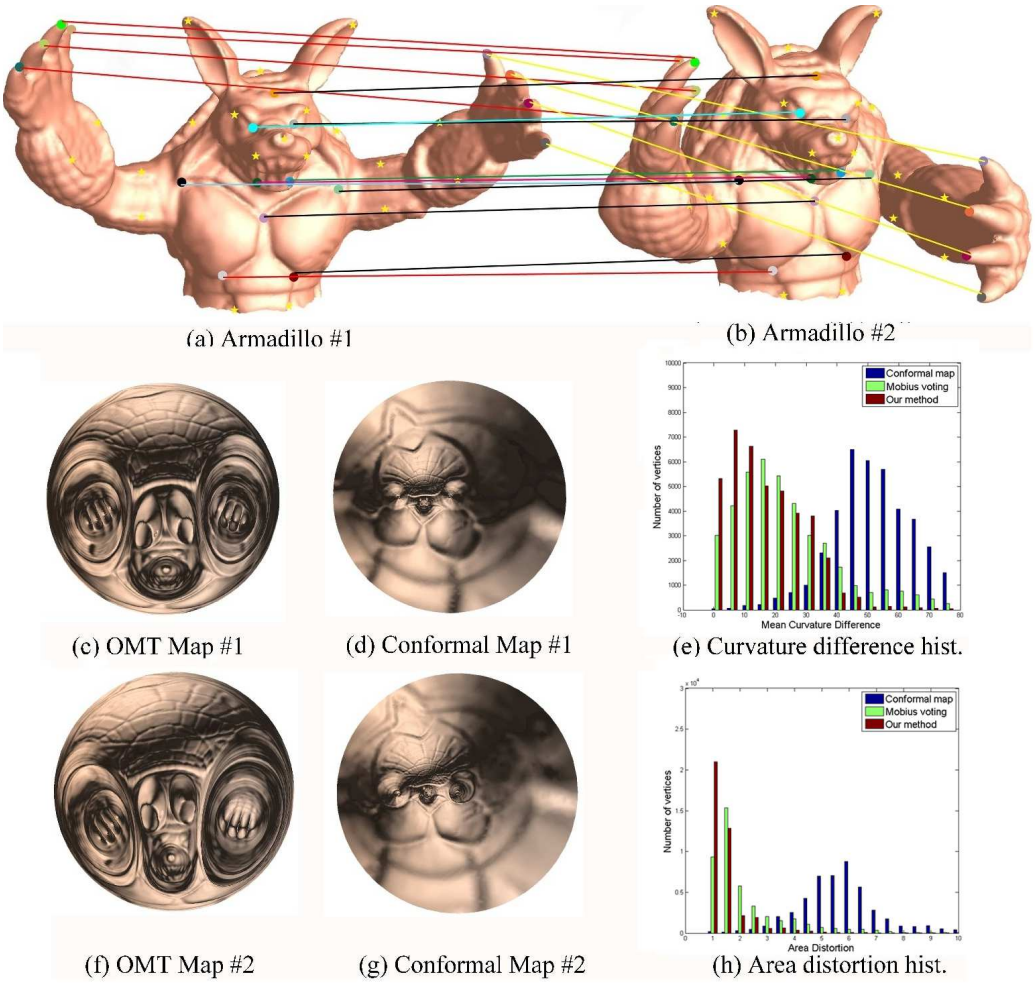

Figure 17: Surface registration results for Armadillo models with isometric deformations. (a) and (b) are the two models respectively, (c) and (f) are the optimal mass transport map results respectively, and (d) and (g) are the conformal map results respectively. Their mapping results are registered using harmonic maps with hard constraints (yellow stars). The colored lines connecting color-encoded circular dots on (a) and (b) show the registered correspondences by OMT map. (e) shows the average histogram of the curvature difference map of conformal mapping, Möbius voting and our method, for 21 Armadillo pairs; (h) shows the average area distortion histogram of conformal method, Möbius voting and our method, for 21 Armadillo pairs. It can be easily seen that our current registration method greatly reduces the curvature errors and local area distortions.

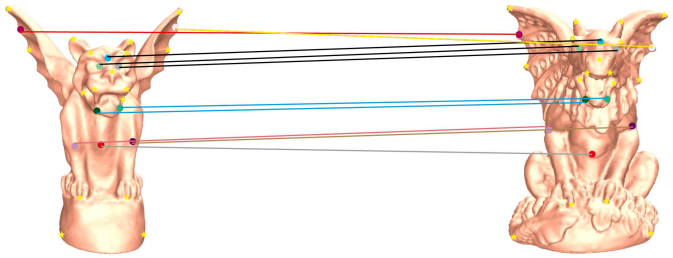

(a) Gargoyle #1 (b) Gargoyle #2

(c) OMT map #1

(d) OMT map #2

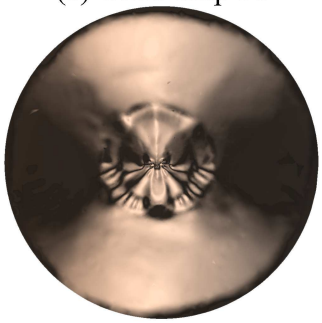

(e) Conformal map #1

(f) Conformal map #2

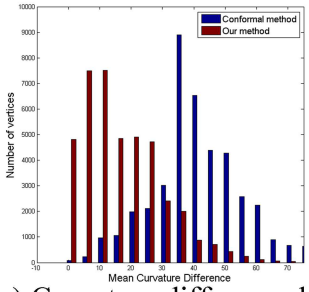

(g) Curvature difference hist.

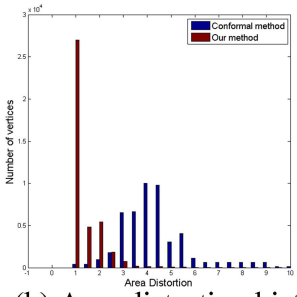

(h) Area distortion hist.

Figure 18: Surface registration results for Gargoyle models.

Figure	# of Faces (a)	# of Faces (b)	Running Time(s)
19	84.7K	83.1K	180.2
20	84.7K	79.4K	220.4
24	77.4K	79.2K	107.9

Table 1: Running time of the Riemannian OMT Map between surfaces.

4.4 Shape Classification Application

In this section, we showed the experimental results and proved the efficiency and efficacy of our method. We implemented our algorithms using C++ in Windows platform. All the 3D shape surfaces in this paper are represented by triangle meshes.

Running time summary Table 1 summarizes the running time of the Riemannian optimal mass transport (OMT) map between 3D surfaces. The results show that the time mainly depends on the complexities of the models and the similarities between shapes.

4.4.1 Wasserstein Distance

In this section, we illustrated the results of Wasserstein distance by Alg. 5 between general 3D shapes. The models are obtained from Aim@SHAPE repository [2]. Figure 19 shows the computation of Wasserstein distance between a pair of similar 3D shapes. (a) and (b) are the original surfaces of two Gargoyle models respectively. The two models have very similar structures yet distinguish with some local deformations; (c) and (d) are the spherical conformal mapping results of the two Gargoyle models respectively. The colors are encoded by the normal information on the original surfaces. (e) shows the Riemannian optimal mass transport map result from (c) to (d), which induces the Wasserstein distance between (a) and (b). In Figure 20, a pair of dissimilar 3D shapes, i.e. a Gargoyle model and a Buddha model, are used for computing the Wasserstein distance.

The Wasserstein distance between Figure 19 (a) and (b) is 0.42, yet the Wasserstein distance between Figure 20 (a) and (b) is 1.25. The results showed that the Wasserstein distance between similar shapes is significantly smaller than dissimilar pairs, which demonstrated the potential for using Wasserstein distance to classify 3D shapes.

4.4.2 3D Facial Expression Classification

Wasserstein distance is a Riemannian metric of the Wasserstein space. The Wasserstein distance between two surfaces is a shape metric which can be used for quantifying shape differences. The computational algorithm can be found in Alg. 5. Figure 21 shows the

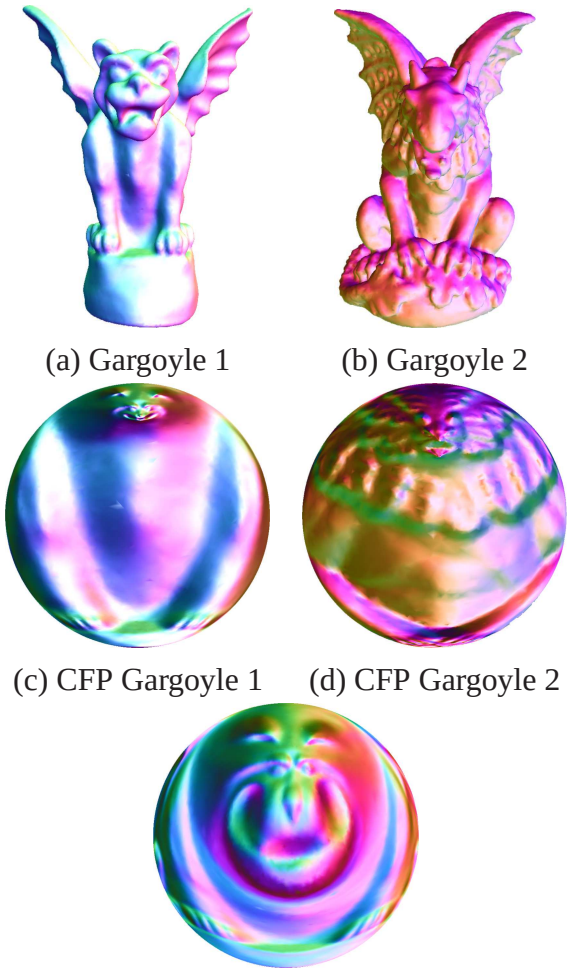

(a) Gargoyle 1 (b) Gargoyle 2

(c) CFP Gargoyle 1 (d) CFP Gargoyle 2

(e) Riemannian OMT Map

Figure 19: The computation of Wasserstein distance between a pair of similar 3D shapes. (a) and (b) are the original surface of two Gargoyle models. (c) and (d) are the spherical conformal parameterization (CFP) of (a) and (b), respectively. The colors are encoded by the normal information on the original surfaces. (e) shows the Riemannian optimal mass transport (OMT) map result from (c) to (d), which induces the Wasserstein distance between (a) and (b).

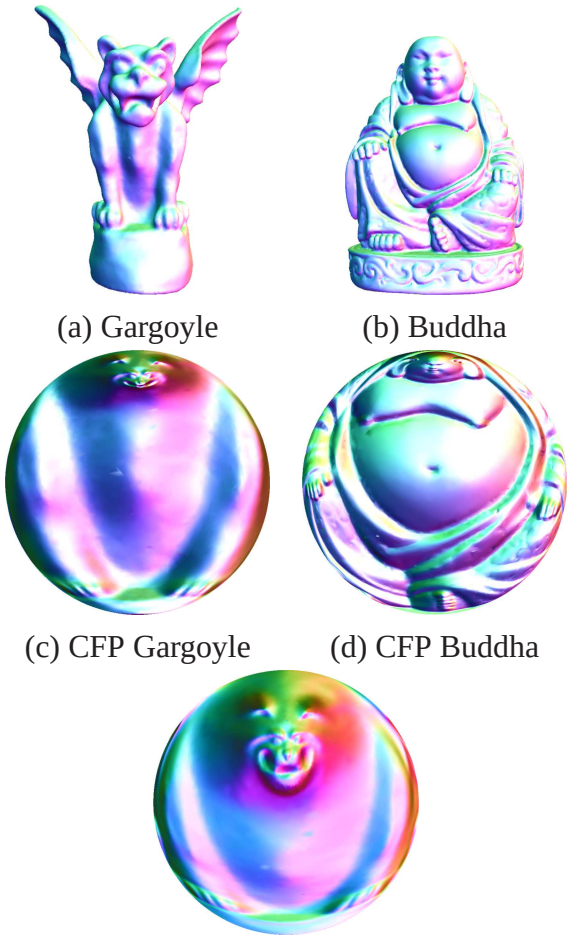

(a) Gargoyle (b) Buddha

(c) CFP Gargoyle (d) CFP Buddha

(e) Riemannian OMT Map

Figure 20: The computation of Wasserstein distance between a pair of dissimilar 3D shapes, i.e. a Gargoyle model and a Buddha model. (c) and (d) are the spherical conformal parameterization (CFP) of (a) and (b), respectively. The colors are encoded by the normal information on the original surfaces. (e) shows the Riemannian optimal mass transport (OMT) map result from (c) to (d), which induces the Wasserstein distance between (a) and (b).

visualization results of Wasserstein distance. (a) and (c) are two face surfaces of different facial expressions. (b) and (d) are the conformal mapping results for (a) and (c), respectively. (e) shows the optimal mapping from (a) to (c), which induces Wasserstein distance by Eqn. 3.31. For better visualization of (e), we put straight grids on (c), and draw the deformed grids on (e). From the grids deformation, we can clearly see how the surface around the mouth and nose deforms when the facial expression changes from calm to smile.

As noted earlier that Wasserstein distance can be used for quantifying shape differences, we applied Wasserstein distance for facial expressions clustering. Our experimental dataset contains 10 people, each of which has 3 different facial expressions–"sad", "happy" and "surprise" shown in Figure 22 row 1, 2, 3, respectively. The 3D face surfaces are from Binghamton University 3D Facial Expression Database [135]. For each pair of surfaces in the dataset, we compute the Wasserstein distance. Then we use classical multidimensional scaling (MDS) [124] to embed all the 30 face surfaces in $\mathbb{R}^2$ based on the Wasserstein distance between each pair of faces. Figure 23 illustrates the visualization results of the MDS embedding. For all the surfaces with "sad" expressions, we mark them as '+' in blue color, and "happy" as 'x' in red color, and "surprise" as 'o' in green color. We can see that almost all faces with the same expressions are clustered together, and faces with different expressions are divided into different clusters.

The facial expression clusters verify the idea that physical expressions of emotions can be systematically categorized and support the adoption facial action coding system (FACS) [40] in computer vision and animation research. The experimental results also demonstrated the feasibility and potential of comparing and quantifying shape differences by conformal Wasserstein distance. Whether or not Wasserstein distance provides better accuracy in facial expression clustering than those afforded by other shape distance requires careful validation for each application. More importantly, we anticipate that our approach may serve as novel shape distance for shape analysis. In future we plan to exploit the potential of proposed shape distance for more applications such as face recognition.

4.4.3 Brain Classification by IQ

There have been much research into the relation between human intelligence and human brain. Earlier works have studied some significant factors such as cortical surface area, cortical thickness and cortical convolution [71, 92, 91]. To validate the correctness of our framework in real applications, we applied our method for the classification problem of brain cortical surfaces with different intelligence quotient (IQ), and compared with some existing works.

Data preparation: The dataset used in our experiments is real brain data from a medical center (due to the anonymity rule for review, we do not disclose the name of the organization for the moment), it includes 50 male and 50 female, with ages ranging from 18 to 30 years. The brain cortical surfaces are reconstructed from MRI images by FreeSurfer [4]. Among all the brain data, we used the left hemisphere of the brain surface

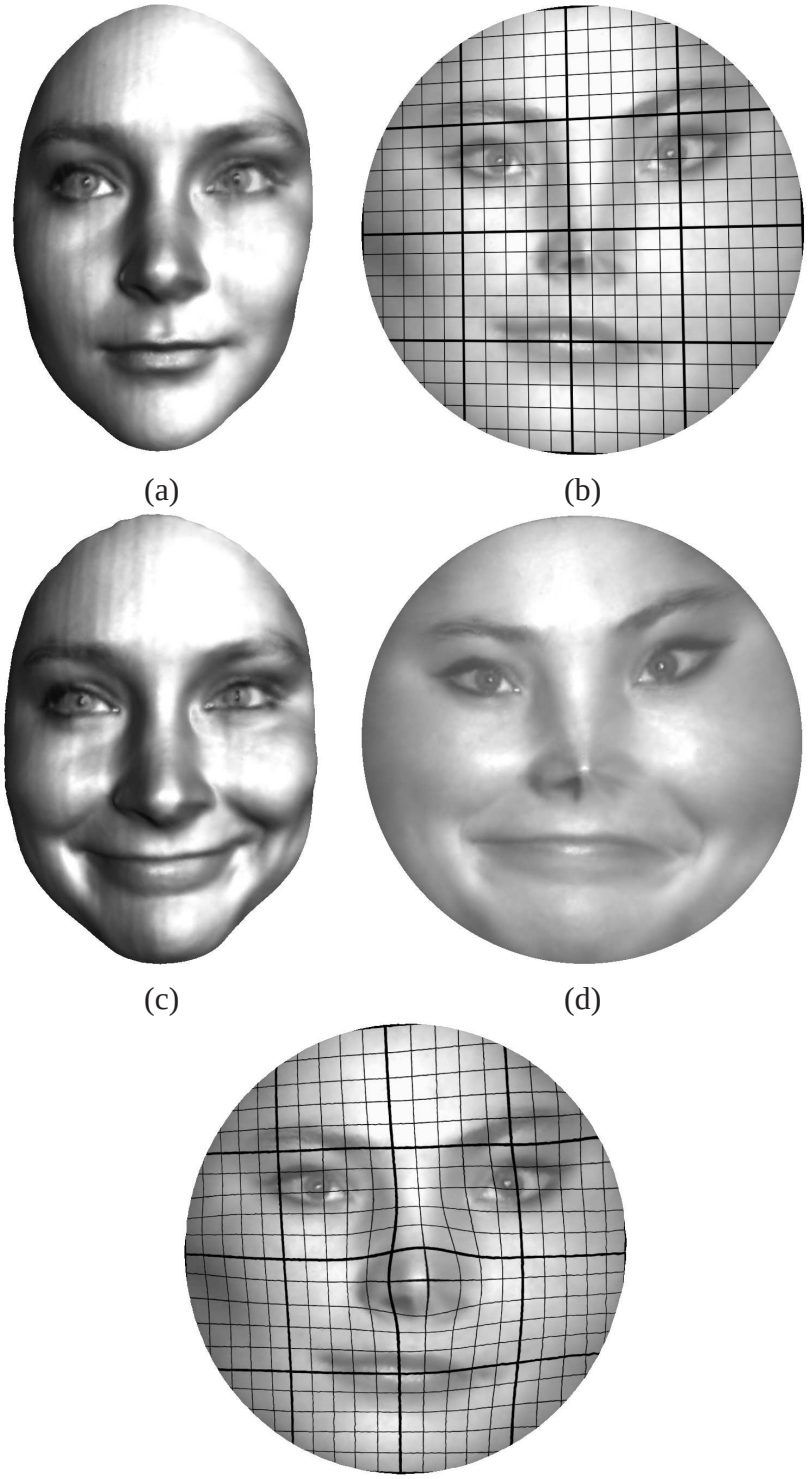

Figure 21: The computation of Wasserstein distance

Figure 22: Face surfaces for expression clustering. The first row is “sad”, the second row is “happy” and the third row is “surprise”.

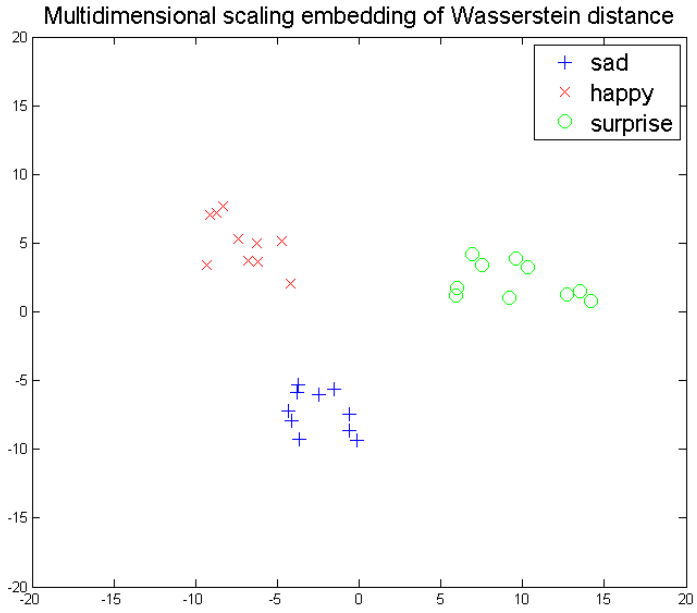

Figure 23: Multidimensional scaling embedding of the Wasserstein distance between each pair of face surfaces in the dataset.

for experiments.

The intelligence quotient (IQ) was evaluated by an online version of Ravens Advanced Progressive Matrices (APM) [5]. The test consists of 36 questions and the IQ score is calculated by $N_{correctAnswers}/N_{total} * 100$. The IQ among the data ranges from 0 to 100, which are almost uniformly distributed. Figure 24 shows the computation of Wasserstein distance between two brain cortical surfaces. (a) shows an example of a 20-year-old female, with IQ score 88.89; (b) shows an example of a 21-year-old male, with IQ score 33.33.

Instead of claiming whether one human brain is intelligent or not, in our experimental settings we divided the IQ into three classes: A, B, and C, ranging from $A : [0, 33)$, $B : [33, 67)$ and $C : [67, 100]$. The data uniformly distributed in the three classes. For each gender, we randomly chose 12 examples from each class. Therefore, we created a training set of 72 examples, which is uniformly distributed with respect to gender and IQ. And the remaining examples are used as testing data.

For the classification experiments, we first computed the full pair-wise Wasserstein distance matrix based on our method. We indexed all the data of class A into $i = 1, 2, ..., 33$, data of class B into $i = 34, 35, ..., 66$ and data of class C into $i = 67, 68, ...100$. Figure 25 shows the visualization of the Wasserstein distance matrix encoded in a gray image. The distance is normalized from 0 to 1, where 0 indicates black and 1 indicates white. The entry of the matrix $M_{i,j}$ is the Wasserstein distance between brain data i and brain data j. Then we can clearly see that, mostly, two surfaces in the same class induce smaller Wasserstein distance, yet two surfaces in different classes induce larger Wasserstein distance. The results further demonstrated the power of Wasserstein distance for measuring shape similarities.

With the distance matrix, we classified the testing set by k-Nearest Neighbors (k-NN) classifier, where k is chosen to be 11 by running 9-fold cross-validation (we chose 9-fold to make each fold has the same number of examples.). The cross-validation curve is shown in Figure 26. Table 3 shows the classification rate of our method is 78.57%.

To demonstrate the efficiency and advantages of our method, we compared our method with existing popular method. Previous work [76] shows that cortical surface area and cortical surface mean curvature have significant correlations to human intelligence, since they quantify the complexity of cortical foldings. Thus we computed the two cortical measurements and used surface area, mean curvature, and the combination of the two measurements as three types of features for classification, respectively. We used LIBSVM [3] as the classifier. Linear kernel and regularization parameter $C = 4.5$ were chosen by cross validation. Table 3 reports the classification rate of all the three comparison methods. The results indicated that our method outperforms previous methods.

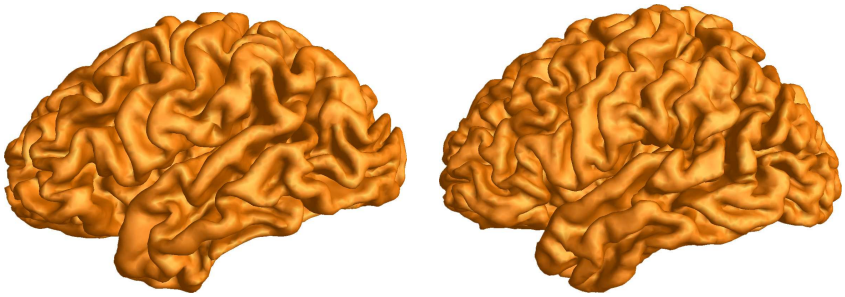

(a) Brain 1 (b) Brain 2

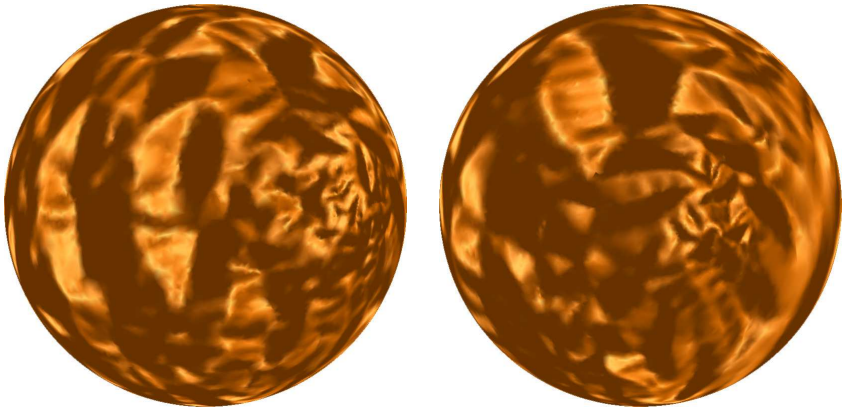

(c) CFP Brain 1 (d) CFP Brain 2

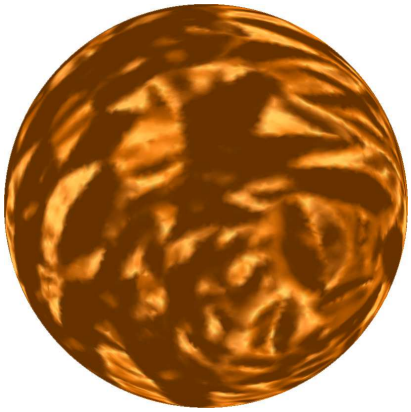

(e) Riemannian OMT Map

Figure 24: The computation of Wasserstein distance between the left hemisphere brain cortical surfaces. (a) shows an example of a 20-year-old female, with IQ score 88.89; (b) shows an example of a 21-year-old male, with IQ score 33.33. (c) and (d) are the spherical conformal parameterization (CFP) of (a) and (b), respectively. (e) shows the Riemannian optimal mass transport (OMT) map result from (c) to (d), which induces the Wasserstein distance between (a) and (b).

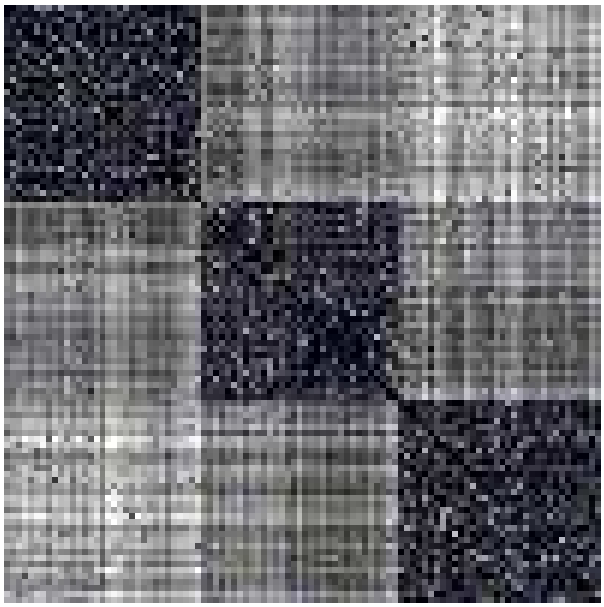

Figure 25: Wasserstein distance matrix encoded in a gray image. The distance is normalized from 0 to 1, where 0 indicates black and 1 indicates white. The results show that, mostly, two surfaces in the same class induce smaller Wasserstein distance, yet two surfaces in different classes induce larger Wasserstein distance

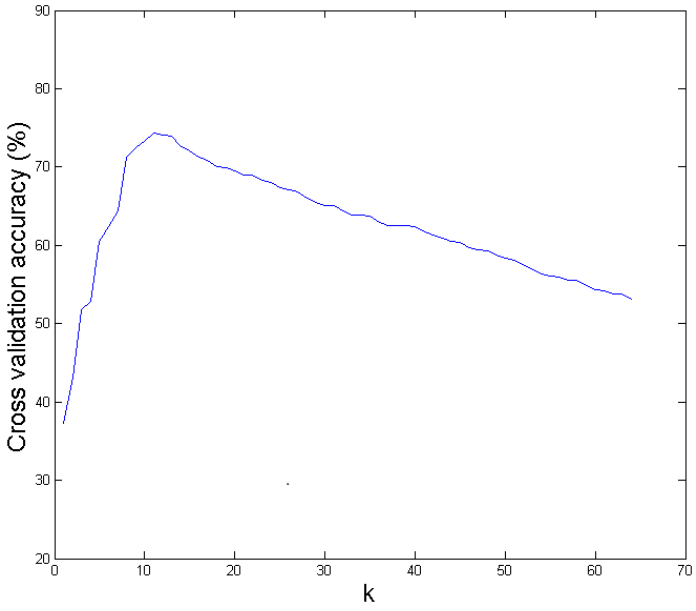

Figure 26: Cross-validation curve. It shows the cross validation accuracy as functions of the parameter k in the k-NN classification. According to the experiments, we chose $k = 11$.

Method	CR
Our method	78.57%
Surface Area	53.57%
Surface Mean Curvature	57.14%
Combination of Area and Curvature	67.85%

Table 2: Classification rate (CR) of our method and previous methods based on cortical surface area, cortical surface mean curvature and combination of previous two cortical measurements. The results demonstrated the accuracy of our method.

5 Area Preserving Brain Mapping

Brain mapping transforms the brain cortical surface to canonical planar domains, which plays a fundamental role in morphological study. Most existing brain mapping methods are based on angle preserving maps, which may introduce large area distortions. This work proposes an area preserving brain mapping method based on Monge-Brenier theory. The brain mapping is intrinsic to the Riemannian metric, unique, and diffeomorphic. The computation is equivalent to convex energy minimization and power Voronoi diagram construction. Comparing to the existing approaches based on Monge-Kantorovich theory, the proposed one greatly reduces the complexity (from n^2 unknowns to n), and improves the simplicity and efficiency.

Experimental results on caudate nucleus surface mapping and cortical surface mapping demonstrate the efficacy and efficiency of the proposed method. Conventional methods for caudate nucleus surface mapping may suffer from numerical instability; in contrast, current method produces diffeomorphic mappings stably. In the study of cortical surface classification for recognition of Alzheimer's Disease, the proposed method outperforms some other morphometry features.

5.1 Overview

Nowadays surface parameterization has been used for a wide variety of applications like pattern recognition and medical imaging. Many prominent approaches, such as conformal mapping [53] and Ricci Flow [63] which have been employed to shape analysis [111, 25] and surface registration [140]. However, an accurate isometric parameterization is impossible for general surfaces.

The conformal mapping may bring huge area distortions in certain surfaces, e.g. a slim surface of brain caudate nucleus. In turn, such distortions usually introduce much difficulty

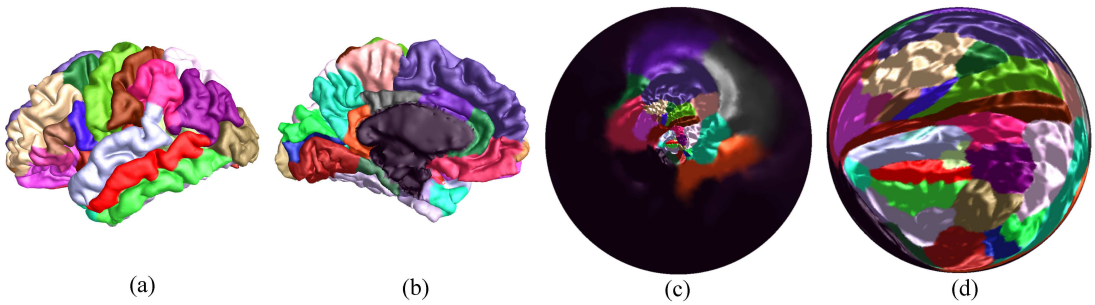

Figure 27: Comparison of geometric mappings for a left brain cortical surface: (a) brain cortical surface lateral view; (b) brain cortical surface medial view; brains are color coded according to functional area definition in [37]; (c) conformal mapping result; (d) area preserving mapping result. The results show that conformal mapping has much more area distortions on the areas close to the boundary while the area preserving mapping provides a map which preserves the area everywhere.

for following shape analysis. As the clinical questions of interest move towards identifying very early signs of diseases, the corresponding statistical differences at the group level invariably become weaker and increasingly harder to identify. A stable method to compute some other mapping with alternative invariants may be highly advantageous for visualization and shape analysis in this research area.

In this work, we propose a novel method to compute area preserving mapping between surfaces. The mapping is diffeomorphic and unique under normalization. Moreover, the mapping is invariant under isometric transformations. We tested our algorithm on cortical and caudate nucleus surfaces extracted from 3D anatomical brain magnetic resonance imaging (MRI) scans. Figure 27 demonstrates the unique power that the area preserving mapping provides for brain cortical surface visualization when compared with its counterpart conformal mapping result. On cortical surfaces, the area preserving may also provide good visualization function to visualize those deeply buried sulci areas which otherwise are usually visualized with big area distortions. In a classification study, our algorithm achieved $87.50\% \pm 0.55\%$ average recognition rate with 95% confidence interval in a brain image dataset consisting of images of 50 healthy control (CTL) subjects and 50 Alzheimer's Disease (AD) patients. We also show that this novel and simple method can outperform two other morphometry features in the same dataset.

5.1.1 Comparison

The area preserving mapping is based on *Optimal Mass Transport* (OMT) theory, which has been applied for image registration and warping [60, 105] and visualization [147]. Our method has fundamental differences from these existing methods.

Monge considered the transportation cost for moving a pile of dirt from one spot to the other, then formulated the *Optimal Mass Transport* problem. Let $\Omega_k \subset \mathbb{R}^n$ be subdomains in $\mathbb{R}^n$, with positive density functions μ_k, such that

$$\int_{\Omega_0} \mu_0 dx = \int_{\Omega_1} \mu_1 dx.$$

Consider a diffeomorphism $f : \Omega_0 \to \Omega_1$, which is *mass preservation*

$$\mu_0 = |J_f| \mu_1 \circ f$$

where J_f is the Jacobian of the mapping f. The *mass transport cost* is

$$C(f) := \int_{\Omega_0} |x - f(x)|^2 \mu_0(x) dx.$$

An *optimal mass transport map*, when it exists, minimizes the mass transport cost. There are two different approaches to prove the existence of the optimal mass transport map, i.e. Kantorovich's and Brenier's. Existing methods follow Kantorovich's approach [78], our proposed method follows Brenier's [27].

Kantorovich constructed a measure $\mu(x, y) : \Omega_0 \times \Omega_1 \to \mathbb{R}$, which minimizes the cost

$$\int_{\Omega_0 \times \Omega_1} |x - y|^2 \mu(x, y) dx dy, \tag{5.1}$$

with the constraints

$$\int_{\Omega_1} \mu(x, y) dy = \mu_0(x), \int_{\Omega_0} \mu(x, y) dx = \mu_1(y). \tag{5.2}$$

In contrast, Brenier showed there exists a convex function $u : \Omega_0 \to \mathbb{R}$, such that its gradient map ∇u gives the optimal mass transport map, and preserves the mass:

$$\mu_0 = det|H(u)| \mu_1 \circ \nabla u.$$

Conventional methods discretize each Ω_k to n samples with discrete measures, and model the measure μ to an $n \times n$ matrix with linear constraints Eqn.5.2, such as a doubly-stochastic matrix (sum of each row and the sum of each column equal to one). The optimization of energy Eqn.5.1 is converted to a linear programming problem with n^2 variables.

In our current method, we only discretize the target domain Ω_1 to n points, then determine n power weights for them, so that the power Voronoi diagram induced by the points and their power weights gives the optimal mass transport map. Furthermore, the n power weights can be obtained by optimizing a convex energy.

Comparing to Kantorovich's approach, Brenier's approach has the following merits from computational point of view:

1. Complexity: Existing method has n^2 unknowns, whereas ours has only n variables.

2. Uniqueness: Due to the convexity of the energy, our method has a unique solution.

3. Diffeomorphism: If the domains are convex, The optimal mapping is guaranteed to be diffeomorphic.

4. Efficiency: Due to the convexity of the energy, it can be optimized using Newton's method.

5. Simplicity: The computational algorithm is mainly based on (power) Voronoi diagram and Delaunay triangulation.

Furthermore, the obtained area preserving mapping between two surfaces is solely determined by the surface Riemannian metric, therefore it is *intrinsic*.

5.1.2 Contributions

Our major contributions in this work include: a way to compute area preserving mapping between surfaces based on Brenier's approach in Optimal Mass Transport theory. The current approach produces the unique diffeomorphic mapping. Comparing to the exiting method, the new method greatly reduces the complexity (from n^2 to n) and improves the simplicity and efficiency.

Thus our method offers a stable way to calculate area preserving mapping in $2D$ parametric coordinates. To the best of our knowledge, it is the first work to compute area preserving mapping between surfaces based on Brenier's approach in OMT and apply it to map the profile of differences in surface morphology between healthy control subjects and AD patients. Our experimental results show our work may provide novel ways for shape analysis and improve the statistical detection power for detecting abnormalities in brain surface morphology.

5.1.3 Related Works

Conformal mapping and quasi-isometric embedding has been applied in computer vision for modeling the 2D shape space or 3D shape analysis [111, 29, 25]. Quasi-isometric brain parameterization has been investigated in [42, 18, 39, 123]. Conformal brain mapping methods have been well developed in the field, such as circle packing based method in [70], finite element method [11, 75, 125], spherical harmonic map method [52], holomorphic differential method [131] and Ricci flow method [133].

Area preserving mapping has been applied for visualizing branched vessels and intestinal tracts in [147], which combined Kantorovich's approach with conformal mapping. Optimal mass transport mapping based on Kantorovich's approach has been applied for image registration in [60]. An improved multi-grid version of OMT mapping is presented

in [105]. Comparing to the existing method, our method is based on Monge-Brenier theory to compute the Optimal Transport mapping and achieves the area preserving.

5.2 Theoretic Background

Optimal Transport Problem Suppose Ω is a domain in $\mathbb{R}^n$ and μ a Borel measure with $\mu(\mathbb{R}^n)$ being the total volume of Ω. Consider transport maps $T : (\Omega, dx) \to (\mathbb{R}^n, \mu)$ which are measure preserving, $T^*\mu = dx$. The cost for the mapping is defined as

$$C(T) := \int_\Omega |x - T(x)|^2 dx.$$

In Brenier's seminal work [27], he proved the following fundamental theorem,

Theorem 5.1 (Brenier)**.** *Let Ω be an n-dimensional compact convex set in $\mathbb{R}^n$ and μ any Borel measure on $\mathbb{R}^n$, so that $\mu(\mathbb{R}^n)$ is the volume of Ω. Then there exists a convex function u on Ω, unique up to adding a constant, so that the gradient map*

$$\nabla u : (\Omega, dx) \to (\mathbb{R}^n, \mu) \tag{5.3}$$

is measure preserving and ∇u minimizes the quadratic cost $\int_\Omega |x - T(x)|^2 dx$ among all transport maps T.

In the following, we call the convex function u the *Brenier potential*, and the gradient map ∇u the *Brenier map*.

In the discrete setting for optimal transport problem, we take the measure μ with finite support, i.e. $\mu = \sum_{i=1}^k w_i \delta_{p_i}$, where $w_i > 0$ and δ_p is the Dirac measure. Then the discrete Brenier theorem is as follows:

Corollary 5.1. *Let Ω be an n-dimensional compact convex set in $\mathbb{R}^n$, point set $P = \{p_1, p_2, \cdots, p_k\} \subset \mathbb{R}^n$, with weights $w_1, w_2, \cdots, w_k > 0$, so that $\sum_{i=1}^k w_i = vol(\Omega)$. Then there exists a piecewise linear convex function $u : \Omega \to \mathbb{R}$, so that Ω is decomposed to k convex sets $W_1, W_2, \cdots, W_k$ with the property that*

1. *$u|_{W_i}$ is linear with $\nabla u|_{W_i} = p_i$,*
2. *$Area(W_i) = w_i$ for all i.*

so that ∇u is the solution to optimal transport problem for Ω and $\{(p_1, w_1), \cdots, (p_k, w_k)\}$ with quadratic cost. The convex function u is unique up to a constant.

Variational Principle for Finite Brenier Map We have found a finite dimensional variational principle for constructing the finite Brenier map.

Fix a finite point set $P = \{p_1, p_2, \cdots, p_k\}$, the powers are $\mathbf{h} = (h_1, h_2, \cdots, h_k)$, the power diagram of $\{(p_i, h_i)\}$ in $\mathbb{R}^n$ partitions Ω to cells $\{W_1, W_2, \cdots, W_k\}$, the areas are

$\mathbf{w} = (w_1, w_2, \cdots, w_k)$. Then the power diagram function $u(x)$ is the Brenier potential, the gradient map is the Brenier map $\nabla u : W_i \to p_i$, which minimizes the quadratic distance cost $C(T) = \int_\Omega |x - T(x)|^2 dx$ for all the maps with the measure preserving property

$$Vol(T^{-1}(p_i)) = Vol(W_i) = w_i, i = 1, 2, \cdots, k.$$

Furthermore, we treat the areas $\mathbf{w}$ as the function of the powers $\mathbf{h}$, then the mapping $\mathbf{h} \to \mathbf{w}$ is a diffeomorphism. Let $W := \{\mathbf{w} | \sum_i w_i = vol(\Omega), w_i > 0\}$ be the space of all possible area vectors, and $H := \{\mathbf{h} | \sum_i h_i = 0, \forall w_i > 0\}$ be the space of all possible power vectors, then

Theorem 5.2 (Main Theorem)**.** *Let Ω be a convex domain in $\mathbb{R}^n$. Fix the point set P, given a power vector $\mathbf{h} \in H$, let $\mathbf{w}$ be the area vector associated to the convex cell decomposition of Ω induced by the power diagram for $\{(p_i, h_i)\}$, then the mapping $\mathbf{w} = \phi(\mathbf{h}) : H \to W$ is a diffeomorphism.*

Proof. We prove the theorem for dimension 2, which can be generalized to arbitrary dimension straightforwardly.

Let the power diagram for $\mathbf{h}$ be $D_\mathbf{h}$, the dual Power Delaunay triangulation be $T_\mathbf{h}$. Any edge $\bar{e} \in D_\mathbf{h}$ has a unique dual edge $e \in T_\mathbf{h}$. Suppose two Voronoi cells W_i and W_j shares an edge $\bar{e}_{ij}$, the direct computation shows

$$\frac{\partial w_i}{\partial h_j} = \frac{\partial w_j}{\partial h_i} = \frac{|\bar{e}_{ij}|}{|e_{ij}|} > 0. \tag{5.4}$$

and

$$\frac{\partial w_i}{\partial h_i} = -\sum_{j \neq i} \frac{\partial w_i}{\partial h_j}. \tag{5.5}$$

We construct a differential 1-form

$$\omega = \sum_{i=1}^{k} w_i dh_i,$$

From Eqn.5.4, ω is closed, $d\omega = 0$. From Brunn-Minkowski theorem [10], we know H is a convex domain. Therefore, ω is an exact form. We then define an energy function

$$E(\mathbf{h}) := \int^{(h_1, h_2, \cdots, h_k)} \sum_{i=1}^{k} w_i h_i. \tag{5.6}$$

The Hessian matrix of E is given by

$$\frac{\partial^2 E}{\partial h_i \partial h_j} = \frac{\partial w_j}{\partial h_i}, \tag{5.7}$$

From Eqn.5.4 and Eqn.5.5, we know the negative of the Hessian is diagonal dominant, so the Hessian is negative definite, the energy E is concave. From the convexity of H and the concavity of E, we conclude the gradient mapping

$$\mathbf{h} \to \nabla E(\mathbf{h}) = \mathbf{w}$$

is a diffeomorphism. □

In practice, the target area vector is given by $\bar{\mathbf{w}} = (\bar{w}_1, \bar{w}_2, \cdots, \bar{w}_k)$, then Brenier map T can be computed as follows. Construct the energy

$$\bar{E}(\mathbf{h}) = \sum_{i=1}^{k} \bar{w}_i h_i - \int^{(h_1,h_2,\cdots,h_k)} \sum_{j=1}^{k} w_j dh_j, \tag{5.8}$$

which is convex and can be minimized using Newton's method. From the minimizer $\mathbf{h}$, we construct the power Voronoi diagram $D_{\mathbf{h}}$, which partitions Ω to convex polygonal cells $\{W_1, W_2, \cdots, W_k\}$, and the power Voronoi diagram function $u(x)$. Then $u(x)$ is the Brenier potential, and $T = \nabla u(x)$ is the Brenier map, $T(W_i) = p_i$.

Area Preserving Mapping for Surfaces Given a simply connected surface $(S, \mathbf{g})$ with total area π, fix an interior point p_0 and a boundary point p_1, then according to Riemann mapping theorem, there is a unique conformal mapping $\phi : S \to \mathbb{D}$, where $\mathbb{D}$ is on the complex plane, such that $\phi(p_0) = 0$ and $\phi(p_1) = 1$. Then the Riemannian metric $\mathbf{g}$ can be represented by $\mathbf{g} = e^{2\lambda} dz d\bar{z}$, where $z = x + iy$ is the complex parameter. The conformal factor defines a measure on the complex disk $\mu = e^{2\lambda(z)} dxdy$. Moreover there exists a unique Briener mapping $\tau : (\mathbb{D}, dxdy) \to (\mathbb{D}, \mu)$. Then the composition mapping $\tau^{-1} \circ \phi : (S, \mathbf{g}) \to (\mathbb{D}, dzd\bar{z})$ is area preserving.

The Brenier map τ conveys the intrinsic information about the Riemannian metric on the surface, which can be formulated as follows:

Theorem 5.3. *Suppose $(S_1, \mathbf{g}_1)$ and $(S_2, \mathbf{g}_2)$ are simply connected oriented surfaces. Let p_0^k be an interior point on S_k, and p_1^k an boundary point on S_k, $k = 1, 2$. There exists an isometric mapping $f : (S_1, \mathbf{g}_1) \to (S_2, \mathbf{g}_2)$, so that $f(p_i^1) = p_i^2, i = 0, 1$. Let $\phi_k : (S_k, \mathbf{g}_k) \to \mathbb{D}$ be the normalized Riemann mapping, such that $\phi_k(p_0^k) = 0$ and $\phi_k(p_1^k) = 1$, λ_k be the conformal factor, $\mathbf{g}_k = e^{2\lambda_k} dzd\bar{z}$, $\tau_k : (\mathbb{D}, dxdy) \to (\mathbb{D}, \mu_k)$ be the Brenier map, where $\mu_k = e^{2\lambda_k} dxdy$. Then*

$$\phi_2 \circ f = \phi_1, \tau_1 = \tau_2,$$

Proof. $\eta := \phi_2 \circ f \circ \phi_1^{-1} : \mathbb{D} \to \mathbb{D}$ is a conformal mapping from the unit disk to itself. Therefore η is a Möbius transformation,

$$\eta(z) = e^{i\theta} \frac{z - z_0}{1 - \bar{z}_0 z}.$$

From $\eta(0) = 0$, we obtain $z_0 = 0$. From $\eta(1) = 1$, we get $\theta = 0$. So $\eta = id$, $\phi_2 \circ f = \phi_1$. Therefore, we get $\lambda_1 = \lambda_2$, so $\mu_1 = \mu_2$. Due to the uniqueness of the Brenizer map, $\tau_k : (\mathbb{D}, dxdy) \to (\mathbb{D}, \mu_k)$ $k = 1, 2$ should be identical. □

Namely, if the Brenier maps are identical, then the surfaces are isometric.

The mapping from the unit disk to itself can be uniquely determined by its Beltrami coefficient. Let $\tau : \mathbb{D} \to \mathbb{D}$, then

$$\mu_\tau := \frac{\partial \tau}{\partial \bar{z}} \Big/ \frac{\partial \tau}{\partial z},$$

where $\partial_{\bar{z}} = 1/2(\partial_x - i\partial_y)$, $\partial_{\bar{z}} = 1/2(\partial_x + i\partial_y)$.

Theorem 5.4 (Measurable Riemann Mapping)**.** *Suppose $\|\mu\|_\infty < 1$, then there exists a diffeomorphism $\tau : \mathbb{D} \to \mathbb{D}$, whose Beltrami coefficient equals to μ. τ is unique up to a Möbius transformation.*

Therefore, in order to compare the Brenier maps, it is sufficient and necessary to compare their Beltrami coefficients.

5.3 Algorithms

Given a simply connected surface $(S, \mathbf{g})$ with total area π, fix an interior point p_0 and a boundary point p_1, then according to Riemann mapping theorem, there is a unique conformal mapping $\phi : S \to \mathbb{D}$, where $\mathbb{D}$ is unit disk, such that $\phi(p_0) = 0$ and $\phi(p_1) = 1$. The mapping ϕ parameterizes the surface, such that the Riemannian metric $\mathbf{g}$ can be represented by $\mathbf{g} = e^{2\lambda}(dx^2 + dy^2)$. The conformal factor defines a measure on the unit disk $\mu = e^{2\lambda}dxdy$. Then there exists a unique Brenier mapping $\tau : (\mathbb{D}, dxdy) \to (\mathbb{D}, \mu)$. The composition mapping $\tau^{-1} \circ \phi : S \to \mathbb{D}$ is an area preserving mapping.

In practice, the surface is approximated by a triangle mesh M, normalized by a scaling such that the total area is π. The conformal mapping $\phi : M \to \mathbb{D}$ can be achieved using discrete Ricci flow method [133]. Then the measure μ can be defined on each vertex $v_i \in M$, as

$$\mu(v_i) := \frac{1}{3}\sum_{jk} Area([v_i, v_j, v_k]),$$

where $[v_i, v_j, v_k]$ is a triangle face adjacent to v_i.

Then the sites are $P = \{\phi(v_1), \phi(v_2), \cdots, \phi(v_n)\}$. The target area vector is $\bar{\mathbf{w}} = \{\mu(v_1), \mu(v_2), \cdots, \mu(v_n)\}$, the power vector $\mathbf{h} = (h_1, h_2, \cdots)$ can be obtained by optimizing the convex energy equation using Newton's method.

Initially, we set all powers to be zeros and translate and scale P, such that P is contained in the unit disk. Compute the power diagram, calculate the areas for each cell w_i. Then compute the dual power Delaunay triangulation, compute the lengths of edges in the diagram and triangulation, form the Hessian matrix H, then update the power $\mathbf{h} \leftarrow \mathbf{h} + H^{-1}(\bar{\mathbf{w}} - \mathbf{w})$. Repeat this procedure until the cell areas are close to the target areas.

Then the power diagram for $\{(\phi(v_i), h_i\}$ partitions $\mathbb{D}$ to convex polygonal cells $\{W_i\}$, the Brenier map is given by $\tau : W_i \to \phi(v_i)$. Compute the centroid of W_i, denoted as c_i. The area preserving mapping is given by $\tau^{-1} \circ \phi(v_i) = c_i$. The algorithm details are illustrated in Alg.8.

5.4 Experimental Results

We applied our area preserving mapping method to various anatomical surfaces extracted from 3D MRI scans of the brain. The baseline T1 images are acquired as part of the Alzheimer's Disease Neuroimaging Initiative (ADNI) [72]. In the paper, the segmentations

Algorithm 8 Area Preserving Mapping

Input: Input triangle mesh M, total area π and area difference threshold δw.

Output: A unique diffeomorphic area preserving mapping $f : M \to \mathbb{D}$, where $\mathbb{D}$ is a unit disk. The area w_i of each cell $W_i \in \mathbb{D}$ is close to the target area $\overline{w_i}$.

1. Run conformal mapping by discrete Ricci flow method [133], $\phi : M \to \mathbb{D}$, where $\mathbb{D}$ is a unit disk. Assign each site $\phi(v_i) \in \mathbb{D}$ with power $h_i = 0$ and target area $\overline{w_i} = \mu(v_i)$ defined above. Translate and scale all sites so that they are in the unit disk.
2. Compute the power diagram and calculate the area w_i of each cell W_i.
3. Compute the dual power Delaunay triangulation, and compute the lengths of edges in the diagram and triangulation to form the Hessian matrix H.
4. Update the power $\mathbf{h} \leftarrow \mathbf{h} + H^{-1}(\bar{\mathbf{w}} - \mathbf{w})$.
5. Repeat step 2 through step 4, until $\|w_i - \overline{w_i}\|$ of each cell is less than δw.
6. Compute the centroid of cell W_i, denoted as c_i. Then the area preserving mapping is given by $\tau^{-1} \circ \phi(v_i) = c_i$, where τ is the Brenier map $\tau : W_i \to \phi(v_i)$.

are done with publicly available software FreeSurfer [42] or FIRST [114]. All surfaces are represented as triangular meshes. All experiments are implemented on laptop computer of Intel Core i7 CPU, M620 2.67GHz with 4GB memory.

5.4.1 Application of Caudate Surface Parameterization

We tested our algorithm on the left caudate nucleus surface. The caudate nucleus is a nucleus located within the basal ganglia of human brain. It is an important part of the brain's learning and memory system, for which parametric shape models were developed for tracking shape differences or longitudinal atrophy in diseases, such as Alzheimers Disease [94] and Parkinsons disease [13], etc.

Figure 28 (a) shows the triangular mesh of a reconstructed left caudate surface segmented by FIRST. The long and slim surface is challenging to compute its parametric surface. For example, a conformal mapping on slim surface usually introduces area distortions at the exponential level and may cause big numerical problems. In contrast, our method evenly embeds the caudate surface to the parametric domain and keeps the area element unchanged. For implementation, we cut a small hole at the bottom of (a) to get an open boundary to make its topology consistent with a disk's. Figure 28 (b) shows that most parts of conformal mapping result shrink towards the center, while the area preserving method shown in Figure 28 (c) gives a good mapping, keeping the same area element, without much numerical error. Figure 29 are the histograms of area distortion of result surface triangles to original surface triangles for conformal mapping and area preserving mapping,

respectively. It shows that conformal mapping cause up to 2^{20} times shrinkage, while area preserving mapping almost keep the same area. In Figure 30, we put circle textures on both conformal mapping result and area preserving result, it gives a direct visualization of our method's correctness. Although multi-subject studies are clearly necessary, this demonstrates our area preserving method may potentially be useful to study some morphometry change to classify and compare different subcortical structure surfaces.

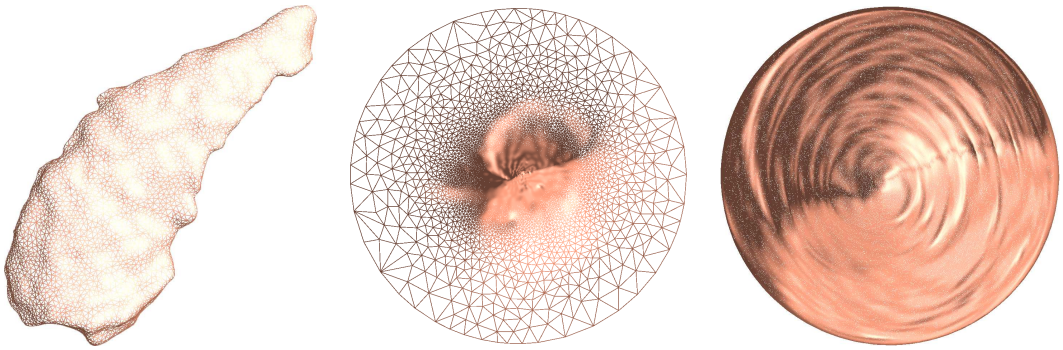

(a) (b) (c)

Figure 28: Comparison of geometric mappings for caudate surface: (a) original caudate surface represented by a triangular mesh; (b) conformal mapping result; (c) area preserving mapping result. The area preserving mapping method evenly maps the surface to the unit disk and eliminates the big distortions close to the upper tip area in (a).

5.4.2 Application of Alzheimer's Disease Diagnosis

For Alzheimer's disease, structural MRI measurements of brain shrinkage are one of the best established biomarkers of AD progression and pathology. And early researches [121, 42] have demonstrated that surface-based brain mapping may offer advantages over volume-based brain mapping [15] to study structural features of brain, such as cortical gray matter thickness, complexity, and patterns of brain change over time due to disease or developmental process. According to prior AD researches [45, 43], the brain atrophy is an important biomarker of AD. The atrophy may not only be area shrinkage, but also have anisotropic directions. Therefore, a good shape signature contains both area and angle deformation information may have a good potential to be a practical biomarker.

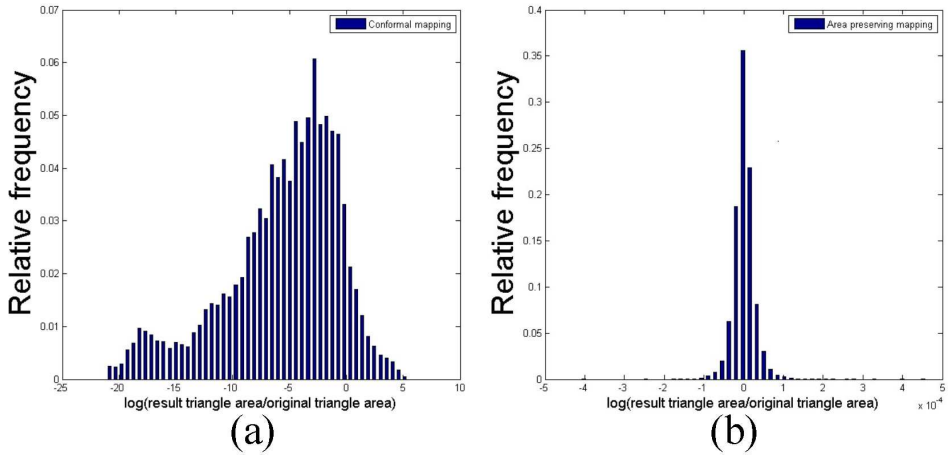

Figure 29: Histogram of area distortion: (a) area distortion of conformal mapping; (b) area distortion of area preserving mapping. The area preserving mapping result shows a much smaller area distortion.

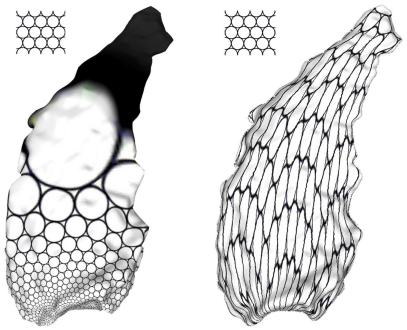

(a) (b)

Figure 30: Circle packing of different geometric mappings: (a) circle packing of conformal mapping. (b) circle packing of area preserving mapping. The parameterizations are illustrated by the texture map of a uniformly distributed circle patterns on the caudate surface, the circle texture is shown in the upper left corner. In (a), the circles stay the circle but the circle areas change dramatically on the upper tip area. In (b), the circles become ellipses but the areas stay unchanged.

In this work, we proposed to use Beltrami coefficients [46] computed from area preserving mapping result to conformal mapping result, as a shape signature to analyze the human brain cortical surfaces among AD patients and CTL subjects. This kind of signature combines both area and angle information so that it may provide more powerful statistical ability in the AD diagnosis in the early stage.

Data Source: Our data included baseline MRI images from 50 AD patients and 50 healthy control (CTL) subjects (Age: AD: 75.86 ± 7.65; CTL: 74.56 ± 4.16; MMSE score: AD: 22.96 ± 2.15; CTL: 29.02 ± 1.04). We used Freesurfer's automated processing pipeline [42] for automatic skull stripping, tissue classification, cortical surface extraction, vertex correspondences across brain surfaces and cortical parcellations. According to work [37], we labeled the functional areas of a left brain cortical surface shown in Figure 31 (a) and (b).

Cortical Surface Parameterization Results Figure 31 (c)-(f) are the conformal mapping results and area preserving mapping results of the left brain cortical surfaces of a healthy control subject and an AD patient. On both surfaces, we cut a hole around the unlabeled subcortical region [37]. After the cutting, the remaining cortical surface becomes a genus zero surface with one open boundary. Both algorithms compute a diffeomorphism map between the cortical surface and a unit disk. The results show that the conformal mapping results have much more area distortion on the areas close to the boundary while the area preserving mapping provides a map which preserves the area of each individual functional area. The area preserving mapping has a potential to better visualize certain sulci areas which are deeply buried under gyri, and hence to provide a tool for a more accurate manual landmark delineation operation.

Numerical Analysis of Signatures among Healthy Control Subjects and AD Patients The Beltrami coefficient is a complex-valued function defined on surfaces with supreme norm strictly less than 1. It measures the local conformality distortion of surface maps. We tested the discrimination ability of our shape signature on a set of left and right brain surfaces of 50 CTL subjects and 50 AD patients. Previous work [113] indicated ten functional areas having significant atrophy in AD group, such as Middle Temporal, Superior Temporal, etc. Among the 35 functional areas, we chose 3 regions for study, which are Middle Temporal, Superior Temporal and Fusiform as shown in Figure 31 (a) and (b). Figure 32 shows the average histograms of the norm of Beltrami coefficients of 50 AD patients and 50 CTL subjects on these three functional areas. The histograms show the norm of Beltrami coefficients of cortical surfaces of AD patients are obviously larger than those of healthy control subjects. It means that AD patients may have larger conformality distortion in both area and shrinkage directions because AD patients may suffer a more serious atrophy of brain structures which result from a combination of neuronal atrophy, cell loss and impairments in myelin turnover and maintenance [43].

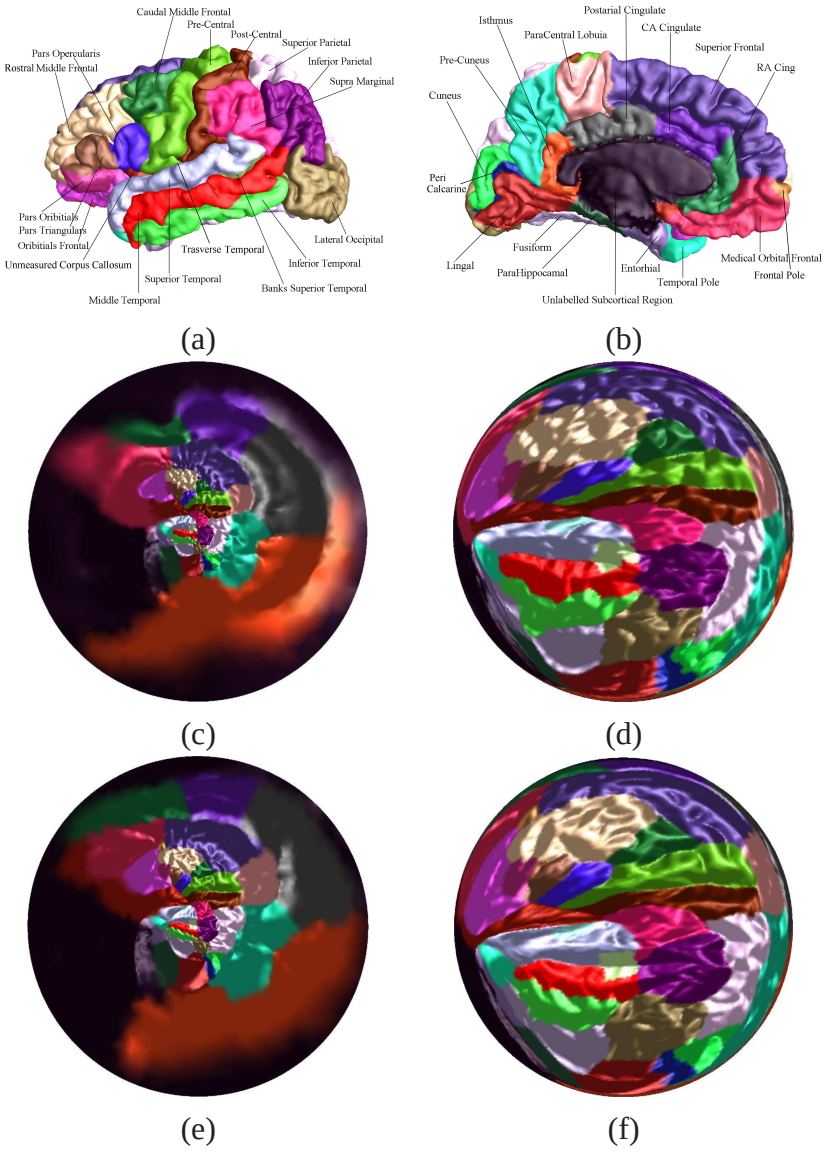

Figure 31: (a) and (b) illustrate the functional areas on the left brain cortex [37]. (a) Lateral view. (b) Medial view. (c) and (e) are conformal mapping results of a CTL subject and an AD patient, respectively; (d) and (f) are area preserving mapping results of a CTL subject and an AD patient, respectively. The area preserving mapping may provide a better visualization tool for tracking sulci landmark curves on cortical surfaces.

Classification among Healthy Control Subjects and AD Patients We further hypothesize that the our computed Beltrami coefficients may help early AD detection. We performed the classification between AD and CTL groups in the current ADNI dataset. For

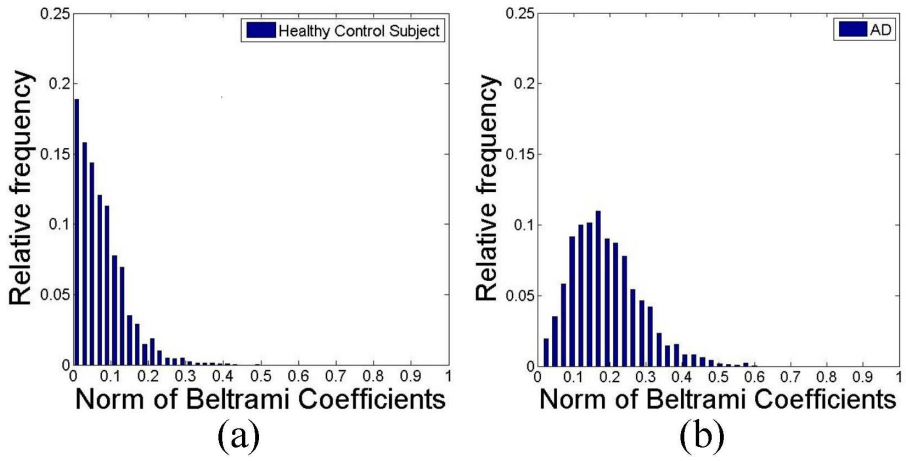

Figure 32: Histograms of Norm of Beltrami Coefficients: (a) result of healthy control subjects. (b) result of AD patients. The AD result demonstrated a stronger and more anisotropic deformation due to a more serious atrophy of brain structures.

the classification experiment, 80% of each category of both left and right brain cortical surfaces are set to be training samples and the remaining 20% as testing samples. To obtain fair results, we randomly selected the training set each time and computed the average recognition rate over 1000 times. We used Support Vector Machine (SVM) [3] as a classifier, where the linear kernel function was employed, and we used C-SVM and chose $C = 5$ by running cross validation. Table 3 shows 95 percent confidence interval for average recognition rate of our method is $87.50\% \pm 0.55\%$. For comparisons, we also computed area based method and volume based method. For area based method, we computed the surface areas for the base domain and 3 regions mentioned above on each hemisphere as a signature $(Area) = (A_0, A_1, A_2, A_3)$; 95 percent confidence interval for the average recognition rate is $70.00\% \pm 0.73\%$. We also calculated the volume of each hemisphere as a signature (*Vol*), 95 percent confidence interval for the average recognition rate is $62.50\% \pm 0.57\%$. Although the above two methods are not popular signatures for AD study in the literature and a more careful study such as [32] is necessary, the results helped illustrate the various nature of our testing data and showed the potential of our proposed shape signature.

Method	Rate $\%$
Area	$70.00\% \pm 0.73\%$
Volume	$62.50\% \pm 0.57\%$
Our method	$87.50\% \pm 0.55\%$

Table 3: Average recognition rate($\%$) for applying different signatures among 50 healthy control subjects and 50 AD patients. In the experiments, 80% data are used for training and the remaining for testing. The experiments were repeated over 1000 times and 95% confidence intervals are reported here.

6 Optimal Mass Transport for Visualization

We propose a novel visualization framework using the optimal mass transport technique, based on Monge-Brenier theory. Our optimal transport map approach is rigorous and solid in theory, efficient and parallel in computation, yet general for various applications. By comparison with the conventional Monge-Kantorovich approach, our method reduces the number of variables from $O(n^2)$ to $O(n)$, and converts the optimal mass transport problem to a convex optimization problem, which can now be efficiently carried out by Newton's method. Furthermore, our framework includes the area weighting strategy that enables users to completely control and adjust the size of areas everywhere in an accurate and quantitative way. Therefore, our method significantly reduces the complexity of the problem, and improves the efficiency, flexibility and scalability during visualization. Our framework, through combining conformal mapping and optimal mass transport mapping, serves as a powerful tool for a broad range of applications in visualization and graphics, especially for medical imaging. We provide a variety of experimental results to demonstrate the efficiency, robustness and efficacy of our novel framework.

6.1 Overview

With the fast generation of large and complicated data nowadays, it is desirable to develop new frameworks aiming at generating a visualization of the entire data needed for navigation, detection, exploration and a global understanding of selected objects or regions of interest (ROIs). Complex geometric structures are often better visualized and analyzed by mapping the surface properties, such as normal map, angle, or area, to a simple canonical

domain, such as a rectangle or a sphere. Surface flattening and texture mapping offer a good way of visualizing a surface section by enabling the visualization of all surface parts within a single planar image.

In general, surface flattening and texture mapping unavoidably introduces distortions. There are two types of distortions, angle distortion and area distortion. A mapping, which is both angle preservation and area preservation, must be isometric. Therefore, the surface must have zero Gaussian curvature everywhere, namely a developable surface or a ruled surface. For general surfaces, one can only choose either angle-preservation mapping or area-preservation mapping, but never both of them simultaneously.

Angle-preservation (conformal) mapping/surface flattening preserves local shapes, and thus has been broadly used in many feature oriented applications in visualization and medical imaging. However, conformal method usually substantially distorts area, which fails to display accurate size of area, including height, width, thickness or diameter of ROIs. Unfortunately, these distorted area parameters are extremely important in many medical image recognition and auto diagnosis applications, such as brain fold detection [38] or colon polyps detection and diagnosis [62, 138]. Moreover, it is well known that conformal mapping induces severe area distortions for surfaces with long tube shapes, such as the elongated lion head model, as shown in Fig. 33. This disadvantage derives from the fundamental obstacle of conformal mapping theory and we can not easily overcome it. Imagine a cylinder $\mathbf{r}(\theta, z) = (\cos\theta, \sin\theta, z)$, a conformal mapping $\phi(\theta, z) = e^{-z}(\cos\theta, \sin\theta)$ maps it to the unit disk, the area distortion factor e^{-2z} is exponential with respect to the height z, and in practice easily exceeds the machine precision.

By comparison, area-preservation mapping can generate accurate and information lossless mapping results, which is a key objective for many medical imaging applications, with the ability to carry out measurements for detecting anatomic abnormalities. For example, in virtual colonoscopy, the physician may want to measure and compare different sizes of polyps, to determine disease conditions and cancer risks [58]. A special case of this problem also occurs in any application where volume or area measurement is critical (e.g. brain data in [38, 50, 150]). From human cognition perspective, area-preservation mapping and flattening can also enhance the viewer's ability to easily recognize the component-aware patches or long branch parts distribution of models, and consequently understand the local feature with the knowledge of a global structure (Fig. 33). Therefore, area-preservation mapping has vast potentials to be applied to many related visualization and graphics applications.

To simultaneously tackle the above challenges, we develop a flattening framework which provides a global view of the surface with a minimum of area distortions, while still, at the same time, maximally preserving local angle/shape features on the flattened surface. In this work, we introduce our solution to this problem using the technique of optimal mass transport (OMT), based on Monge-Brenier theory [24].

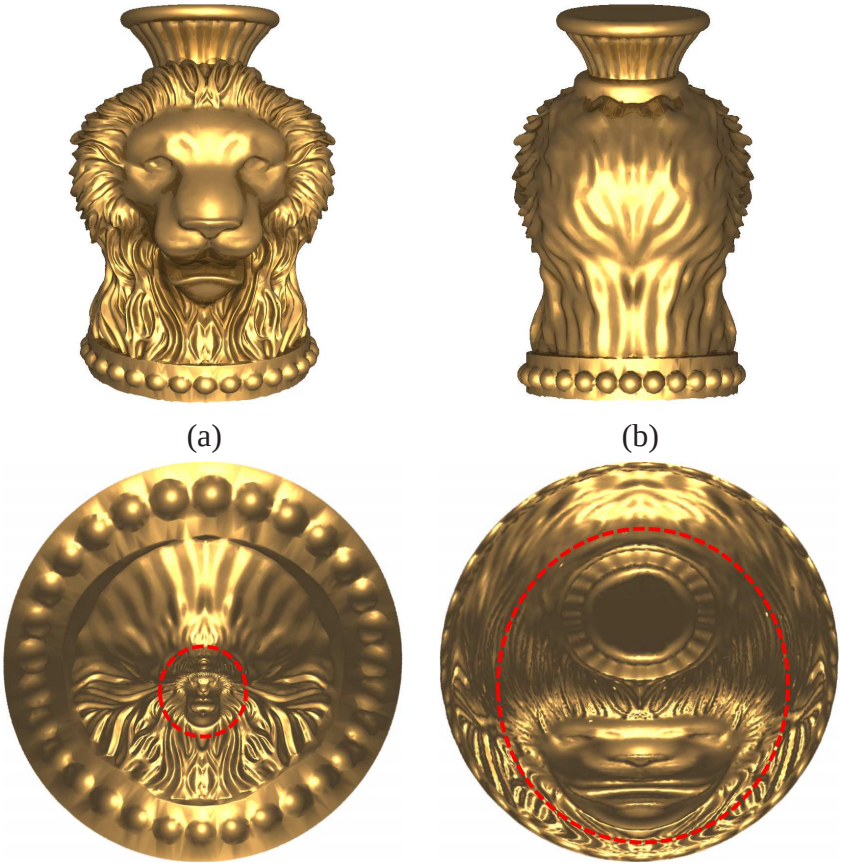

Figure 33: Disadvantages of conformal mapping for elongated shapes. (a) Front view and (b) back view of the elongated lion head surface model. Surface flattening results induced by (c) conformal mapping and by (d) our area-preservation mapping. Conformal mapping generates major area distortions for both the lion face and the vase regions, while our method can preserve them accurately for clear view without losing any information (highlighted by the red circles).

6.1.1 Related Work

We review research work on optimal mass transport that are most relevant to our approach targeting both algorithms and applications, and discuss the comparisons.

Theoretic Development. In 1781, Monge [98] has formulated the OMT problem. In the 1940's, Kantorovich [78] has proved the existence and the uniqueness of the optimal transport plan. At the end of 1980's, Briener has proved that the optimal transport map

is the gradient map of a convex function, when the transportation cost is the quadratic of the Euclidean distance. In the discrete case, Brenier's result is equivalent to the existence and the uniqueness of the convex polyhedron with prescribed projected facet areas. This has been first shown by Alexandroff [9] in 1920's. Aurenhammer [17] has shown the connection between Brenier's construction and power diagram, where the existence has been proven. Recently, the connection between the discrete optimal transport map and the discrete Monge-Ampere equation, which is based on variational approach, has been given by Gu et al. [49].

Monge-Kantorovich Approach. Most existing works are based on Monge-Kantorovich approach. Bonnel et al. [23] have proposed a method for interpolation between distributions or functions based on advection instead of blending for rendering purposes. This method decomposes distributions or functions into sums of radial basis functions (RBFs), then solves a mass transport problem to pair the RBFs and applies partial transport to obtain the interpolated function. Rubner et al. [106] have proposed a content based image retrieval method using the earth mover distance as a metric for the OMT problem. However, it fails to give a warped grid, an essential requirement for image registration and image morphing. Rehman et al. [126] have listed several advantages of the OMT method for multiresolution 2D/3D nonrigid registration. Meanwhile, they stress the fact that the optimization of OMT is computationally expensive and emphasize that it is important to find efficient numerical methods to solve this issue.

The following techniques are based on Monge-Brenier's approach. Merigot [97] has proposed a multiscale approach to solve the optimal transport problem. To solve an optimal transport problem between a measure with density μ to a discrete measure ν, this method build a sequence $\nu_0 = \nu, \ldots, \nu_L$ of simplifications. Then, it first solves the easier transport problem between μ and ν_L, and use the solution of the problem to be the initial guess for the optimal transport between μ and $\nu_{(L-1)}$. This step is iterated until a solution to the original OMT problem. The method is applied for computing the Wasserstein distances between probability distributions, and for image interpolation. de Goes et al. [35] have provided an optimal transport driven approach for 2D shape reconstruction and simplification. They have further presented a formulation of capacity constrained Voronoi tessellation as an optimal transport problem for image processing [34]. This method produces high quality blue noise point sets with improved spectral and spatial properties. Compared to our method, de Goes's method only applies between 2D domains while our method maps a 3D surface to a 2D domain. Our method can further lead to a fast, scalable algorithm to generate high quality blue noise point distributions of arbitrary density functions.

Tannenbaum group has introduced this novel approach. The basic idea is to construct an initial mass preservation mapping, then deform the mapping such that the total transportation cost is reduced and the deformed mapping is still mass preserving. Namely, it designs a gradient flow in the space of all mass preservation mapping space. Haker et al. [61] have

presented a method for image registration and warping based on the OMT. The method is parameter free and has the unique global optimum. However, its linear programming of the optimal map can be solved with $O(n^2)$ variables, which is prohibitively expensive when n is large. Zhu et al. [148] have combined conformal mapping and area-preservation mapping for flattening branched physiological surfaces, such as vessels. The optimal transport map is carried using the minimal flow approach. Similar method has been applied for image morphing [149]. Rehman et al. [126] have applied the minimizing flow approach for the OMT with applications to non-rigid 3D image registration. The implementation also employs multi-grid and parallel methodologies on a consumer graphics processing unit (GPU) for fast computation. Although computing the optimal map has been shown to be computationally expensive in the past, we show that our approach is orders of magnitude faster than previous work. Dominitz and Tannenbaum [38] have proposed to use the OMT for texture mapping. The method begins with an angle-preservation mapping and then corrects it using the mass transport procedure derived via a certain gradient flow. A multiresolution scheme is incorporated into the flow to obtain fast convergence to the optimal mapping. Both methods require designing divergence free vector fields to drive a diffeomorphic flow to minimize the energy.

Comparison. Our method mainly follows the Monge-Brenier approach, based on the variational principle [49]. Comparing to the state-of-the-art techniques, it has many merits as follows:

- Comparing to the Monge-Kantorovich approaches [23, 78, 126], our method only requires $O(n)$ variables. In contrast, Kantorovich approach requires $O(n^2)$ variables. Therefore, our method greatly reduces the storage complexity, and it is thus much more efficient.

- Comparing to the Monge-Brenier based approaches [34, 35, 97], all the existing methods are for image processing tasks. Our method however focuses on surfaces. For image processing, the samples are relatively uniform, and therefore, the computation is relatively stable. In our case, the sample points are produced by the conformal mapping, the sample density is highly non-uniform, and thus conventional methods are very vulnerable and error-prone for the large area distortions induced by the conformal mapping. Our experiments indicate that conventional methods are not robust enough. Therefore, we have specially designed our *step length control* algorithm (Section 4.2) to improve the robustness.

- Comparing to the minizing flow methods [38, 61, 149], the solution of latter is equivalent to a gradient descend method for optimizing the transportation cost. In contrast, our method is equivalent to the Newton's method to optimize a convex energy, which has a higher order convergence rate. Therefore, our method is more efficient.

6.2 Algorithm

This section gives the detailed algorithms for the optimal mass transport map generation. Fig. 34 shows the pipeline of our OMT based area-preserving framework. The input surface is approximated by a triangular mesh M, with vertex sets V, face set F and a convex planar domain Ω, represented as a convex polygon. Our goal is to compute an area-preserving map from the mesh M to the planar domain Ω. Our discrete algorithm is based on the Monge-Briener theory and utilizes the variational principle to solve the optimization problem. For the input, aiming to get ROIs with arbitrary shape (e.g., irregular shape of the brain folds), we utilize the saliency map [81] to for the ROI detection. Once users specify local area weight $\overline{w_i}$ everywhere, the system will iteratively solve the OMT map and refine the area-preserving result that yields strict equality of weighted sizes of area between the input surface and flattened plane. The area weighting parameter $\overline{w_i}$ is defined as weighted areas in 2D or weighted volumes in 3D. After the generation of the OMT map (bijectively area-preservation mapping), we directly apply the ROI guided texture mapping to obtain the output.

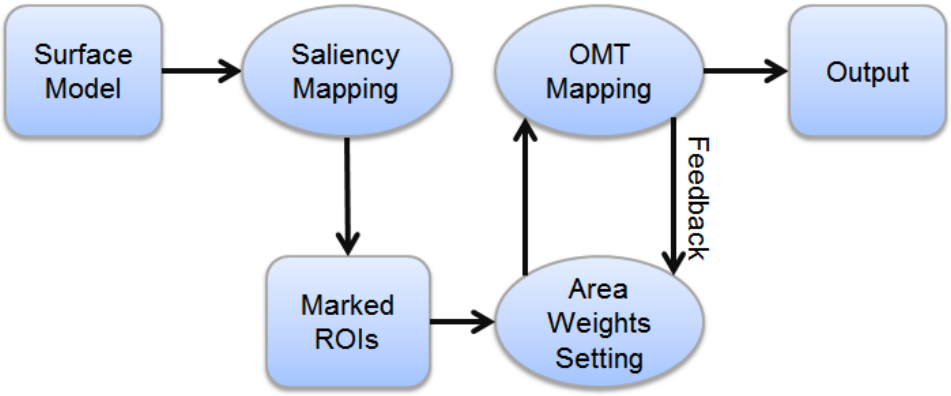

Figure 34: The pipeline of our OMT based area-preserving framework.

Merits of Saliency Map. The application of saliency map can (1) accurately detect arbitrary ROI shape to obtain the accurate area preservation; and (2) provide hierarchical resolution of surface models, supporting the reduction of triangles in the context area, while preserving high resolution ones in ROIs, for the purpose of fast computation. Take the

brain model as an example, instead of using the original model with 100K faces, with the saliency guided ROI detection, we can significantly reduce the face account to 10K or less (data oriented).

6.2.1 Initialization

Our algorithm uses the conformal mapping result (angle preservation) to set up the initial position for each vertex v_i. We first normalize the mesh such that its total area equals to the area of the planar domain Ω. We then initialize a discrete conformal mapping $\phi : M \to \mathbb{D}$. In our framework, we utilize the discrete Ricci flow method [133] to achieve this step. Then, after assigning each vertex a target area $\bar{w_i}$, we define for each vertex $v_i \in V$ the Dirac measure associated with it, as one third of the total area of faces adjacent to it,

$$\mu(v_i) = \frac{1}{3} \sum_{[v_i,v_j,v_k]\in F} Area([v_i, v_j, v_k]),$$

where $[v_i, v_j, v_k]$ represents the triangle formed by vertices v_i, v_j and v_k.

We use the images of all the vertices as the sample points of the unit disk $\mathbb{D}$, $Y = \{\phi(v_i)|v_i \in V\}$, each sample $\phi(v_i)$ is associated with the Dirac measure $\mu(v_i)$. By translation and scaling, we transform Y to be contained by Ω.

6.2.2 Optimal Mass Transport Mapping

According to the Monge-Briener theory, we need to find the height vector $\mathbf{h} = (h_1, h_2, \cdots, h_n)$. Fix a height vector, the support planes are given by $\pi_i(\mathbf{h}) : \langle x, y_i\rangle + h_i$, the convex function is $u_{\mathbf{h}}(x) = \max_i\langle x, y_i\rangle + h_i$, and its graph $G(\mathbf{h})$ can be computed as upper envelope of the supporting plane $\pi_i(\mathbf{h})$. The projection of $G(\mathbf{h})$ onto Ω forms a polygonal partition $\Omega = \bigcup_i W_i(\mathbf{h})$.

In order to preserve the area of cell W_i, we need to iteratively update the virtual variable for each vertex with height vector $\mathbf{h} = (h_1, h_2, \cdots, h_n)$ (details in the paragraph Initial Height Vector below). Thus, in each iteration, we first compute the power diagram, using each vertex as a point and the weighted radius as the power in the diagram. Then, in step 3, we compute the dual triangulation of this calculated power diagram (details in the paragraph Power Diagram below). We record every edge length in both the power diagram and its dual triangulation in this step to form the Hessian matrix. In step 4 (the last step of each iteration), we use Newton's method to solve the gradient energy equation (Eqn. 3.27) and to update the height vector $\mathbf{h}$ until it satisfies that $\|w_i - \overline{w_i}\|$ of each cell is less than δw (details in the paragraph Hessian Matrix below). Finally, we update the vertex position as the center of the power Voronoi diagram to obtain the area-preserving parameterization result.

Initial Height Vector. At the initial stage, we scale and transform a point set Y to ensure they are contained in Ω, and then compute the Voronoi diagram with zero power weights,

Algorithm 9 Area-Preservation Mapping

Input: Input triangular mesh M, total area π and area difference threshold δw.

Output: A unique diffeomorphic area-preservation mapping $f : M \to \mathbb{D}$, where $\mathbb{D}$ is a unit disk. The area w_i of each cell $W_i \in \mathbb{D}$ is close to the target area $\overline{w_i}$.

1. Run conformal mapping by discrete Ricci flow method [133] $\phi : M \to \mathbb{D}$, where $\mathbb{D}$ is a unit disk. Assign each site $\phi(v_i) \in \mathbb{D}$ with zero power weight, and target area $\overline{w_i} = \mu(v_i)$ defined above. Translate and scale all sites so that they are in the unit disk.
2. Compute the power diagram and calculate the area w_i of each cell W_i.
3. Compute the dual power Delaunay triangulation, and compute the lengths of edges in the diagram and triangulation to form the Hessian matrix of the convex energy in Eqn. 3.24 .
4. Update the power $\mathbf{h} \leftarrow \mathbf{h} + H^{-1}(\bar{\mathbf{w}} - \mathbf{w})$.
5. Repeat step 2 through step 4, until $\|w_i - \overline{w_i}\|$ of each cell is less than δw.
6. Compute the centroid of cell W_i, denoted as c_i. Then the area-preservation mapping is given by $\tau^{-1} \circ \phi(v_i) = c_i$, where τ is the Brénier map $\tau : W_i \to \phi(v_i)$.

or namely, with initial heights $h_i = -1/2\|y_i\|^2$, where $\|y_i\|^2$ is the point position in the planar domain. This guarantees that all the cells are non-empty.

Power Diagram. The OMT based area-preserving computation for the partition of Ω is equivalent to the classical power diagram in computational geometry [49]. Given a point set $Y = \{y_1, y_2, \cdots, y_n\}$, each point y_i associated with the weight w_i as its power, the power distance from any point x to y_i is defined as:

$$Pow(x, y_i) = \frac{1}{2}\|x - y_i\|^2 - \frac{1}{2}w_i,$$

Then, the power diagram is the Voronoi diagram when we use the power distance instead of the standard Euclidean distance.

In our method, the partition induced by the convex function $u_{\mathbf{h}}$ in Eqn. 3.18 is equivalent to the power diagram with the power weight:

$$w_i = 2h_i + \langle y_i, y_i \rangle.$$

Therefore, the computation can be carried out using power diagram functionalities in standard computational geometry library, such as CGAL [7]. The construction of the power Voronoi diagram and the power Delaunay triangulation are illustrated in Fig. 35.

Hessian Matrix. In our algorithm, we represent the gradient of energy $\nabla E(\mathbf{h})$ in Eqn. 3.27 as the area changes of cell $(\bar{\mathbf{w}} - \mathbf{w})$, where $\bar{\mathbf{w}}$ and $\mathbf{w}$ as weighting values. Then,

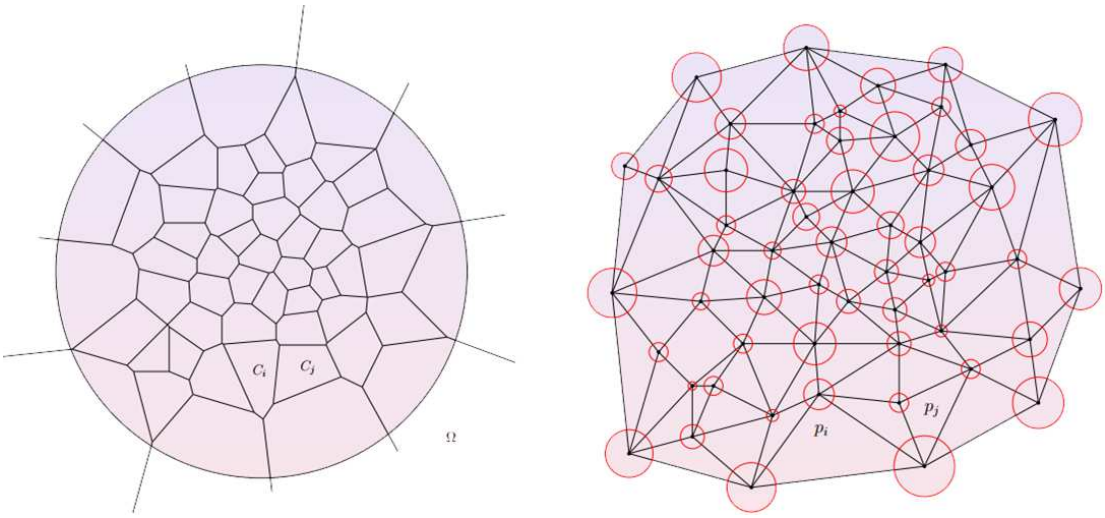

(a) (b)

Figure 35: Construction of (a) the power Voronoi diagram and (b) the power Delaunay triangulation.

compute the dual triangulation and the cell areas to form the gradient, as in Eqn. 3.27,

$$\nabla E(\mathbf{h}) = (Area(W_i(\mathbf{h}) \cap \Omega))$$

Following the theory proposed by Gu et al. [49], in order to form the Hessian as in Eqn. 3.28, we compute all edge lengths e_{ij} and the dual edge lengths $\bar{e}_{ij}$ from the power diagram and its dual triangulation (Fig. 35). Then, we use the following matrix: $H(\mathbf{h}) = (h_{ij}(\mathbf{h}))$, where

$$h_{ij}(\mathbf{h}) = \begin{cases} -|e_{ij}|/|\bar{e}_{ij}| & i \neq j, W_i \cap W_j \cap \Omega \neq \emptyset \\ -\sum_{k \neq i} h_{ik} & i = j \\ 0 & otherwise, \end{cases}$$

h_{ij} is the (i, j) entry of a matrix, ($i \neq j$) is the off diagonal entry, and the diagonal entry is defined as $h_{ii} = -\sum_{k \neq i} h_{ik}$ (namely, h_{ii} is equal to the sum of all off diagonal entries).

Then, we use Newton's method to update the height vector

$$\mathbf{h} \leftarrow \mathbf{h} + \epsilon H(\mathbf{h})^{-1} \nabla E(\mathbf{h}),$$

where ϵ is the step length.

Step Length Control. During the computation, it is crucial to ensure that all the cells $W_i(\mathbf{h}) \cap \Omega$ are non-empty. Suppose at step k all the cells are non-empty, then, we update

$\mathbf{h_k} \leftarrow \mathbf{h_k} + \epsilon H(\mathbf{h}_k)^{-1} \nabla E(\mathbf{h_k})$. If some cells are empty in the power diagram induced by $\mathbf{h}_{k+1}$, we will return to $\mathbf{h}_l$, shrink the step length ϵ to be $1/2\epsilon$, and try again. If some cells are still degenerated, we shrink the step length iteratively, until all the power cells are non-empty.

Following the implementation details listed in Alg. 9, we have tested our algorithms on different surface models (See Section 5). For practical implementations, we may need to deal with surface models with different topologies, such as the earth and brain models which are genus zero without any boundary, and map and graph cases which are genus zero with an open boundary. The basic idea is to make the topologies of the source domain and the parameter domain consistent. For example, if we want to map a genus zero surface without an open boundary, such as the brain surface, to a unit disk parameter domain, we cut a very small hole on the surface to get an open boundary so that the source domain and parameter domain have the consistent topology.

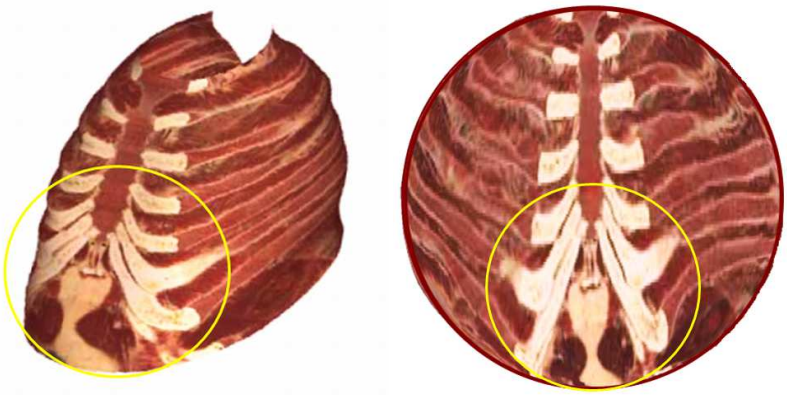

(a) (b)

Figure 36: Surface flattening of a chest model using our area-preservation mapping for direct display and accurate measurement. The yellow circles highlight the corresponding ROIs between (a) the 3D surface model and (b) the 2D flattening plane.

6.3 ROIs Guided Texture Mapping

After computing the bijective area-preservation surface mapping between the 3D surface model and the flattened 2D disk or rectangular parameter domain, the texture mapping is

straightforward with the ROIs guided alignment. With respect to user predefined mapping criteria (e.g., fix the disk boundary or fix the four corner points of a rectangular domain with the alignment of ROIs), the bijective texture mapping between parameterizations and image pixels is syntactically and semantically trivial. We directly call texture mapping functions provided by OpenGL with bilinear interpolation, which is fast and easy to implement. Moreover, we consider model shape and rendering factors, such as depth, view angle, and camera position to obtain reality style visualization, especially for medical data. The pixel color and alpha can be adjusted by the user defined transfer functions.

Our OMT-MAP algorithm can also fully control the local areas of different regions of the surface. By adjusting the measure vector μ, our method can control the areas of different local regions, magnifying regions of interest and shrinking unimportant ones. This allows more parameter spaces to be allocated for regions with richer geometric or textural features, and improves the rendering quality and matching accuracy.

Figure 37 demonstrates this merit, where the buddha's head ((a) and (d)) is magnified by different zooming factors, and the complementary part is shrunk accordingly (e)-(h). Basically, for vertices in the head region, we multiply their measures by the zooming factor, and then normalize the total area to be invariant. The importance-driven mapping results (e)-(h) show more details on the parameter domain than the angle-preserving result (b). Such flexibility controls are particularly useful for visualization or a focused region of interest shape analysis.

6.4 Medical Applications

We first test our method using various medical data. Our highly area-preserving results can be obtained in an interactive-rate, even for various large and complicated datasets. For every medical dataset acquired from CT or MRI, we start from using the visualization toolKit (VTK) [80] to convert a volume dataset to a triangulation mesh as the input, with filters to remove noise and aliasing. Then, we can utilize our mapping framework to achieve various visualization results.

Easy and Accurate Area Measurement. Fig. 36 shows a major advantage of our area-preservation mapping and flattening method. Our mapping framework can bijectively project the 3D surface model into a unit 2D disk, so the doctor can directly and accurately visualize and measure the size of the entire ROI area without repeatedly rotating and scaling.

Saliency Feature Guided Area-preservation Mapping. We use saliency map [81] guided area-preservation mapping for diverse computer aided detection (CAD) applications. Fig. 38 shows the design detail. After extracting the surface model from CT colon data (Fig. 38a), we use the electronic biopsy [68], working as saliency map, for the polyp detection (Fig. 38b). Our area-preservation flattening framework is only applied in the detected

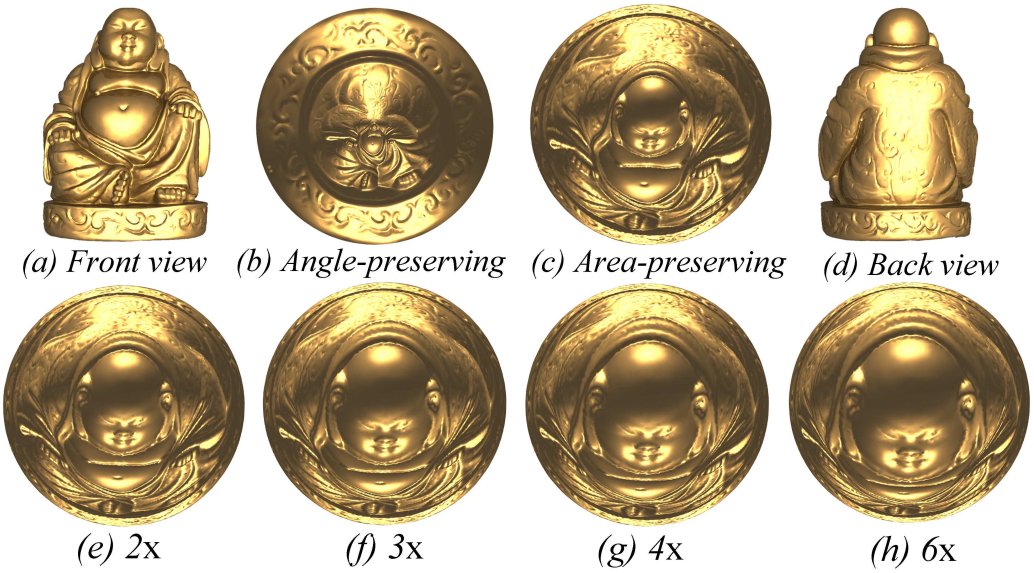

Figure 37: Importance-driven parameterization of a Buddha model.

ROIs, providing an area-preserving view of polyps for the accurate measurement of the diameter and the size of area (verified by the doctor marked measurement as ground truth in the original 3D surface model). By comparison with the conformal mapping method, our framework still preserves major shape characteristics of the colon surface (e.g., colon folds) without any obviously visual distortion (Fig. 38c).

Arbitrary Area Weighting Scheme. Flattening the brain surface with area preservation is important to visualize and study neural activity or to detect diseases/disfunctions [151]. For the easy recognition of different brain folds, we use colors to mark different folds as the ROIs (Fig. 27a and Fig. 27b). In contrast to the conformal mapping result (Fig. 27c), Fig. 27d shows our area-preservation mapping result using the MRI brain dataset, which accurately displays accurate sizes of brain folds without severely compressing or stretching. Moreover, users can set different weight coefficients in ROIs to flexibly adjust sizes of different ROI areas (default 1X: equal area).

6.5 Informatics Applications

With the general application property of parameterization and texture mapping, we can easily apply our framework for various informatics applications including earth map, city map and graph.

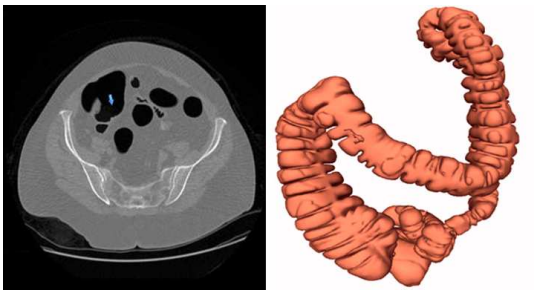

(a)

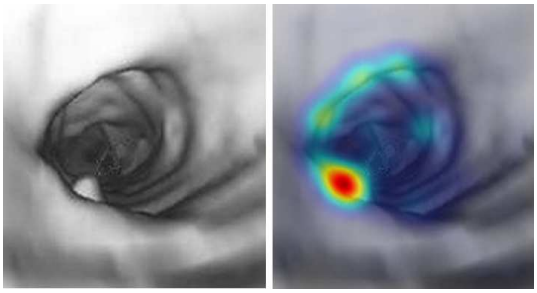

(b)

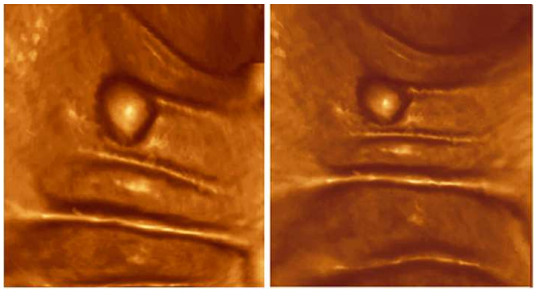

(c)

Figure 38: Saliency map guided area-preservation mapping using a colon model. (a) A colon surface, extracted from CT slices. (b) Possible polyps detected using the saliency map [81]. (c) Surface flattening results using (Left) our area-preservation mapping and (Right) conformal mapping. By comparison, our result generates the accurate polyp size for area measurement (verified by the doctor marked area measurement of the polyp as ground truth) without any severe angle distortion.

Earth Map. The fundamental challenge for earth visualization lies at mapping the sphere earth model to a planar domain with maximal information preserved. Direct projection only projects the half sphere, and then causes severe information lost (Fig. 39b). The state-of-the-art method, such as conformal mapping (Fig. 39c), preserves the whole sphere with angle preservation, but severely compresses some continents while inappropriately enlarging others without any control. By comparison, our method (Fig. 39d) can keep the

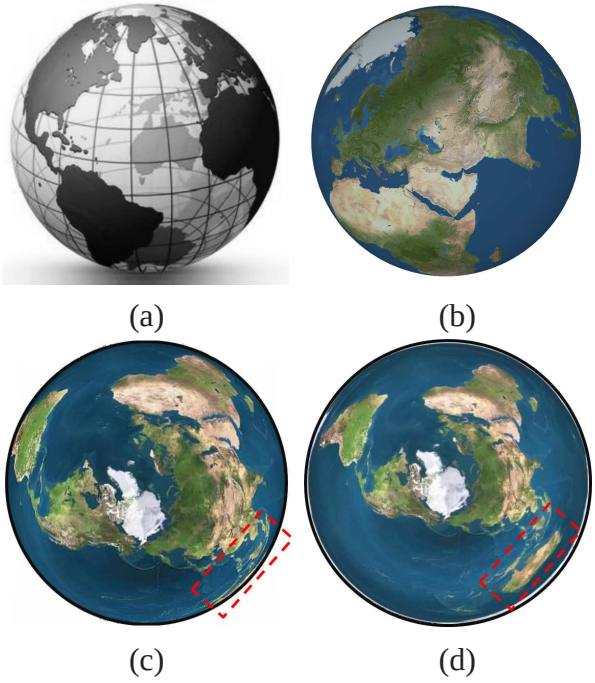

Figure 39: Different mapping results and comparisons using an earth surface model. (a) A 3D earth model. (b) Direct projection mapping with large information loss. (c) Conformal mapping result is with large area distortions, while (d) our area-preservation mapping result is with accurate area preservation and small angle distortion (highlighted by the red frames).

original areas for all major continents, providing the accurate size and area impression for users.

City Map. Our system also provides a direct multiresolution display, functioned as a "magic-lens" to reveal additional details in the ROIs. Our method makes the multiscale alignment accurate but easy without the need of any predefined landmark, due to the accurate area preservation. As shown in Fig. 40, our method generates multiresolution texture mapping to reveal additional street information of the city map. The result demonstrates that our method can well magnify the ROI without causing any obvious distortion.

Network Graph. Our system can generate various visual displays for the graph visualization to satisfy diverse user requirements, due to the flexible weight settings. We showcase its merit using a network visualization example from the AT&T graph library [8], as shown in Fig. 41a. Each graph node stands for a network station, while each straight line depicts direct connection between two neighbor nodes. Fig. 41b enlarges the radius of the

Figure 40: Multiresolution view without any predefined landmarks. (a) The original New York city (NYC) map. (b) NYC map with multiresolution texture images. The red frames highlight the corresponding multiresolution texture maps in the ROI. (c) Area manipulation result with a detailed view to show additional street information. The high resolution detail view can be easily aligned/merged into the low scale map without using any landmark due to the accurate area preservation.

central core to increase the node separation, while compressing exterior nodes to further reduce the potential attention. Fig. 41c shows another area manipulation style: compressing central nodes while enlarging exterior nodes for further separation. There is no efficient way to generate a similar result using either geometry methods (e.g., conformal magnifier [145]) or deformation methods (e.g., moving least squares [143]). Taking a close look at Fig. 41d, the conformal magnifier fails to flexibly control magnification ratios in both focus and context regions. It excessively enlarges the central core area, while compressing exterior nodes without any control. By comparison, our system can easily manipulate the size of area everywhere to generate a user preferred view with appropriate node distributions.

Hierarchical Magnification. We can directly apply our mapping framework as a cascaded magnifier: applying the same magnifier repeatedly on the prior computing magnification result to obtain exponentially increasing magnification ratios. Since our method can accurately preserve the size of area by setting the target weight, we can guarantee that the final target region would be precise after each magnification process. Fig. 42 shows that our hierarchical magnification can easily and accurately reach the high magnification ratio.

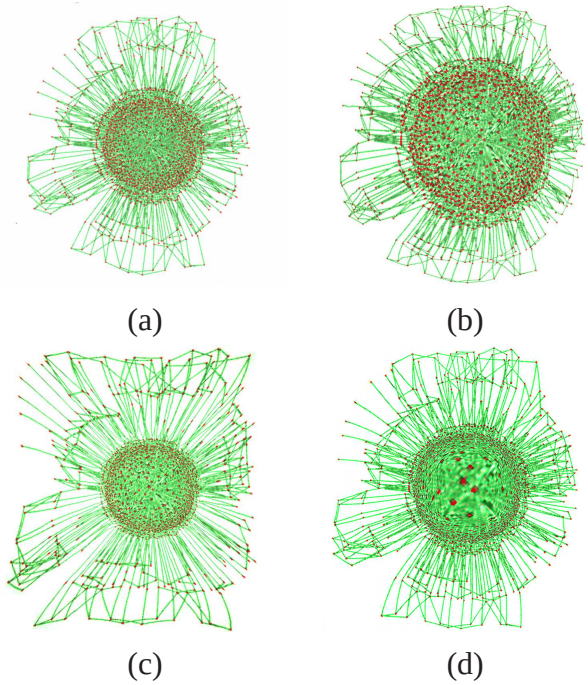

Figure 41: Mapping comparisons using the network graph. (a) Original graph layout [8]. Magnification results with (b) the central nodes as the ROI, and with (c) the surrounding exterior nodes as the ROI, using our framework. (d) Magnification result using conformal magnifier [145]. By comparison, our method has flexible area control to generate various views.

7 Conclusion

In this dissertation, we introduce a practical optimal mass transport map based on Brenier's approach, which reduces the complexity from $O(k^2)$ to $O(k)$ and improves the efficiency and applicability. And we use our approach to address different problems in various research areas. In medical imaging, we applied our method for brain cortical surface mapping. Comparing to the traditional conformal based mapping which introduces large area distortions and may even cause numerical problens, our method minimizes the area distortions and provides the flexibility for choosing between area distortions and angle distortions. We applied our method for cortical surface classification for recognition of Alzheimer's Disease, the proposed method outperforms some other morphometry features. In computer vision, we propose to use optimal mass transportation maps for shape analysis, focusing on two important shape analysis applications including surface registration and shape space. The experimental results on 3D surface matching and comparison demonstrated the efficiency and efficacy of our approach. In visualization area, our frame-

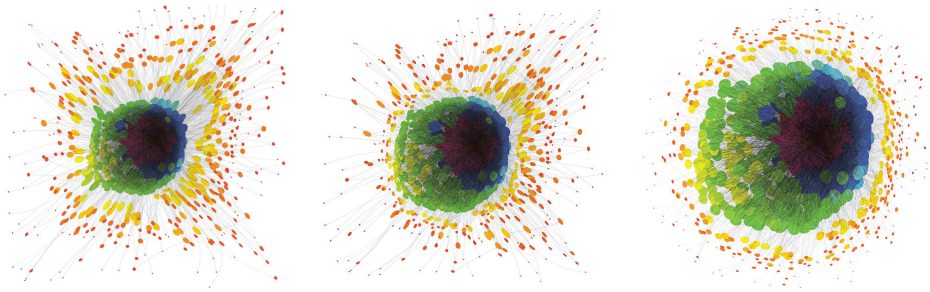

(a) (b) (c)

Figure 42: Hierarchical magnification views of a simulated radial graph. Colors are used to illustrate the node overlaps: from red (no overlap) to purple (most overlaps). (a) Original radial graph. (b) 2X and (c) 4X cascade magnification results. The 4X magnification result is generated using the 2X magnifier again on its prior magnified result. With the increasing magnification ratio, the central nodes are enlarged for a clear separation view, while compressing the exterior nodes.

work combines conformal mapping and optimal mass transport mapping, which serves as a powerful tool for a broad range of applications in visualization and graphics, especially for medical imaging.

In the future, we will explore broader applications in computer graphics, wireless sensor network and machine learning. The theoretical correctness of the high dimensional optimal mass transport has been proven, and has the potential to be applied in many research areas including computational geometry and machine learning. In future works, we will generalize and implement the optimal mass transport map to higher dimensions.

References

[1] Brain surface conformal parameterization with the slit mapping. *Biomedical Imaging: From Nano to Macro, 2008. ISBI 2008. 5th IEEE International Symposium on*, pages 448 – 451.

[2] http://www.aimatshape.net/.

[3] http://www.csie.ntu.edu.tw/ cjlin/libsvm/.

[4] http://www.freesurfer.net/.

[5] Raven, j., j. c. raven, et al. (1998). raven manual: Section 4, advanced progressive matrices. oxford, uk, oxford psychologists press ltd.

[6] CGAL, Computational Geometry Algorithms Library. http://www.cgal.org.

[7] CGAL, Computational Geometry Algorithms Library. http://www.cgal.org.

[8] AT&T graph library. *http://www.graphdrawing.org*, 2009.

[9] A. D. Alexandrov. Convex polyhedra. *Springer Monographs in Mathematics. Springer-Verlag, Berlin*, 2005.

[10] A. D. Alexandrov. *Convex Polyhedra*. Springer, 2005.

[11] S. Angenent, S. Haker, A. Tannenbaum, and R. Kikinis. Conformal geometry and brain flattening. In *Med. Image Comput. Comput.-Assist. Intervention*, pages 271–278, 1999.

[12] M. Ankerst, G. Kastenmuller, H.-P. Kriegel, and T. Seidl. 3d shape histograms for similarity search and classification in spatial databases. *Symposium on Large Spatial Databases*, pages 207–226, 1999.

[13] L. G. Apostolova, M. Beyer, A. E. Green, K. S. Hwang, J. H. Morra, Y. Y. Chou, C. Avedissian, D. Aarsland, C. C. Janvin, J. L. Cummings, and P. M. Thompson. Hippocampal, caudate, and ventricular changes in Parkinson's disease with and without dementia. *Mov. Disord.*, pages 687–695, 2010.

[14] E. Arbarello, M. Cornalba, P. Griffiths, and J. Harris. *Topics in the Theory of Algebraic Curves*. 1938.

[15] J. Ashburner, C. Hutton, R. Frackowiak, I. Johnsrude, C. Price, and K. Friston. Identifying global anatomical differences: deformation-based morphometry. *Human Brain Mapping*, 6(5-6):348–357, 1998.

[16] F. Aurenhammer. Power diagrams: properties, algorithms and applications. *SIAM J. Comput.*, 16:78–96, 1987.

[17] F. Aurenhammer. Power diagrams: properties, algorithms and applications. *SIAM Journal of Computing*, 16(1):78–96, 1987.

[18] M. Balasubramanian, J. Polimeni, and E. Schwartz. Exact geodesics and shortest paths on polyhedral surfaces. *IEEE Trans. Patt. Anal. Mach. Intell.*, 31(6):1006–1016, June 2009.

[19] M. Bauer, P. Harms, and P. Michor. Almost local metrics on shape space of hypersurfaces in n-space. *SIAM Journal on Imaging Sciences*, 5:244–310, 2012.

[20] M. Bauer, P. Harms, and P. W. Michor. Sobolev metrics on shape space of surfaces in n-space. *arXiv:1009.3616*, 2010.

[21] P. J. Besl and N. D. Mckay. A Method for Registration of 3D Shapes. *IEEE Transactions on Pattern Analysis and Machine Intelligence*, 14(2), Feb. 1992.

[22] H. Blum and R. N. Nagel. Shape description using weighted symmetric axis features. *Pattern Recognition*, 10(3):167 – 180, 1978.

[23] N. Bonneel, M. van de Panne, S. Paris, and W. Heidrich. Displacement interpolation using Lagrangian mass transport. *ACM Trans. Graph. (SIGGRAPH Asia)*, 30:158:1–158:12, 2011.

[24] N. Bonnotte. From Knothe's rearrangement to Brenier's optimal transport map. *arXiv:1205.1099 [math.OC]*, pages 1–29, 2012.

[25] D. M. Boyer, Y. Lipman, E. S. Clair, J. Puente, B. A. Patel, T. Funkhouser, J. Jernvall, , and I. Daubechies. Algorithms to automatically quantify the geometric similarity of anatomical surfaces. *PNAS*, 2011.

[26] Y. Brenier. Polar factorization and monotone rearrangement of vector-valued functions. *Comm. Pure Appl. Math.*, 44(4):375–417, 1991.

[27] Y. Brenier. Polar factorization and monotone rearrangement of vector-valued functions. *Com. Pure Appl. Math.*, 64:375–417, 1991.

[28] Y. Brenier. Polar factorization and monotone rearrangement of vector-valued functions. *Comm. Pure Appl. Math.*, 44(4):375–417, 1991.

[29] A. M. Bronstein, M. M. Bronstein, and R. Kimmel. Generalized multidimensional scaling: a framework for isometry-invariant partial surface matching. *Proc. Natl. Acad. Sci. U.S.A.*, 103(5):1168–1172, Jan 2006.

[30] M. M. Bronstein and A. M. Bronstein. Shape recognition with spectral distances. *IEEE Trans Pattern Anal Mach Intell*, 33(5):1065–1071, May 2011.

[31] K. L. Clarkson and P. W. Shor. Applications of random sampling in computational geometry, ii. *Disc. & Comp. Geom.*, 4:387–421, 1989.

[32] R. Cuingnet, E. Gerardin, J. Tessieras, G. Auzias, S. Lehericy, M. Habert, M. Chupin, H. Benali, , and O. Colliot. Automatic classification of patients with Alzheimer's disease from structural MRI: A comparison of ten methods using the ADNI database. *Neuroimage*, 56(2), 2011.

[33] M. de Berg, M. van Krefeld, M. Overmars, and O. Schwarzkopf. *Computational Geometry: Algorithms and Applications*. Springer, second edition, 2000.

[34] F. de Goes, K. Breeden, V. Ostromoukhov, and M. Desbrun. Blue noise through optimal transport. *ACM Trans. Graph. (SIGGRAPH Asia)*, 31:1–10, 2012.

[35] F. de Goes adn D.Cohen-Steiner, P. Alliez, and M. Desbrun. An optimal transport approach to robust reconstruction and simplification of 2D shapes. *Eurographics Sym. on Geometry Processing*, 30(5):1593–1602, 2011.

[36] M. Desbrun, E. Kanso, and Y. Tong. Discrete differential forms for computational modeling. In *SIGGRAPH '05: ACM SIGGRAPH 2005 Courses*, page 7, New York, NY, USA, 2005. ACM.

[37] R. S. Desikan, F. Segonne, B. Fischl, B. T. Quinn, B. C. Dickerson, D. Blacker, R. L. Buckner, A. M. Dale, R. P. Maguire, B. T. Hy-man, M. S. Albert, and R. J. Killiany. An automated labelingsystem for subdividing the human cerebral cortex on MRI scans into gyral based regions of interest. *Neuroimage*, 31:968–980, 2006.

[38] A. Dominitz and A. Tannenbaum. Texture mapping via optimal mass transport. *IEEE Transactions on Visualization and Computer Graphics*, 16(13):419–432, 2010.

[39] H. A. Drury, D. C. Van Essen, C. H. Anderson, C. W. Lee, T. A. Coogan, and J. W. Lewis. Computerized mappings of the cerebral cortex: A multiresolution flattening method and a surface-based coordinate system. *J. Cognitive Neurosciences*, 8:1–28, 1996.

[40] P. Ekman and W. Friesen. *Facial Action Coding System: A Technique for the Measurement of Facial Movement*. Consulting Psychologists, Palo Alto, 1978.

[41] B. Fischl, M. I. Sereno, and A. M. Dale. Cortical surface-based analysis. II: Inflation, flattening, and a surface-based coordinate system. *Neuroimage*, 9(2):195–207, Feb 1999.

[42] B. Fischl, M. I. Sereno, and A. M. Dale. Cortical surface-based analysis II: Inflation, flattening, and a surface-based coordinate system. *NeuroImage*, 9(2):195 – 207, 1999.

[43] N. C. Fox, R. I. Scahill, W. R. Crum, and M. N. Rossor. Correlation between rates of brain atrophy and cognitive decline in AD. *Neurology*, 52:1687–1689, 1999.

[44] T. Frankel. *The Geometry of Physics – An Introduction*. Cambridge, second edition, 2003.

[45] G. B. Frisoni, N. C. Fox, C. R. J. Jr, P. Scheltens, and P. M. Thompson. The clinical use of structural MRI in Alzheimer's disease. *Nature Reviews Neurology*, 6(2):67–77, 2010.

[46] F. Gardiner and N. Lakic. Quasiconformal teichmuller theory. *American Mathematics Society*, 2000.

[47] X. Gu, Y. He, and H. Qin. Manifold splines. *Graphical Models*, 68(3):237–254, 2006.

[48] X. Gu, F. Luo, J. Sun, and S.-T. Yau. Variational principles for Minkowski type problems, discrete optimal transport, and discrete Monge-Amperé equations. *arXiv:1302.5472*, 2013.

[49] X. Gu, F. Luo, J. Sun, and S.-T. Yau. Variational principles for Minkowski type problems, discrete optimal transport, and discrete Monge-Ampere equations. *arXiv:1302.5472 [math.GT]*, pages 1–13, 2013.

[50] X. Gu, Y. Wang, T. Chan, P. Thompson, and S.-T. Yau. Genus zero surface conformal mapping and its application to brain surface mapping. *IEEE Transactions on Medical Imaging*, 23(8):949–958, 2004.

[51] X. Gu, Y. Wang, T. F. Chan, P. M. Thompson, and S.-T. Yau. Genus zero surface conformal mapping and its application to brain surface mapping. *IEEE TMI*, 23:949–958, 2004.

[52] X. Gu, Y. Wang, T. F. Chan, P. M. Thompson, and S.-T. Yau. Genus zero surface conformal mapping and its application to brain surface mapping. *IEEE Trans. Med. Imag.*, 23(8):949–958, Aug. 2004.

[53] X. Gu and S.-T. Yau. Computing conformal structures of surfaces. *Communications in Information and Systems*, 2:121–146, 2002.

[54] X. Gu and S.-T. Yau. Global conformal parameterization. In *Symposium on Geometry Processing*, pages 127–137, 2003.

[55] X. Gu and S.-T. Yau. *Computational Conformal Geometry*. International Press, 2008.

[56] X. D. Gu and S.-T. Yau. *Computational Conformal Geometry*. Higher Education Press, first edition, 2008.

[57] S. Gupta, M. K. Markey, and A. C. Bovik. Anthropometric 3D face recognition. *IJCV*, 90(3):331–349, Dec. 2010.

[58] S. Haker, S. Angenent, A. Tannenbaum, and R. Kikinis. Nondistorting flattening maps and the 3D visualization of colon CT images. *IEEE Trans. Med. Imag.*, 19(7):665–670, 2000.

[59] S. Haker, L. Zhu, A. Tannenbaum, and S. Angenent. Optimal mass transport for registration and warping. *IJCV*, 60(3):225–240, 2004.

[60] S. Haker, L. Zhu, A. Tannenbaum, and S. Angenent. Optimal mass transport for registration and warping. *International Journal on Computer Vision*, 60(3):225–240, 2004.

[61] S. Haker, L. Zhu, A. Tannenbaum, and S. Angenent. Optimal mass transport for registration and warping. *International Journal on Computer Vision*, 60:225–240, 2004.

[62] S. Halier, S. Angenent, A. Tannenbaum, and R. Kikinis. Nondistorting flattening maps and the 3D visualization of colon CT images. *IEEE Transactions on Medical Imaging*, 19(7):665–670, 2000.

[63] R. S. Hamilton. The Ricci flow on surfaces. *Mathematics and general relativity*, 71:237–262, 1988.

[64] R. M. Haralick, S. R. Sternberg, and X. Zhuang. Image analysis using mathematical morphology. *TPAMI*, 9(4):532–550, Apr 1987.

[65] A. Hatcher. *Algebraic Topology*. Cambridge University Press, 2001.

[66] Y. He, K. Wang, H. Wang, X. Gu, and H. Qin. Manifold t-spline. In *In Proceedings of Geometric Modeling and Processing*, pages 409–422, 2006.

[67] D. Holland, J. B. Brewer, D. J. Hagler, C. Fennema-Notestine, and A. M. Dale. Subregional neuroanatomical change as a biomarker for Alzheimer's disease. *Proc. Natl. Acad. Sci*, 106(49):20954–20959, Dec 2009.

[68] W. Hong, F. Qiu, and A. Kaufman. A pipeline for computer aided polyp detection. *IEEE Transactions on Visualization and Computer Graphics*, 12(5):861–868, 2006.

[69] M. Hurdal and K. Stephenson. Discrete conformal methods for cortical brain flattening. *Neuroimage*, pages 86–98, 2009.

[70] M. K. Hurdal and K. Stephenson. Cortical cartography using the discrete conformal approach of circle packings. *NeuroImage*, 23:S119–S128, 2004.

[71] K. Im, J. Lee, U. Yoon, Y. Shin, S. Hong, I. Kim, J. Kwon, and S. Kim. Fractal dimension in human cortical surface: multiple regression analysis with cortical thickness, sulcal depth, and folding area. *Human Brain Mapping*, 27:994–1003, 2006.

[72] C. J. Jack, M. Bernstein, N. Fox, P. Thompson, G. Alexander, D. Harvey, B. Borowski, P. Britson, J. Whitwell, C. Ward, and e. al. The alzheimer's disease neuroimaging initiative (adni): Mri methods. *J. of Mag. Res. Ima.*, 27:685–691, 2007.

[73] I. H. Jermyn, S. Kurtek, E. Klassen, and A. Srivastava. Elastic shape matching of parameterized surfaces using square root normal fields. *ECCV*, 7576:804–817, 2012.

[74] M. Jin, Y. Wang, S.-T. Yau, and X. Gu. Optimal global conformal surface parameterization. In *IEEE Visualization 2004*, pages 267–274, 2004.

[75] L. Ju, M. K. Hurdal, J. Stern, K. Rehm, K. Schaper, and D. Rottenberg. Quantitative evaluation of three surface flattening methods. *NeuroImage*, 28(4):869–880, 2005.

[76] J. ju Yang, U. Yoon, H. Yun, K. Im, Y. Y. Choi, S. I. Kim, K. H. Lee, and J.-M. Lee. Prediction of human intelligence using morphometric characteristics of cerebral cortex. *WCECS*, 1, 2011.

[77] I. A. Kakadiaris, G. Passalis, G. Toderici, M. N. Murtuza, Y. Lu, N. Karampatziakis, and T. Theoharis. Three-dimensional face recognition in the presence of facial expressions: an annotated deformable model approach. *TPAMI*, 29(4):640–649, Apr 2007.

[78] L. Kantorovich. On a problem of Monge. *Uspekhi Mat. Nauk.*, 3:225–226, 1948.

[79] D. G. Kendall. Shape manifolds, procrustean metrics, and complex projective spaces. *Bulletin of the London Mathematical Society*, 16(2):81–121, 1984.

[80] Kitware, Inc. *The Visualization Toolkit User's Guide*, January 2003.

[81] C. Koch and S. Ullman. Shifts in selective visual attention: towards the underlying neural circuitry. *Human Neurobiology*, (4):219–227, 1985.

[82] P. Koehl and J. Hass. Automatic alignment of genus-zero surfaces. *TPAMI*, 36(3):466–478, Mar 2014.

[83] I. Kra and H. M. Farkas. *Riemann Surfaces*. Springer-Verlag New York, Incorporated, 1995.

[84] E. Kreyszig. *Differential Geometry*. Dover, New York, 1991.

[85] Y. kun Lai, M. Jin, X. Xie, Y. He, S. min Hu, and X. Gu. Metric-driven rosy field design and remeshing. *IEEE Transactions on Visualization and Computer Graphics*, 16(1):95–108, 2010.

[86] S. Kurtek, E. Klassen, J. C. Gore, Z. Ding, and A. Srivastava. Elastic geodesic paths in shape space of parameterized surfaces. *TPAMI*, 34:1717–1730, 2012.

[87] S. Kurtek, A. Srivastava, E. Klassen, and H. Laga. Landmark-guided elastic shape analysis of spherically-parameterized surfaces. *CG Forum*, 32, 2013.

[88] H. Laga, H. Takahashi, and M. Nakajima. Three-dimensional point cloud recognition via distributions of geometric distances. *Shape Modeling and Applications*, pages 15–23, 2006.

[89] Y. Lipman and T. Funkhouser. Mobius voting for surface correspondence. *TOG*, 28(3), Aug 2009.

[90] H. Lombaert, L. Grady, J. R. Polimeni, and F. Cheriet. FOCUSR: Feature Oriented Correspondence using Spectral Regularization - A Method for Accurate Surface Matching. *IEEE TPAMI*, Dec 2012.

[91] E. Luders, K. Narr, R. Bilder, P. Szeszko, M. Gurbani, L. Hamilton, A. Toga, and C. Gaser. Mapping the relationship between cortical convolution and intelligence: effects of gender. *Cereb Cortex*, 18:2019–2026, 2008.

[92] E. Luders, K. Narr, R. Bilder, P. Thompson, P. Szeszko, L. Hamilton, and A. Toga. Positive correlations between corpus callosum thickness and intelligence. *Neuroimage*, 37:1457–1464, 2007.

[93] B. Lvy, S. Petitjean, N. Ray, and J. Maillo. Least squares conformal maps for automatic texture atlas generation. In ACM, editor, *SIGGRAPH*, Jul 2002.

[94] S. K. Madsen, A. J. Ho, X. Hua, P. S. Saharan, A. W. Toga, C. R. Jack, M. W. Weiner, and P. M. Thompson. 3D maps localize caudate nucleus atrophy in 400 Alzheimer's disease, mild cognitive impairment, and healthy elderly subjects. *Neurobiol. Aging*, 31:1312–1325, 2010.

[95] M. Mahmoudi and G. Sapiro. Three-dimensional point cloud recognition via distributions of geometric distances. *Journal of Graphical Models*, 71:22–32, 2009.

[96] W. Massey. *Algebraic Topology: An Introduction*. Springer-Verlag, 1967.

[97] Q. Merigot. A multiscale approach to optimal transport. *Comput. Graph. Forum*, 30(5):1583–1592.

[98] G. Monge. Mémoire sur la théorie des déblais et de remblais. *Histoire de l'Académie Royale des Sciences de Paris, avec les Mémoires de Mathématique et de Physique pour la meme année,*, pages 666–704, 1781.

[99] J. Munkres. *Elements of Algebraic Topology*. Addison-Wesley Co., 1984.

[100] J. Munkres. *Topology*. Prentice Hall; 2 edition, 2000.

[101] R. Osada, T. Funkhouser, B. Chazelle, and D. Dobkin. Shape distributions. *Symposium on Large Spatial Databases*, 21:807–832, 2002.

[102] D. Pantazis, A. Joshi, J. Jiang, D. W. Shattuck, L. E. Bernstein, H. Damasio, and R. M. Leahy. Comparison of landmark-based and automatic methods for cortical surface registration. *Neuroimage*, 49(3):2479–2493, Feb 2010.

[103] F. P. Preparata and S. J. Hong. Convex hulls of finite sets of points in two and three dimensions. *Commun. ACM*, 20:87–93, 1977.

[104] S. Rachev and L. Ruschendorf. *Mass Transportation Problems*, volume I-II. Springer, New York, 1998.

[105] T. Rehman, E. Haber, G. Pryor, and A. Tannenbaum. Fast optimal mass transport for 2D image registration and morphing. *Elsevier Journal of Image and Vision Computing*, 2008.

[106] Y. Rubner, C. Tomasi, and L. J. Guibas. The earth mover's distance as a metric for image retrieval. *International Journal of Computer Vision*, 40:99–121, 2000.

[107] R. Sarkar, F. Luo, X. Yin, X. D. Gu, and J. Gao. Greedy routing with guaranteed delivery using ricci flows. In *In Proc. of the 8th International Symposium on Information Processing in Sensor Networks (IPSN09*, 2009.

[108] R. Schneider. *Convex Bodies: the Brunn-Minkowski Theory*, volume Encyclopedia of Mathematics and its Applications. Cambridge University Press, 1993.

[109] R. Schoen and S.-T. Yau. *Lectures on Harmonic Maps*. International Press, 1997.

[110] E. L. Schwartz, A. Shaw, and E. Wolfson. A numerical solution to the generalized mapmaker's problem: Flattening nonconvex polyhedral surfaces. *IEEE Trans. Patt. Anal. Mach. Intell.*, 11(9):1005–1008, Sep. 1989.

[111] E. Sharon and D. Mumford. 2D-shape analysis using conformal mapping. In *Proc. IEEE Conf. Computer Vision and Pattern Recognition*, pages 350–357, 2004.

[112] J. Shi, P. M. Thompson, B. Gutman, and Y. Wang. Surface fluid registration of conformal representation: application to detect disease burden and genetic influence on hippocampus. *Neuroimage*, 78:111–134, Sep 2013.

[113] Y. Shi, R. Lai, and A. Toga. Corporate: cortical reconstruction by pruning outliers with Reeb analysis and topology-preserving evolution. *Information Process Medical Imaging*, 22:233–244, 2011.

[114] S. M. Smith, M. Jenkinson, M. W. Woolrich, C. F. Beckmann, T. E. Behrens, H. Johansen-Berg, P. R. Bannister, M. De Luca, I. Drobnjak, D. E. Flitney, R. K. Niazy, J. Saunders, J. Vickers, Y. Zhang, N. De Stefano, J. M. Brady, and P. M. Matthews. Advances in functional and structural MR image analysis and implementation as FSL. *Neuroimage*, 23 Suppl 1:S208–219, 2004.

[115] A. Sotiras, C. Davatzikos, and N. Paragios. Deformable medical image registration: A survey. *TMI*, 32:1153–1190, 2014.

[116] A. Srivastava and I. H. Jermyn. Looking for shapes in two-dimensional cluttered point clouds. *TPAMI*, 31(9):1616–1629, Sep 2009.

[117] A. Srivastava, S. H. Joshi, W. Mio, and X. Liu. Statistical shape analysis: clustering, learning, and testing. *TPAMI*, 27(4):590–602, Apr 2005.

[118] A. Srivastava, E. Klassen, S. H. Joshi, and I. H. Jermyn. Shape analysis of elastic curves in euclidean spaces. *TPAMI*, 33(7):1415–1428, July 2011.

[119] M. Styner, J. A. Lieberman, R. K. McClure, D. R. Weinberger, D. W. Jones, and G. Gerig. Morphometric analysis of lateral ventricles in schizophrenia and healthy controls regarding genetic and disease-specific factors. *Proc. Natl. Acad. Sci. U.S.A.*, 102(13):4872–4877, Mar 2005.

[120] Z. Su, W. Zeng, R. Shi, Y. Wang, J. Sun, and X. Gu. Area preserving brain mapping. *CVPR*, pages 2235–2242, 2013.

[121] P. Thompson and A. Toga. A surface-based technique for warping 3-dimensional images of the brain. *IEEE Trans. Med. Imag.*, 15:1–16, 1996.

[122] P. M. Thompson and A. W. Toga. A framework for computational anatomy. In *CVS*, volume 5, pages 1–12, 2002.

[123] B. Timsari and R. M. Leahy. Optimization method for creating semi-isometric flat maps of the cerebral cortex. *Medical Imaging 2000: Image Processing*, 3979(1):698–708, 2000.

[124] W. S. Torgerson. Multidimensional scaling: I. theory and method. *Psychometrika*, 17:401–419, 1952.

[125] D. Tosun and J. Prince. A geometry-driven optical flow warping for spatial normalization of cortical surfaces. *IEEE Trans. Med. Imag.*, 27(12):1739 –1753, Dec. 2008.

[126] T.Rehman, E.Haber, G.Pryor, J.Melonakos, and A.Tannenbaum. 3D nonrigid registration via optimal mass transport on the GPU. *Medical Image Analysis*, 13:931–40, 2009.

[127] N. S. Trudinger. Remarks concerning the conformal deformation of riemannian structures on compact manifolds. *Ann. Scuola Norm. Sup. Pisa*, 22(2):265–274, 1968.

[128] R. Unnikrishnan and M. Hebert. Multi-scale interest regions from unorganized point clouds. *CVPR*, 2008.

[129] C. Villani. *Topics in Optimal Transportation*. American Mathematical Society, 2003.

[130] X. Wang, X. Ying, Y.-J. Liub, S.-Q. Xin, W. Wang, X. Gu, W. Mueller-Wittig, and Y. He. Intrinsic computation of centroidal voronoi tessellation (cvt) on meshes. *ACM Symposium on Solid and Physical Modeling*, 2014.

[131] Y. Wang, X. Gu, T. F. Chan, P. M. Thompson, and S.-T. Yau. Conformal slit mapping and its applications to brain surface parameterization. In *Med. Image Comp. Comput.-Assist. Intervention, Proceedings, Part I*, pages 585–593, 2008. LNCS 5241.

[132] Y. Wang, M. Gupta, S. Zhang, S. Wang, X. Gu, D. Samaras, and P. Huang. High resolution tracking of non-rigid motion of densely sampled 3d data using harmonic maps. *IJCV*, 76, 2008.

[133] Y. Wang, J. Shi, X. Yin, X. Gu, T. F. Chan, S. T. Yau, A. W. Toga, and P. M. Thompson. Brain surface conformal parameterization with the Ricci flow. *IEEE Trans Med Imaging*, 31(2):251–264, Feb 2012.

[134] S. H. Weitraub. *Differential Forms: A Complement to Vector Calculus*. Academic Press, 2007.

[135] L. Yin, X. Chen, Y. Sun, T. Worm, and M. Reale. A high-resolution 3d dynamic facial expression database. *International Conference on Automatic Face and Gesture Recognition*, pages 17–19, 2008.

[136] L. Younes. Spaces and manifolds of shapes in computer vision: An overview. *Image Vision Comput.*, 30(6-7):389–397, June 2012.

[137] L. Younes, P. Michor, J. Shah, and D. Mumford. A metric on shape space with explicit geodesics. *Atti Accad. Naz. Lincei Cl. Sci. Fis. Mat. Natur.*, 19(1):25–57, 2008.

[138] W. Zeng, J. Marino, A. E. Kaufman, and X. D. Gu. Volumetric colon wall unfolding using harmonic differentials. *Computers and Graphics*, 35(3):726—-732, 2011.

[139] W. Zeng, D. Samaras, and X. Gu. Ricci flow for 3d shape analysis. *IEEE TPAMI.*, 32:662–677, 2010.

[140] W. Zeng, X. Yin, Y. Zeng, Y. L. X. Gu, and D. Samaras. 3D face matching and registration based on hyperbolic Ricci flow. *CVPR Workshop on 3D Face Processing*, pages 1–8, 2008.

[141] W. Zeng, X. Yin, Y. Zeng, Y. Lai, X. Gu, and D. Samaras. 3d face matching and registration based on hyperbolic ricci flow. In *CVPR 3D Face Processing Workshop*, 2008.

[142] D. Zhang and M. Hebert. Harmonic maps and their applications in surface matching. *CVPR*, pages 524–530, 1999.

[143] X. Zhao, B. Li, L. Wang, and A. Kaufman. Texture-guided volumetric deformation and visualization using 3D moving least squares. *The Visual Computer*, 28:193–204, 2012.

[144] X. Zhao, Z. Su, X. D. Gu, A. Kaufman, J. Sun, J. Gao, and F. Luo. Area-preservation mapping using optimal mass transport. *TVCG*, 19(12):2838–2847, Dec 2013.

[145] X. Zhao, W. Zeng, X. D. Gu, A. E. Kaufman, W. Xu, and K. Mueller. Conformal magnifier: A focus+context technique with local shape preservation. *IEEE Transactions on Visualization and Computer Graphics*, 18(11):1928–1941, 2012.

[146] J. Zhong and A. Qiu. Multi-manifold diffeomorphic metric mapping for aligning cortical hemispheric surfaces. *Neuroimage*, 49(1):355–365, Jan 2010.

[147] L. Zhu, S. Haker, and A. Tannenbaum. Area-preserving mappings for the visualization of medical structures. *In Medical Image Computing and Computer-Assisted Intervention*, 2879:277–284, 2003.

[148] L. Zhu, S. Haker, and A. Tannenbaum. Flattening maps for the visualization of multibranched vessels. *IEEE Trans. Med. Imag.*, 24(2):191–198, 2005.

[149] L. Zhu, Y. Yang, S. Haker, and A. Tannenbaum. An image morphing technique based on optimal mass preserving mapping. *IEEE Trans. Med. Imag.*, 16(6):1481–1495, 2007.

[150] G. Zou, J. Hu, X. Gu, and J. Hua. Area-preserving surface flattening using Lie advection. *Medical Image Computing and Computer-Assisted Intervention (MICCAI)*, 14:335–342, 2011.

[151] G. Zou, J. Hu, X. Gu, and J. Hua. Authalic parameterization of general surfaces using Lie advection. *IEEE Transactions on Visualization Computer Graphics*, 17(12):2005–2014, 2011.